Hydrodynamic Design of Highly Loaded Torque-neutral Ducted Propulsor for Autonomous Underwater Vehicles

Suraj A. Pawar

Thesis submitted to the Faculty of the

Virginia Polytechnic Institute and State University

in partial fulfillment of the requirements for the degree of

Master of Science

in

Mechanical Engineering

Stefano Brizzolara, Chair

Alexander Leonessa

Walter O'Brien

Daniel Stilwell

December 10, 2018

Blacksburg, Virginia

Keywords: CFD, Optimization, AUV, Propulsor, Turbulence Modeling

Hydrodynamic Design of Highly Loaded Torque-neutral Ducted Propulsor for Autonomous Underwater Vehicles

Suraj A. Pawar

(ABSTRACT)

The design method for marine propulsor (propeller/stator) is presented for an autonomous underwater vehicle (AUV) that operates at a very high loading condition. The design method is applied to Virginia Tech Dragon AUV. It is based on the parametric geometry definition for the propulsor, use of high-fidelity CFD RANSE solver with the transition model, construction of the surrogate model, and multi-objective genetic optimization algorithm. The CFD model is validated using the paint pattern visualization on the surface of the propeller for an open propeller at model scale. The CFD model is then applied to study hydrodynamics of ducted propellers such as forces and moments, tip leakage vortex, leading-edge flow separation, and counter-rotating vortices formed at the duct trailing edge. The effect of variation of thickness for stator blades and different approaches for modeling the postswirl stator is presented. The field trials for Dragon AUV shows that there is a good correlation between expected and achieved design speed under tow condition with the designed base propulsor. The marine propulsor design is further improved with an objective to maximize the propulsive efficiency and minimize the rolling of AUV. The stator is found to eliminate the swirl component of velocity present in the wake of the propeller to the maximum extent. The propulsor designed using this method (surrogate-based optimization) is demonstrated to have an improved torque balance characteristic with a slight improvement in efficiency than the base propulsor design.

Hydrodynamic Design of Highly Loaded Torque-neutral Ducted Propulsor for Autonomous Underwater Vehicles

Suraj A. Pawar

(GENERAL AUDIENCE ABSTRACT)

The propulsion system is the critical design element for an AUV, especially if it is towing a large payload. The propulsor for towing AUVs has to provide a very large thrust and hence the propulsor is highly loaded. The propeller has to rotate at very high speed to produce the required thrust and is likely to cavitate at this high speed. Also at this high loading condition, the maximum ideal efficiency of the propulsor is very less. Another challenge is the induced torque from the propeller on AUV that can cause the rolling of an AUV which is undesirable. This problem can be addressed by installing the stator behind the propeller that will produce torque in the opposite direction of the propeller torque. In this work, we present a design methodology for marine propulsor (propeller/stator) that can be used in AUV towing a large payload. The propulsor designed using this method has improved torque characteristics and has the efficiency close to 80 % of the ideal efficiency of ducted propeller at that loading condition.

Acknowledgments

I express my sincere gratitude to Dr. Brizzolara not only for his guidance but also for his motivation throughout my graduate studies. He always took time to explain complex concepts in the simplest terms and he ensured that I grasp theory as well as computational procedures in order to conduct substantial research. I would like to thank my committee for their advice and suggestions that helped improve the quality of my thesis. I would like to thank Dr. Neu and Dr. Stilwell for their guidance and advise on several aspects of this work like the mechanical system design and gathering field trial data.

I would like to thank all members of Autonomous Systems and Controls Lab for making my work enjoyable. It has been a great learning experience to work with you all. In particular, I would like to thank Michael Kepler for designing the controller for Dragon AUV, Jorge Jimenez for his contributions to internal hardware and software package specific to Dragon AUV, Stephen Krauss for his help with the software architecture and conducting field trials, and Jack Webster for his insights on propeller design and turbulence modeling.

I am grateful to my dear parents: Arun Pawar and Shobha Pawar for their unconditional love and support. I would not be in this position without the sacrifice that they made. Finally, I would like to thank my brother, Rajan for his constant encouragement throughout my graduate studies. I owe every bit of my achievement to them.

Contents

List of Figures

List of Tables

Chapter 1

Introduction

The Virginia Tech Dragon AUV is a small AUV designed for a mission to foul another ship's propeller using a long thick rope[1]. Fig. 1.1 shows the CAD drawing of Dragon AUV with internal components. Technical specifications of Dragon AUV are given in Table 1.1. The control surfaces for Dragon are placed on the nose to get better maneuverability than if placed at the tail. One of the challenges in this mission is that the drag of the payload is multiple times the drag of bare hull. Hence, the marine propulsor for Dragon AUV should be designed in such a way that it can produce very high thrust. The propulsor for Dragon AUV is designed with an objective to maximize propulsive efficiency and minimize rolling of the vehicle. In this thesis, we describe the numerical simulation based design method for marine propulsor which are highly loaded.

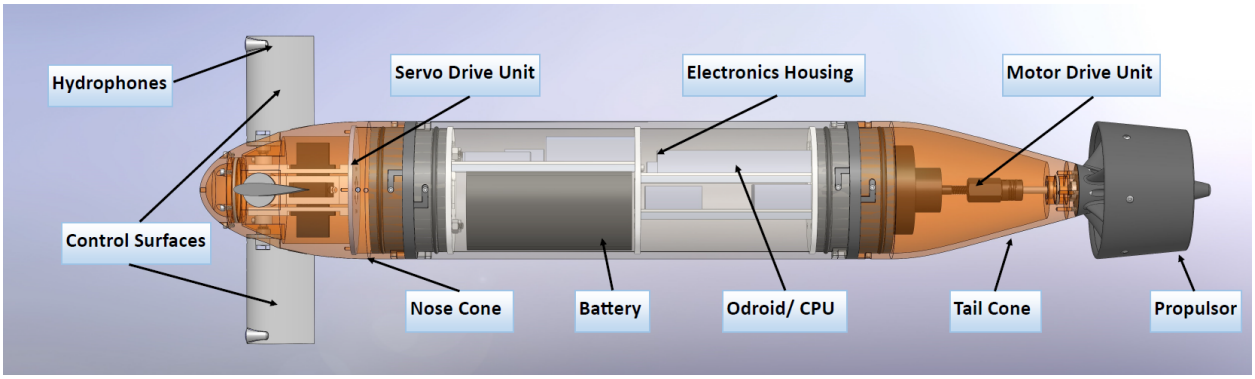

Figure 1.1: CAD rendering of Virginia Tech Dragon AUV with internal components

[1]The rope is referred to as the payload further in this thesis

Parameter	Symbol	Value	Units
Length	L	32.75	inch
Diameter	D	4.875	inch
Weight	M	7.94	kg
Design Speed	V	2	m/s
Payload Drag	F_D	70	N
Energy Storage	-	266.4	W

Table 1.1: Virginia Tech Dragon AUV Specifications

1.1 Motivation

The design of the propeller for small AUV is a challenging task because the flow on the surface of the propeller is in the transitional flow regime with length-based Reynolds number $Re_L \approx 5 \cdot 10^5$, often lower than the minimum Reynolds number accepted by ITTC. The complexity increases when the propeller is highly loaded i.e, when the specific thrust is order of magnitudes higher than the value reached by typical AUV. At low Reynolds number, the stall occurs even for a small angle of attacks. The effect of viscosity is important at low Reynolds number and can not be neglected. Traditional methods such as lifting line method and panel methods assume that the flow is inviscid and does not account for unsteady viscous flow. Fully viscous methods, such as Reynolds Averaged Navier-Stokes Solver simulation can capture unsteady flow separation and tip vortex. However, current industrial grade turbulence model are based on fully turbulent flow assumption, hence inherently not applicable to low Reynolds number flow propellers. New transitional turbulence models have been developed recently, but they are not fully validated for propellers, especially ducted propulsors.

Another constraint in the propulsor design presented here is its maximum diameter. Also, the advance velocity V_a is relatively low (close to 2 m/s in our case) and the thrust is very high due to large payload drag. All these factors act adversely and the thrust loading coefficient $C_T = T/(\frac{1}{2}\rho V_a^2 \frac{\pi}{4} D^2)$ can be very large. The ideal maximum efficiency of the

propulsor in terms of thrust loading coefficient C_T is given as

$$\eta = \frac{2}{1 + \sqrt{1 + C_T}} \tag{1.1}$$

For Virginia Tech Dragon AUV, the propulsor diameter is required to be less than 4.875 *inch* and the thrust loading coefficient for this diameter is approximately 9. The maximum open-water efficiency of the propulsor can be 47 % at such high loading condition. Hence, the propulsor should be carefully designed in such a way that axial and rotational energy losses are minimized and we can achieve higher efficiency.

Finally, the torque of the propeller goes in pair with the thrust, so a highly loaded propeller will transmit the high torque back to the vehicle. If this torque is not neutralized, then the AUV will have large roll angle owing to induced torque from the propeller. This type of equilibrium cannot be tolerated for the type of mission this vehicle is designed for and hence the torque has to be counteracted. This can be addressed by several methods: such as dedicated stabilizing fins, asymmetric deflection of control surfaces, contra-rotating propeller arrangement [56] or the adoption of preswirl/ postswirl stator [30, 31]. Each of these strategies has certain advantages or disadvantages over the other and hence should be carefully investigated. The overall mechanical system design for the propulsor should be simple and should be designed in such a that it can be used for different payloads without major changes in mechanical design.

1.2 Approach

The advancement in numerical simulation software makes optimization of unconventional propellers increasingly popular. Several researchers have recently worked on simulation-

based design and optimization of marine propellers with an objective to improve propulsive efficiency and to reduce the side effects such as cavitation and noise [8, 14, 24, 61]. In this study, parametric geometry definition of propulsor, use of high-fidelity CFD RANSE solver, and surrogate-based optimization algorithms are used in developing a design framework for highly loaded marine propulsor.

1.2.1 Applied Computational Fluid Dynamics

The research in computational fluid dynamics is mainly focused on CFD algorithms and high-performance computing. The considerable amount of research in CFD in the last few decades has made it possible to use CFD as a tool for analyzing challenging engineering problems such as viscous, turbulent flows around different geometries in unsteady conditions. These problems can also be studied using experimental techniques on scaled down models tested in towing tanks and wind tunnel. However, experiments are costly, time-consuming and are affected by scale effects that sometimes might not provide a better understanding of these problems. With the advancement in computational resources, the CFD model can analyze the problem and give an accurate solution in a couple of hours based on the size of the problem. Just like any other complex tool, special attention should be given to verification and validation of CFD model to confirm its accuracy.

1.2.2 Design by Optimization

The design by optimization is an indirect approach based on formal mathematical algorithms to derive a trial and error like design process. This indirect approach allows the use of any flow solver to analyze different propulsor geometries and select an optimum geometry from this population that satisfies certain objective functions and constraints. The modification in

the initial population of designs can be achieved using different optimization algorithms. In this study, a genetic optimization algorithm which relies on bio-inspired operators mutation, crossover and selection is used. The genetic optimization guarantees a global convergence, but it might need an evaluation of hundreds or even thousands of different geometries before an optimum solution satisfying the objective and constraint is found. It is not practical to use CFD simulation for every case to evaluate propulsor's performance. Hence, the surrogate model is created from an initial population generated using design space exploration algorithm and this surrogate model is used for the genetic optimization algorithm. This framework is computationally efficient and allows the use of CFD RANSE solver with minimum user intervention.

1.3 Thesis Outline

The thesis is organized as below

- In Chapter 2, the conceptual design of the propulsor including propeller-hull interaction is discussed. Additionally, the calculation of drag of an AUV and the payload and different options available for the propulsor configuration are presented.

- In Chapter 3, the main theoretical aspects of two turbulent models are given. In addition, different techniques for modeling the propulsor using CFD solver are included in this chapter.

- In Chapter 4, the validation of CFD model with transition model is presented for open and ducted propeller. Also, propeller redesign using different hydrofoil section and the parametric geometry module for the propeller is discussed.

- In Chapter 5, the design technique for the postswirl stator is presented. Different design aspects affecting the performance of postswirl stator is given in this chapter.
- In Chapter 6, the optimization framework which includes design space exploration algorithm, surrogate model construction and Genetic optimization algorithm is presented. The performance of some candidate propulsor designs is also given.
- In Chapter 7, we give closing remark and summarize this work.

Chapter 2

Conceptual Design of the Propulsor

Before starting the design of the propulsor, it is necessary to determine the total power required to propel an AUV and the payload at design speed. The main components of required power are the drag of an AUV and the payload, the propeller-hull interaction, and the propeller open-water efficiency. These three components are discussed in this chapter. Additionally, the information of required power is needed for selection of other components such as battery and DC motor driving the propeller.

2.1 Drag Analysis

The propeller is designed to produce thrust which can overcome the drag of an AUV and the payload. The major drag comes from the payload. There are different methods for calculating the drag force which includes towing tank experiments, empirical formulas and CFD simulations with RANSE solver. For the conceptual design stage, simple empirical formulas which give a good prediction of drag forces are used.

2.1.1 AUV Drag

The force acting on submerged bodies is due to the viscosity of water. For deeply submerged bodies, there is no wave formation at the surface and hence there is no wave-making re-

sistance. The drag force can be divided into two components - skin friction resistance and pressure (form) resistance. The skin friction resistance is due to wall shear stress caused by the velocity decrease in the boundary layer formed around the body. The adjustment of the streamline due to the boundary layer formed also alters the pressure distribution on the front and aft portion and hence there is a net force acting on the body in a direction opposite to its motion. This component is called as viscous pressure drag. The total drag of an AUV can be calculated using two separate factors. *ITTC 1957 Line* [39] is used for calculation of skin friction drag coefficient as below

$$C_F = \frac{0.075}{(log_{10}Rn - 2)^2} \tag{2.1}$$

The skin friction drag coefficient C_F calculated using the equation 2.1 has to be multiplied with the form factor $(1 + K)$. The form factor takes into account the shape of the vehicle and it gives the complete drag coefficient of the vehicle. Hoerner [28] proposed an expression for the form factor for axisymmetric bodies of elongated length as a function of diameter and length

$$(1 + K) = 1 + 1.5\left(\frac{d}{l}\right)^{1.5} + 7\left(\frac{d}{l}\right)^{3} \tag{2.2}$$

The total drag force acting on AUV is calculated as below

$$C_D = (1 + K)C_F; \quad F_D = \frac{1}{2}C_D\rho AV^2 \tag{2.3}$$

where F_D is the AUV drag, A is the wetted surface area and V is the speed of an AUV. The above formulation for drag does not take appendages into account. Typical appendages found on AUV are maneuvering fins and stabilizers and more information on calculation of appendages drag can be found in Molland et al. [47]. For simplicity, considering this AUV has only fins as appendages, total appendages drag is considered to be 10% of bare hull drag

calculated using equation 2.3.

2.1.2 Payload Drag

The mission requirement is to tow a long rope into the propeller of another ship to foul it. The payload in this study is 1 inch thick and 50 m long rope. The drag of the rope is calculated by approximating it as a circular cylinder with rough surface. Reid and Wilson [53] developed an expression for tangential drag coefficient as a function of surface roughness. The drag coefficient calculated using this formula shows good agreement with the experimental results for towing tests of standard cables. The drag coefficient is calculated as below

$$C_{D,Rope} = 2\Big[\frac{k}{ln(120\frac{a}{s})}\Big] \tag{2.4}$$

where $k = 0.4$ is Von Karman constant, a is the radius of the rope and $s = 3\ mm$ is the equivalent roughness height. The drag coefficient $c_{D,Rope}$ is calculated to be 0.0082. Total payload drag is calculated based on the wetted surface area of the rope as below

$$F_{D,Rope} = \frac{1}{2}C_{D,Rope}\rho(\pi dl)V^2 \tag{2.5}$$

where d is the rope diameter, l is the rope length and V is the design speed. The rope drag is calculated to be 70 N for the design speed of 4 knots.

2.2 Propeller-hull Interaction

When the propeller is operating behind the hull the velocity experienced by the propeller is not the same as the speed of an AUV. The axial velocity distribution in the wake of the

body is a result of potential and viscous wake resulting in a velocity smaller in magnitude than the speed of an AUV. This velocity is referred to as the advance velocity V_a. The wake fraction is defined as the ratio of difference in AUV velocity and advance velocity to AUV velocity. It is given as below

$$w = \frac{V - V_a}{V} \tag{2.6}$$

where V is the velocity of an AUV and V_a is the advance velocity.

The wake fraction can be calculated by measuring the average velocity at some distance upstream from the propeller plane without the propeller. The wake fraction calculated in this way is called nominal wake fraction. The wake fraction changes when the propeller is developing a thrust and can be calculated by comparing propeller's performance behind the hull with the open-water performance of the propeller (thrust identity principle). This wake fraction is called effective wake fraction.

When the propeller is developing a thrust, it accelerates the water ahead of it. The increase in velocity of the flow increases the frictional resistance. Also, the pressure near the tail section of an AUV decreases and hence pressure resistance increases. If there is a separation at the tail section of an AUV, then the action of the propeller might suppress the separation by reducing unfavorable pressure gradient. All these effects result into the change in hull resistance (usually increase) than the resistance of bare hull without the propeller. The increase in drag of hull is taken into account using thrust deduction factor t. The increase in drag is proportional to the propeller's thrust. The thrust deduction factor is defined as below

$$t = \frac{T - R}{T} \tag{2.7}$$

where T is the total thrust (propeller and duct) and R is the bare hull resistance without the propeller.

For calculation of thrust deduction factor and wake fraction, the information about the propeller is needed. In the conceptual design stage the propeller's geometry is not finalized and hence empirical relations or experimental study for similar sized AUV should be used to determine the thrust deduction factor and wake fraction.

The wake fraction and thrust deduction factor are calculated from the data given in Jackson [32] for the conceptual design stage. These curves were obtained by accumulating data and are good approximation for conceptual design stage. The wake fraction w is found to be 0.18 and thrust deduction factor t is found to be 0.04 for $L = 32.75\ in$, $D = 4.875\ in$, $K_2 = 1.35$ and $D_p/D_h = 0.6$. This data does not take into account the drag of the payload (towing condition) into account and hence actual parameters are likely to be different from these values. The final wake fraction and thrust deduction factor are calculated using thrust identity principle and is discussed in section 5.2.

2.3 Selection of Propeller

Open-water diagrams of the propeller can be used for selecting the base propeller geometry for further design and optimization if the AUV resistance, wake fraction and thrust deduction factor are known. The basic design parameters such as the number of blades, expanded area ratio, and average pitch can be selected using open-water diagrams. The open-water performance of families of propeller were obtained experimentally by systematically changing the geometrical parameters and is expressed as a polynomial function of the pitch of the propeller and advance ratio [16]. In case of ducted propeller, the open-water performance of propeller is expressed in terms of non-dimensional hydrodynamic coefficients as below

$$K_{TP} = \frac{T_P}{\rho n^2 D^4}; \quad K_{TN} = \frac{T_N}{\rho n^2 D^4}; \quad K_Q = \frac{Q}{\rho n^2 D^4}; \quad K_T = K_{TP} + K_{TN}; \quad \eta = \frac{J}{2\pi}\frac{K_T}{K_Q} \tag{2.8}$$

where T_P, T_N, Q, J is the propeller thrust, duct thrust, propeller torque and advance coefficient respectively.

For attaining the high efficiency of the propeller, the diameter of the propeller should be large. However, the diameter is usually restricted by the hull design. For the specific maximum diameter of the propeller, optimum revolution speed and optimum pitch ratio can be determined by matching the total resistance of an AUV and the payload with the thrust coefficient of the propeller. First, the total resistance is transformed into a specific thrust coefficient C as given below

$$J = \frac{V_a}{nD}; \quad \left(\frac{K_T}{J^2}\right) = \frac{T}{\rho n^2 D^4} \cdot \frac{n^2 D^2}{V_a^2} = \frac{T}{\rho V_a^2 D^2} = C \tag{2.9}$$

The thrust coefficient $K_{T,AUV}$ can be obtained from known C at different advance coefficients J as below

$$K_{T,AUV} = CJ^2 \tag{2.10}$$

By matching the AUV resistance curve with thrust coefficient curve of the propeller, corresponding advance ratio, pitch of the propeller and efficiency can be calculated. The optimum speed of the propeller can be calculated using advance ratio as given in equation 2.9. Also, the torque of the propeller can be calculated using torque coefficient at same advance ratio.

For the propeller selection, three types of propellers are considered. They are Wageningen B- Series open propeller, K_a-4-70 propeller inside the accelerating nozzle no. 19A and inside the decelerating nozzle no. 37. The open-water performance for these propellers is available in the form of polynomial regression [16]. Four diameters and four pitch values of each type of propeller are used for the propeller selection. The operating point, efficiency, speed, and torque at the operating condition can be found by matching of the total resistance curve and the propeller thrust coefficient curve. Fig. 2.1 shows the resistance curve matching for

three types of propellers considered in this study.

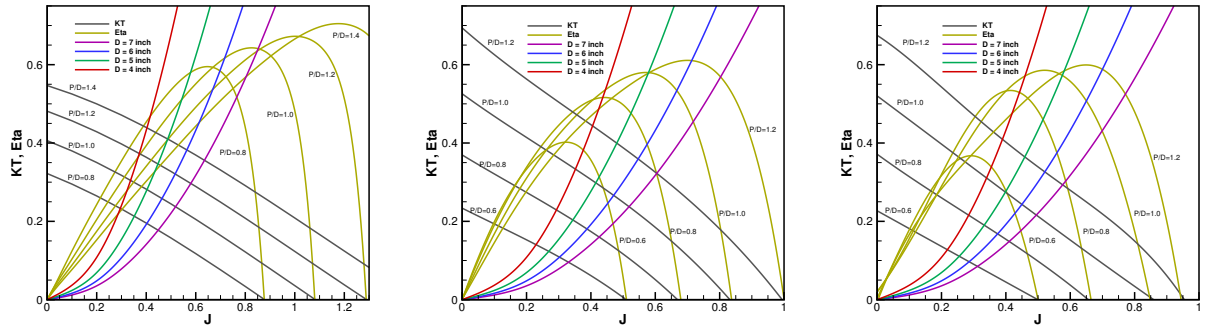

(a) B-Series (b) K_a-4-70 inside Duct 19A (c) K_a-4-70 inside Duct 37

Figure 2.1: Preliminary Selection of propeller using thrust matching at self-propulsion point at $V = 2\ m/s$

Fig. 2.2 gives the efficiency and the torque for different propellers (different diameters and pitch ratios). The selected propeller should have high efficiency for increasing the mission endurance and low torque for the directional stability. Since the propeller is directly coupled the brushless DC motor, the revolution speed of the propeller should be such that the efficiency of the motor at required torque and speed is high at that point. In general as the diameter of the propeller increases, the efficiency also increases. However, there is a significant increase in the propeller torque also. So, the conceptual design must find a compromise between optimum efficiency and minimum torque. For propeller K_a-4-70, the efficiency increases with an increase in the pitch ratio. The efficiency of the propeller K_a-4-70 increases significantly when the pitch ratio is increased from 0.6 to 0.8 with a slight increase in torque. The increase in efficiency is not significant when the pitch ratio is increased beyond 0.8. The efficiency of the motor is calculated to be to be in the range 85% to 89% in the speed range $n = 55$ to 62 rps (calculation for the motor is shown in Appendix A). The operating point for propeller K_a-4-70 with $P/D = 0.8$ lies in that range. Hence the propeller K_a-4-70 with the $P/D = 0.8$ adn $D = 4\ inch$ inside nozzle no. 19A is selected as

the base propeller for further design optimization.

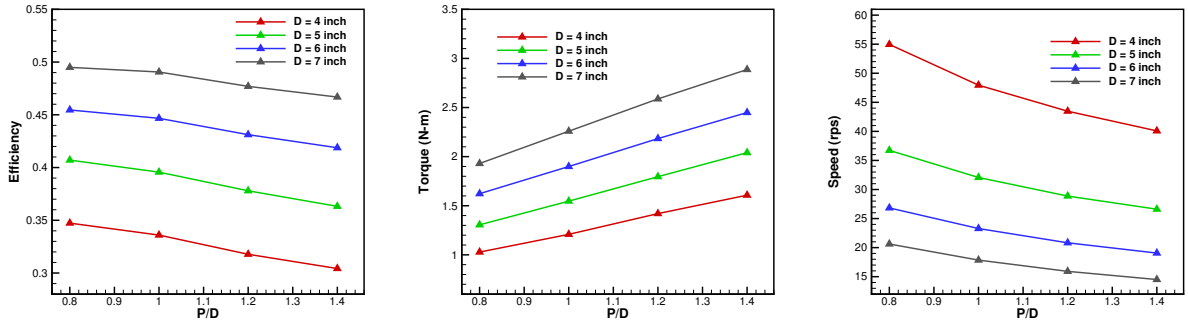

(a) B-Series propeller

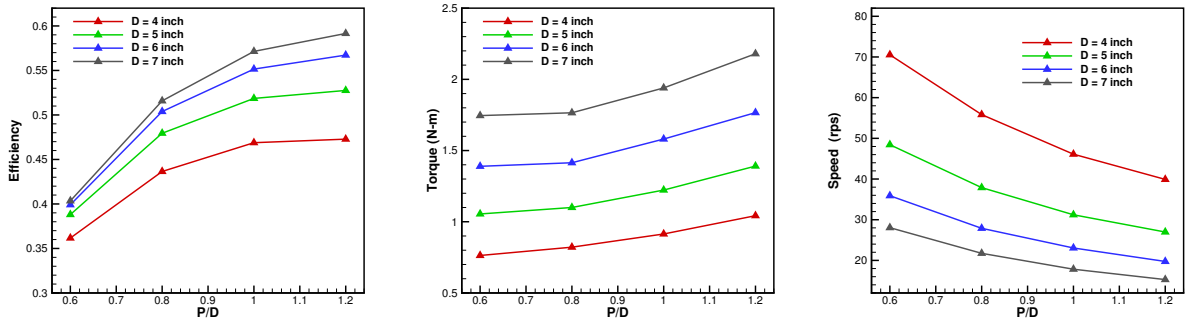

(b) Propeller K_a-4-70 inside Duct 19A

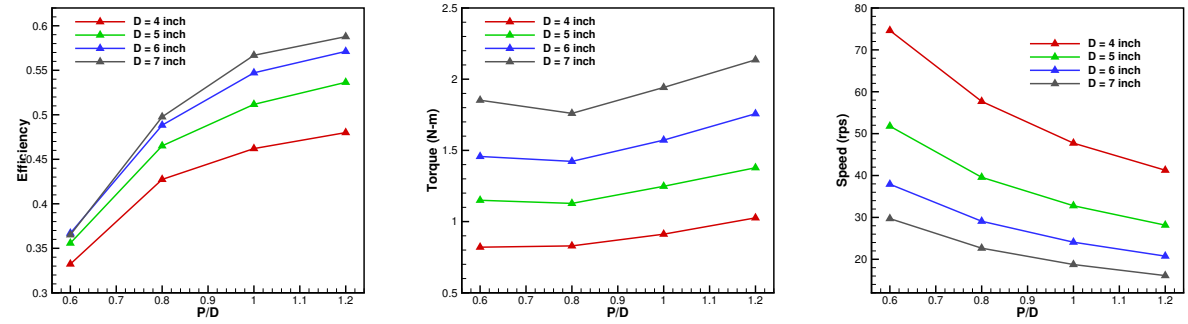

(c) Propeller K_a-4-70 inside Duct 37

Figure 2.2: Parametric study for different diameters and pitch ratios of the propeller for $V = 2\ m/s$ Left: Efficiency, Middle: Torque (N-m), Right: Speed (rps)

2.4 Anti-Roll Devices

The torque calculated in section 2.3 is considerably higher than the torque experienced by AUVs designed for non-towing conditions. Hence, it is important to counteract the propeller torque to avoid rolling instability to the AUV. Otherwise, the propeller torque will induce excessive rolling on the AUV. The propeller-stator combination is one of the cost-effective and practical ways for counteracting the propeller torque.

There are number of studies on the design of propeller-stator devices. In all these studies the main objective was to increase the efficiency of the propulsion devices by minimizing the energy losses that are associated with the propeller. These losses are mainly due to a transfer of energy in the slipstream of the propeller, that is rotational energy loss due to a transfer of torque from propeller to the water and axial energy loss due to an acceleration of water to produce thrust. Use of contra-rotating propeller can reduce the rotational energy loss and improve the efficiency up to 10-14 % [46]. However, contra-rotating propellers are mechanically complex and are expensive. Instead, the propeller-stator combination might reach efficiency gain up to 5-6% but are simple and cheap.

The stator can be placed either upstream of the propeller or behind the propeller. If the stator is placed upstream then it is called as the pre-swirl stator. The pre-swirl stator is usually used as an energy saving device and it can increase the efficiency up to 5 % [67]. The pre-swirl stator generates a swirling flow in a direction opposite to the rotation of the propeller. This increases a loading on the propeller and thrust of the propeller increases. This increase in thrust should be more than the drag of the pre-swirl stator to obtain a gain in efficiency. From energy balance, the kinetic rotational energy behind the propeller gets reduced and the flow leaving the propeller has less rotation in the final slipstream.

If the stator is placed behind the propeller then it is called as the postswirl stator. Typically,

the postswirl stator is used inside a decelerating duct in the so called pumpjet propulsor and are widely used on large submarine vessels. The main objective of pumpjet propulsor is to reduce the hydrodynamic noise of the propeller and to counteract the torque of the propeller to reduce roll. Suryanarayana et al. [58] carried out the experimental evaluation of the performance of propulsor in wind tunnel and showed that the post-swirl stator can counteract up to 90 % of the propeller torque at all advance ratios. Guner and Glover [26] showed that for the highly loaded propeller, the postswirl stator can produce a net positive thrust and thus will have improved efficiency than the equivalent propeller. Hence, in this study postswirl stator is used for counteracting the propeller torque.

Chapter 3

Computational Fluid Dynamics Methodology

The work done for this thesis is based on the application and analysis of CFD simulations. All CFD simulations are performed using Reynolds-Averaged Navier-Stokes Equation (RANSE) solver in a commercial solver StarCCM+ [3]. This solver allows meshing, CFD model formulation and post-processing the results in one package. The focus of this research is on the application of CFD and not the development of CFD itself. Hence, the detail explanation of mathematical formulation in CFD is omitted. In this chapter, main theoretical aspects of governing equations, turbulence model formulation, numerical algorithm, and propeller modeling techniques are discussed.

3.1 Governing Equations and Discretization

The fundamental laws that govern the fluid mechanics are conservation of mass, linear momentum and energy. The balance of mass through a control volume is expressed by the continuity equation. For incompressible flow, the continuity equation is given as

$$\boldsymbol{\nabla} \cdot (V) = 0 \tag{3.1}$$

where V is the continuum velocity.

The time rate of change of linear momentum is the total force acting on the fluid. The momentum equation for incompressible flow is given as

$$\frac{\partial(V)}{\partial t} + \boldsymbol{\nabla} \cdot (V \otimes V) = -\frac{1}{\rho}\boldsymbol{\nabla} \cdot (p\mathbf{I}) + \frac{1}{\rho}\boldsymbol{\nabla} \cdot \mathbf{T} + f_b \tag{3.2}$$

where p is the pressure, $\mathbf{T}$ is the viscous stress tensor and f_b is the resultant body forces (such as gravitational and centrifugal forces).

CFD uses discretization methods to convert the continuous system of equations to a set of discrete algebraic equations. The set of algebraic equations are solved using numerical techniques. The domain is divided into . The unknowns are stored at specific locations of the mesh like at centroids, faces or edges. For fluid mechanics problems, StarCCM+ uses a Finite Volume method for discretization. In this method, conservation laws are satisfied on each cell and hence global conservation is ensured. In this work, the value of unknowns at cell face is approximated using second-order central difference scheme. For unsteady simulations, the implicit time integration method is used with the second-order central difference scheme for temporal discretization.

3.2 Reynolds-Averaged Navier-Stokes Formulation

Fluid flows of practical applications are characterized by irregularly fluctuating flow quantities. These fluctuations are at small scale and high frequencies that resolving them in time and space are computationally expensive. Instead of solving for the exact governing equation for turbulent flows using Direct Numerical Simulation (DNS) or Large Eddy Simulation (LES), it is less expensive to solve for averaged quantities and approximate the impact of small fluctuating structures. There are different turbulent models to model these fluctuating

structures.

To obtain Reynolds-Averaged Navier-Stokes equation, each solution variable ϕ is expressed as the sum of averaged value $\bar{\phi}$ and its fluctuating component ϕ':

$$\phi = \bar{\phi} + \phi' \tag{3.3}$$

where ϕ represents the velocity components, pressure and energy.

Inserting the decomposed solution variables into the Navier-Stokes equation gives is the equation for mean quantities. The equation for mean quantities for incompressible flow can be written as

$$\boldsymbol{\nabla} \cdot \left(\overline{V}\right) = 0 \tag{3.4}$$

$$\frac{\partial(\overline{V})}{\partial t} + \boldsymbol{\nabla} \cdot \left(\overline{V} \otimes \overline{V}\right) = -\frac{1}{\rho}\boldsymbol{\nabla} \cdot (\bar{p}\mathbf{I}) + \frac{1}{\rho}\boldsymbol{\nabla} \cdot (\mathbf{T} + \mathbf{T_t}) + f_b \tag{3.5}$$

The above equations are similar to the original Navier-Stokes equation 3.1 and 3.2. The only difference is that the momentum equation has an additional term known as Reynolds stress tensor, which is given as

$$\mathbf{T_t} = -\rho \begin{pmatrix} \overline{u'u'} & \overline{u'v'} & \overline{u'w'} \\ \overline{u'v'} & \overline{v'v'} & \overline{v'w'} \\ \overline{u'w'} & \overline{v'w'} & \overline{w'w'} \end{pmatrix} \tag{3.6}$$

From equations 3.4, 3.5 and 3.6 we see that there are ten unknowns ($\bar{p}, u, v, w$ and the six elements of Reynolds stress tensor $\overline{u_i'u_j'}$) and only four equations. The challenge in Reynolds-Averaged Navier-Stokes Equation (RANSE) solver is to model $\mathbf{T_t}$ in terms of mean flow quantities and provide closure to the governing equations. Using Boussinesq approximation, the momentum transfer caused by turbulent eddies can be modeled using turbulent eddy

viscosity. The Reynolds stress tensor can be expressed as a function of mean flow quantities and turbulent eddy viscosity:

$$\mathbf{T_t} = 2\mu_t \mathbf{S} - \frac{2}{3}(\mu_t \boldsymbol{\nabla} \cdot \overline{V})\mathbf{I} \tag{3.7}$$

$$S = \frac{1}{2}(\boldsymbol{\nabla}\overline{V} + \boldsymbol{\nabla}\overline{V}^T) \tag{3.8}$$

where $\mathbf{S}$ is the mean strain rate tensor and $\overline{V}$ is the mean velocity.

There are simpler models that rely on the concept of mixing length to model the turbulent eddy viscosity. The eddy viscosity models solve additional transport equations for scalar quantities that can enable the turbulent eddy viscosity μ_t. Usually, these models assume that Reynolds stress tensor is linearly proportional to the mean strain rate and does not consider anisotropy of turbulence [4, 33, 54, 65]. There are some two-equation models that provide an option to extend the linear approximation to include non-linear constitutive relation [41, 42]. In this study $k-\omega$ SST turbulent model and $\gamma - Re_\theta$ transition model are used for CFD simulations. Sections 3.2.1 and 3.2.2 gives brief description of these models.

3.2.1 SST $k-\omega$ Turbulent Model

The $k-\omega$ turbulent model is a two-equation model that solves two additional transport equations for the turbulent kinetic energy k and the specific dissipation rate ω in order to determine the turbulent eddy viscosity [64]. This model is sensitive to inlet boundary conditions because the boundary layer computation depends upon the value of ω in the free-stream. This problem was resolved in SST $k-\omega$ turbulent model developed by Menter [44]. This model is similar to standard $k-\omega$ model with an additional non-conservative cross diffusion term containing $\boldsymbol{\nabla}k.\boldsymbol{\nabla}\omega$. This term is included far away from the wall using a blending dunction, but not near the wall.

The turbulent eddy viscosity is calculated as the product of turbulent kinetic energy k and turbulent time scale T

$$\mu_t = \rho k T; \quad T = min\Big(\frac{1}{\omega}, \frac{0.31}{SF_2}\Big); \quad F_2 = tanh\bigg(\Big(max\Big(\frac{2\sqrt{k}}{\beta^*\omega d}, \frac{500\nu}{d^2\omega}\Big)\Big)^2\bigg) \tag{3.9}$$

$$\beta^* = F_1\beta_1^* + (1-F_1)\beta_2^*; \quad F_1 = tanh\bigg(\Big[min\Big(max\Big(\frac{\sqrt{k}}{0.09\omega d}, \frac{500\nu}{d^2\omega}\Big), \frac{2k}{d^2 CD_{k\omega}}\Big)\Big]^4\bigg) \tag{3.10}$$

where S is the mean strain rate tensor, d is the wall distance, β_1^* and β_2^* are model coefficients. The cross diffusion coefficient $CD_{k\omega}$ is given as

$$CD_{k\omega} = max\Big(\frac{1}{\omega}\boldsymbol{\nabla}\cdot k \cdot \boldsymbol{\nabla}\cdot\omega, 10^{-20}\Big) \tag{3.11}$$

The transport equation for turbulent kinetic energy k and specific dissipation rate ω are

$$\frac{\partial}{\partial t}(k) + \boldsymbol{\nabla}\cdot\big(k\overline{V}\big) = \frac{1}{\rho}\boldsymbol{\nabla}\cdot[(\mu+\sigma_k\mu_t)\boldsymbol{\nabla}k] + P_k - \beta^*(\omega k - \omega_0 k_0) \tag{3.12}$$

$$\frac{\partial}{\partial t}(\omega) + \boldsymbol{\nabla}\cdot\big(\omega\overline{V}\big) = \frac{1}{\rho}\boldsymbol{\nabla}\cdot[(\mu+\sigma_\omega\mu_t)\boldsymbol{\nabla}\omega] + P_\omega - \beta(\omega^2 - \omega_0^2) \tag{3.13}$$

where $\sigma_k, \sigma_\omega, \beta^*, \beta$ are model coefficients, P_k, P_ω are production terms, k_0, ω_0 are the ambient turbulence values that counteracts turbulence decay. The further details on formulation of production terms P_k and P_ω can be found in Menter [44]. The value of all model coefficients used in $SST\ k-\omega$ turbulent model is given in Table 3.1.

3.2.2 $\gamma - Re_\theta$ Transition Model

The $\gamma - Re_\theta$ transition model proposed by Menter et al. [45] and applied by Langtry et al. [38] is an empirically derived correlation-based model that has been specifically formulated

Coefficient	Value
σ_k	$F_1\sigma_{k1} + (1 - F_1)\sigma_{k2}$
σ_{k1}	0.85
σ_{k1}	1
σ_ω	$F_1\sigma_{\omega1} + (1 - F_1)\sigma_{\omega2}$
$\sigma_{\omega1}$	0.5
$\sigma_{\omega1}$	0.856
β^*	$F_1\beta_1^* + (1 - F_1)\beta_2^*$
β_1^*	0.09
β_2^*	0.09
β	$F_1\beta_1 + (1 - F_1)\beta_2$
β_1	0.075
β_2	0.0828

Table 3.1: Model coefficients used in $SST\ k-\omega$ turbulent model

for unstructured CFD codes. This model is based on two additional transport equations, one for the intermittency γ and one for the transition onset momentum thickness Reynolds number $\overline{Re_{\theta t}}$, coupled with $SST\ k-\omega$ turbulent model [44]. This transition model provides a semi-local approach to predict the onset of transition in turbulent boundary layer and it relies on calibration from experimental data. The transport equation for the intermittency is formulated as

$$\rho\frac{D\gamma}{Dt} = \boldsymbol{\nabla}\cdot\left[(\mu + \frac{\mu_t}{\sigma_\gamma})\boldsymbol{\nabla}\gamma\right] + P_\gamma - E_\gamma \tag{3.14}$$

where P_γ and E_γ are the production and destruction terms given as

$$P_\gamma = F_{Length}C_{a1}\rho S[\gamma F_{onset}]^{1/2}(1 - C_{e1}\gamma) \tag{3.15}$$

$$E_\gamma = C_{a2}\rho W\gamma F_{turb}(C_{e2}\gamma - 1); \quad F_{turb} = exp\Big[-\Big(\frac{Re_t}{4}\Big)^4\Big] \tag{3.16}$$

where C_{a1}, C_{e1}, C_{a2}, C_{e2} are model constants. The value of these constants are $C_{a1} = 0.5$, $C_{e1} = 1.0$, $C_{a2} = 0.03$, $C_{e2} = 50$. F_{Length} is an empirical correlation that controls the length of transition region and this correlation is suggested by Suluksna et al. [57]. F_{onset} is a trigger function that describes the initiation of intermittency for different modes of transition. S

and W are the modulus of mean strain-rate tensor and mean vorticity tensor respectively. F_{turb} is used to disable the destruction/relaminarization sources outside of a laminar layer or in the viscous sublayer and it is a function of turbulent Reynolds number Re_t.

The transport equation of the transition momentum thickness Reynolds number $\overline{Re_{\theta t}}$ is formulated as

$$\rho\frac{D\overline{Re_{\theta t}}}{Dt} = \boldsymbol{\nabla}\cdot\left[(\mu+\frac{\mu_t}{\sigma_\gamma})\boldsymbol{\nabla}\overline{Re_{\theta t}}\right] + P_{\theta t} \tag{3.17}$$

where $P_{\theta t}$ is a source term designed to force the transported scalar $\overline{Re_{\theta t}}$ to match the local value of transition onset momentum thickness Reynolds number $Re_{\theta t}$ outside the boundary layer. The empirical relation for $Re_{\theta t}$ can be found in Langtry [37]. The transport equation for turbulent kinetic energy k used in $SST\ k-\omega$ is modified as below to be used in $\gamma - Re_\theta$ transition model

$$\frac{Dk}{Dt} = \frac{1}{\rho}\boldsymbol{\nabla}\cdot[(\mu+\sigma_k\mu_t)\boldsymbol{\nabla}k] + \gamma P_k - min[max(\gamma,0,1),1]\beta^*(\omega k - \omega_0 k_0)$$

where P_k is the production term from the turbulent kinetic energy equation in the original $SST\ k-\omega$ turbulent model [44].

3.3 SIMPLE Solution Algorithm

All the simulations in this study are performed using the segregated flow solver. This flow solver is suitable for constant-density flows and it solves conservation equations for mass and momentum in a sequential manner. The nonlinear governing equations are solved sequentially for the solution variable u, v, w, p. In this study, the segregated flow solver uses SIMPLE algorithm [52] as pressure-velocity coupling algorithm. In this algorithm, the mass conservation constraint is fulfilled by solving the pressure-correction equation. The pressure-

correction equation is constructed from continuity and momentum equation. The pressure is corrected in such a way that the predicted velocity field satisfies the continuity equation. This method is called a predictor-corrector approach. The SIMPLE algorithm is summarized below:

1. Set the boundary and initial conditions.

2. Compute the velocity and pressure gradients.

3. Solve the discretized momentum equation to get the intermediate velocity field V^*

4. Compute the uncorrected mass fluxes at faces $\dot{m}_f^*$

5. Solve the pressure correction equation. This creates cell values for the pressure correction p'

6. Update the pressure field

$$p^{n+1} = p^n + \omega p' \tag{3.18}$$

where ω is the under-relaxation factor for pressure

7. Correct the face mass fluxes

$$\dot{m}_f^{n+1} = \dot{m}_f^* + \dot{m}_f' \tag{3.19}$$

8. Correct the cell velocities

$$V_p^{n+1} = V_p^* - \frac{Vol \boldsymbol{\nabla} p'}{a'^v_p} \tag{3.20}$$

where $\boldsymbol{\nabla} p'$ is the gradient of pressure correction, a'^v_p is the vector of central coefficients for the discretized velocity equation, and Vol is the cell volume.

3.4 Modeling Techniques for the Propeller

There is a number of ways in which the effect of the propeller can be modeled in StarCCM+. Each of these methods decides the accuracy of the solution and the computational efforts needed.

3.4.1 Moving Reference Frame

The average effect of the propeller can be modeled using steady-state moving reference frame approach. This approach takes into account the effect of the shape of the propeller. This approach requires a cylindrical region surrounding the propeller. The rotating reference frame is applied to the cylindrical region which contains the propeller. This approach does not change the relative position of the cell vertices, but it imposes a body forces induced by the rotation. The body force is calculated based on the properties of the reference frame and not the actual motion of cell vertices.

There is an interface between the cylindrical domain and the stationary region. The local variables are transferred from one reference frame to another on a cell-by-cell basis at the interface. Since there is no motion there is no change in relative cell position at the interface. The rotating reference frame is specified relative to a stationary (laboratory) reference frame. This approach is particularly suitable for axisymmetric flows. If any component of the flow is perpendicular to the axis of rotation, then the results proportional to the axis of rotation might not be correct.

Fig. 3.1 shows the stationary lab reference frame and moving reference frame. The velocity of point P relative to moving reference frame is given as

$$V_r = V - \omega_{MRF} \times r_{P,MRF} \tag{3.21}$$

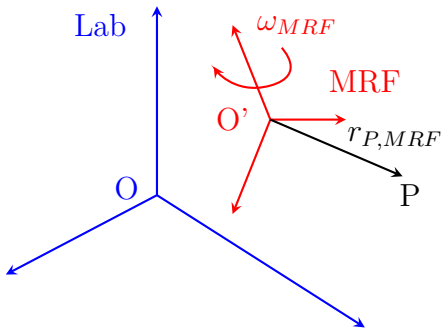

Figure 3.1: Stationary lab reference frame and moving reference frame

where V_r is the relative velocity, V is the velocity in lab reference frame, ω_{MRF} is the angular velocity of moving reference frame, and $r_{P,MRF}$ is the position vector with respect to the moving reference frame.

The continuity and momentum equation in moving reference frame are given ass

$$\boldsymbol{\nabla} \cdot V_r = 0 \tag{3.22}$$

$$\frac{\partial}{\partial t}(V) + \boldsymbol{\nabla} \cdot V \otimes V_r = -\frac{1}{\rho}\boldsymbol{\nabla} \cdot (p\mathbf{I}) + \frac{1}{\rho}\boldsymbol{\nabla} \cdot \mathbf{T} + f_b - \omega \times V \tag{3.23}$$

For the stationary reference frame $V_r = V$. In this study, moving reference frame approach is used for studying the open water performance of propeller and for optimization of propulsor geometry.

3.4.2 Sliding Mesh

In order to take into account the full effect of the propeller, including propeller-hull interaction, flow at an inclined angle, propeller-rudder interaction we can use unsteady sliding mesh approach for modeling the propeller. The propeller is fully simulated using transient simulation with time-step adjusted to resolve the rotation of the propeller.

In this approach, the region containing the propeller rotates by fixed angular rotation per

time step. For each time step, the interfaced region slides the mesh to the new position according to the user-defined motion. This is the most accurate approach to simulate the moving parts, but this approach is the most computationally intensive. This approach takes into account the flow effects such as blade passing, inclined propeller shaft, and interaction with a free surface. The mesh velocity is defined as

$$V_g = \omega_g \times r \tag{3.24}$$

where ω_g is the angular velocity of the rotating region and r is the position vector of mesh vertex. The continuity and momentum equation for rigid body motion are

$$\boldsymbol{\nabla} \cdot (V - V_g) = 0 \tag{3.25}$$

$$\frac{\partial}{\partial t}(V) + \boldsymbol{\nabla} \cdot V \otimes (V - V_g) = -\frac{1}{\rho}\boldsymbol{\nabla} \cdot (p\mathbf{I}) + \frac{1}{\rho}\boldsymbol{\nabla} \cdot \mathbf{T} + f_b - \omega \times V \tag{3.26}$$

The grid velocity is calculated based on the under-defined rotation rate and the axis of rotation. The time step for transient simulation should be selected in such a way that the convective courant number is not very high, as this might cause divergence.

3.5 Hydrodynamic Forces and Moments

The thrust and the torque of the propulsor are two main types of forces that are used in this study to measure the performance of propulsor. The thrust is an axial force acting on the body as a result of fluid dynamic pressure and shear stress due to surrounding fluid. The

total force on the propeller in the normal direction $\vec{n}$ is given as

$$\vec{F_n} = \sum_c (\vec{F_c}^{pressure} + \vec{F_c}^{shear}) \cdot \vec{n} \tag{3.27}$$

$$\vec{F_c}^{pressure} = p_c \cdot \vec{a_c} \tag{3.28}$$

$$\vec{F_c}^{shear} = -T_c \cdot \vec{a_c} \tag{3.29}$$

where p_c, T_c, a_c are the pressure tensor, shear stress tensor and the cell area vector.
The torque of the propeller is due to moment acting from fluid dynamics pressure and shear stress about the reference axis. The moment about an axis $\vec{n}$ passing through x_0 is given by

$$M_n = \sum_c \vec{r_c} \times (\vec{F_c}^{pressure} + \vec{F_c}^{shear}) \cdot \vec{n} \tag{3.30}$$

where $\vec{r_c}$ is the position vector with respect to x_0

Chapter 4

Propeller Design

There are different classes of methods that can be used for designing the propeller. Carlton [16] gives an overview of different methods that have been developed over the years for designing the propeller. OpenProp is an open-source tool based on lifting line theory used for designing the propeller operating at low or moderately loaded condition [21]. OpenProp takes the parameters such as the diameter, number of blades, ship speeds etc. as an input from users and generates the propeller geometry that gives optimum circulation distribution. Kinnas and Fine [34] developed a boundary element method code PROPCAP to solve for the unsteady effects such as cavitaion around the propeller subjected to non-axisymmetric inflow. Recently, the geometry of different types of propellers are optimized using Panel Method solver for analyzing the flow around the propeller, parametric geometry definition for the propeller geometry and multi-fidelity optimization algorithms [14, 24]. These methods give accurate results especially at design operating condition. However, at off-design condition hydrodynamic modeling of trailing vortex wake of the propeller is a challenging task [23]. Also, for ducted propellers the interaction between tip gap flow and duct boundary layer is critical and robust method is needed to take these effects into account [5].

The inviscid approximation in potential flow methods is good for high Reynolds number flow and around the design advance coefficient. However, at low Reynolds number the effect of viscosity should be taken into account. Also, at low Reynolds number the stall occurs at low angle of attack due to laminar or transitional flow on the surface of the propeller. Drela

and Giles [19] proposed a viscous/inviscid analysis methods for low Reynolds number flows. In this method, the inviscid part of the flow field was represented by Euler equation and a two-equation integral formulation based on dissipation closure for laminar and turbulent flows is proposed within the boundary layer. The coupled viscous/inviscid methods gives good results for the drag over narrow range of angle of attacks, but the solution diverges if significant region of flow separation exists on the surface of an airfoil (i.e. off-design advance coefficients). When the propeller operates in transitional flow regime (Re $< 10^6$) the flow is usually separated on the surface of the propeller.

The propeller designed for this study is highly loaded and operates in transitional flow regime. Brizzolara et al. [12] showed the capability of RANSE solver to analyze the flow around propeller at lower advance ratios. i.e. high loading condition where the viscous effect of boundary layer and eventually separation are critical. Recent development in transition model has made it possible to simulate laminar to turbulent transition and these models can capture both natural transition and separation-induced transition [66]. Number of studies done recently shows that transition model has the capability to simulate laminar to turbulent transition on model scale propellers [7, 9, 62]. Hence, simulation-based design using RANSE solver with transition model as discussed in section 3.2.2 is used for this study. In this chapter, we discuss about the CFD model, meshing strategies, validation and results of CFD simulation.

4.1 Model Setup, Verification and Validation

The propeller considered in this study for validation is the propeller C from study carried out by Kuiper [35]. Four propellers were studied for laminar to turbulent boundary layer transition at model scale in this study. Paint pattern data is available on the suction and

pressure side of the surface of this propeller. In addition, the chord-wise location of laminar to turbulent flow transition on pressure and suction side of the propeller is available for two different loading conditions and two different Reynolds number. Also the thrust and torque were measured for this propeller from advance ratio $J = 0$ to 1 at higher Reynolds number. The validated CFD model is then used for investigating ducted propeller K_a-4-70 inside the duct 19A. The accelerating duct 19A has $L/D = 0.5$ and is used for higher loading condition like bollard pull condition. The geometry of the propeller is available in the form of back and face coordinates at various radial location [51]. The details of geometrical parameters for K_a series screw propeller are given in Appendix B. The gap between the propeller tip and the duct is 0.83 % of the propeller radius. The geometrical details of both propellers are given in Table 4.1.

Parameter	**Open Propeller**	**Ducted Propeller**
Number of blades	4	4
Diameter (m)	0.3	0.24
A_E/A_O	0.63	0.7
$C_{0.7}/D$	0.43	0.36
$t/C(0.7)$	0.022	0.038

Table 4.1: Geometry of two propellers used in this study

Both propellers are modeled with front hubcap and downstream shaft following the open water setup with full cylindrical fluid domain. The cylindrical domain extends $3D$ from the propeller plane to the inlet, $6D$ from propeller plane to the outlet and with a radius of $4D$, where D is the propeller diameter. The computational domain is divided into two regions, stationary region and rotating region. In this study, steady state Moving Reference Frame (MRF) (as discussed in Section 3.4.1) approach is used because it requires less computation time as compared to unsteady sliding mesh approach (as discussed in Section 3.4.2). The rotating domain extends $0.5D$ upstream from the propeller plane and $0.5D$ downstream from

the propeller plane. Fig. 4.1 shows the geometry of open propeller, ducted propeller, and computational domain used for CFD simulations.

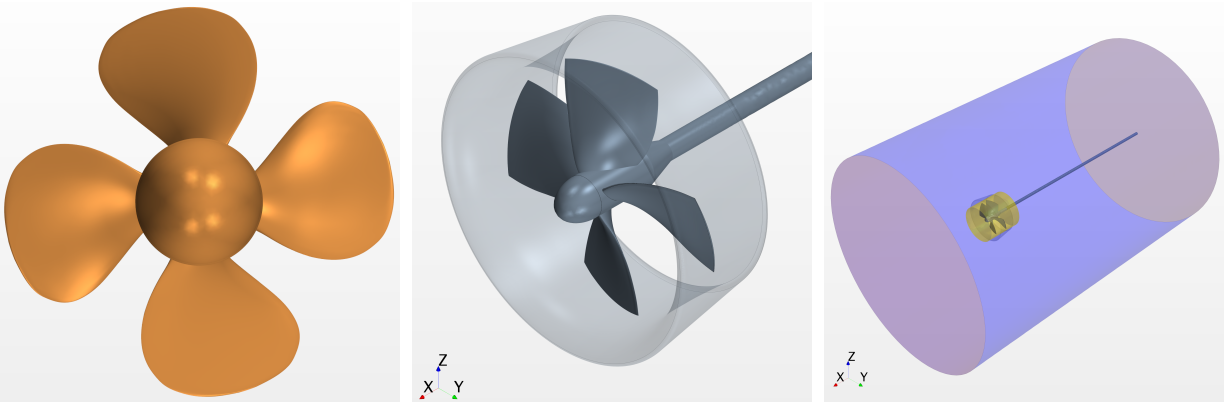

(a) Open Propeller (b) Ducted Propeller (c) Computational Domain

Figure 4.1: Geometry of two propellers used for CFD model validation and computational domain used for the CFD model

Table 4.2 gives the boundary conditions that were used for the CFD calculations. For open propeller, turbulent intensity is available from the experimental setup [36] and turbulent viscosity ratio is obtained by tuning inlet parameters for transition model (as discussed in section 4.1.2.1). Both turbulent intensity and turbulent viscosity ratio are obtained by tuning inlet parameters based on hydrodynamic forces for ducted propeller. Second-order upwind scheme is used for the discretization of momentum equation. For turbulence model, second-order upwind scheme is used.

4.1.1 Grid Generation and Mesh Sensitivity Analysis

The computational domain is discretized using unstructured polyhedral cells including the prism layers on the wall surface. The first cell height for prism layer is calculated in such a way that wall $y+ \approx 1$ is achieved on the surface of the propeller. The propeller has very small leading edge radius and a very small gap between the propeller tip and the duct. Hence, very

Boundary	**Velocity**	**Pressure**	**Turbulent Intensity**	**Turbulent Viscosity Ratio**
Inlet	Constant (Based on value of J)	$\frac{\partial P}{\partial n} = 0$	3% (Open), 1% (Ducted)	30 (Open), 10 (Ducted)
Outlet	$\frac{\partial V}{\partial n} = 0$	Ambient Pressure	1%	10
Cylinder Surface	$\frac{\partial V}{\partial n} = 0$	$\frac{\partial P}{\partial n} = 0$	Wall function	Wall function
Propeller, Duct, Hub, Shaft	No Slip	$\frac{\partial P}{\partial n} = 0$	Wall function	Wall function
Rotating/ Stationary region interface	Internal Interface	Internal Interface	Internal Interface	Internal Interface

Table 4.2: Boundary conditions used for the CFD model

fine meshing is needed in these regions to capture the flow correctly. To get accurate flow prediction in these regions, volumetric controls are created in the form of a cylinder which covers the leading edge and tip of each propeller blade. The interface between rotating and stationary region has two prism layers on both side for smooth movement of flow from one region to another. Fig. 4.2 shows various types of refinement zones created for the ducted propeller. Similar refinement zones were also created around the open propeller.

Table 4.3 gives the details of mesh parameters that were used to perform mesh sensitivity analysis. Three grids were used to do mesh sensitivity analysis. Fig. 5.3a - 4.3c shows the prism layer around the surface of open propeller at $^{r}/_{R} = 0.7$ for three meshes used. Fig. 4.3d - 4.3f shows the mesh on the propeller and the duct for three grid sizes used in this study. Fig. 4.4 and 4.5 shows the wall $y+$ on the surface of propeller blades for open and ducted propeller. It can be observed that as the mesh becomes finer leading edge separation and trailing edge separation is better predicted. For mesh sensitivity analysis, the hydrodynamic coefficients are compared with experimental results at advance coefficient

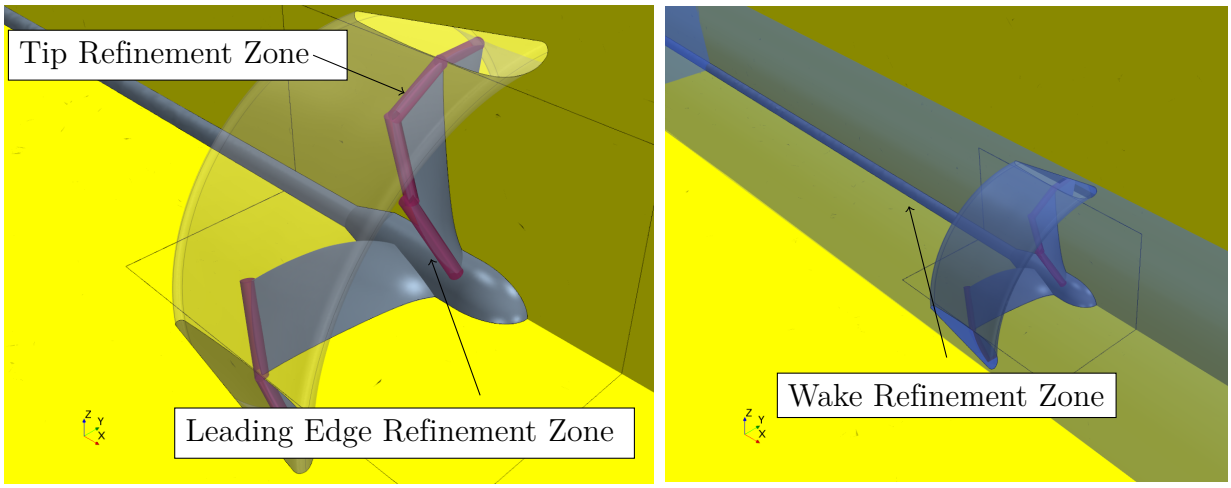

Figure 4.2: Various mesh refinement zones created in computational domain around the propeller's leading edge and the tip

$J = 0.4$ and $J = 0.3$ for open and ducted propeller respectively. Hydrodynamic coefficients of open and ducted propeller are calculated as below

$$K_{TP} = \frac{T_P}{\rho n^2 D^4}; \quad K_{TN} = \frac{T_N}{\rho n^2 D^4}; \quad K_Q = \frac{Q}{\rho n^2 D^4}; \quad K_T = K_{TP} + K_{TN}; \quad \eta = \frac{J}{2\pi}\frac{K_T}{K_Q}$$

where T_P, T_N, Q, J is the propeller thrust, duct thrust, propeller torque and advance coefficient respectively.

The results of mesh sensitivity analysis for open propeller are given in Fig. 4.6a. The forces predicted by all three meshes are almost the same and that might be due to the same first cell layer height in the prism layer. For different first cell layer height in different meshes, different wall functions will be used based on the value of $y+$ since we are using all-$y+$ treatment. In order to make sure that the same wall treatment is used for all three meshes, the first cell height is kept the same. The relative error between experimental torque coefficient and CFD torque coefficient reduces from 1.45% to 1.27% from coarse mesh to fine mesh. The results for ducted propeller are presented in Fig. 4.6b. The relative error of torque coefficient

	Fine	**Medium**	**Coarse**
Cell type	Polyhedral	Polyhedral	Polyhedral
Target surface mesh size- Propeller	0.25 % D	0.3125 % D	0.375 % D
Target surface mesh size- Duct	0.67 % D	0.84 % D	1 % D
Surface mesh size- LE and Tip volume	0.17 %D	0.21 % D	0.25 % D
Surface mesh size- Rotating region volume	3.3 % D	4.1 % D	5 % D
Prism layer thickness	3.2 mm (Ducted), 2.5 mm (Open)	3.2 mm (Ducted), 2.5 mm (Open)	3.2 mm (Ducted), 2.5 mm (Open)
Number of prism layers	25	20	15
Maximum Wall Y+	25	20	15
Cell count	24.7 M (Ducted), 28.3 M (Open)	13.7 M (Ducted), 15.7 M (Open)	8.5 M (Ducted), 11.8 M (Open)

Table 4.3: Mesh parameters for three grids used for mesh sensitivity study

reduces from 0.82% to 0.77% from coarse mesh to fine mesh. In the case of thrust coefficient, all meshes overpredict the thrust and the relative error changes from 1.69 % to 1.95% from coarse mesh to fine mesh. No monotonic convergence is found, but it is believed that the experimental measurement uncertainty is in the same order of magnitude of the deviation of the numerical prediction error.

4.1.2 Validation Study for Open Propeller

In this section, the validation of CFD model for open propeller with the experimental results found by Kuiper [35] is presented. In these experiments, the boundary layer on the surface of the propeller were investigated related to the cavitation inception. The local characteristics such as location of laminar to turbulent transition and global characteristics like hydrodynamic forces are compared between the CFD simulation results and experimental results.

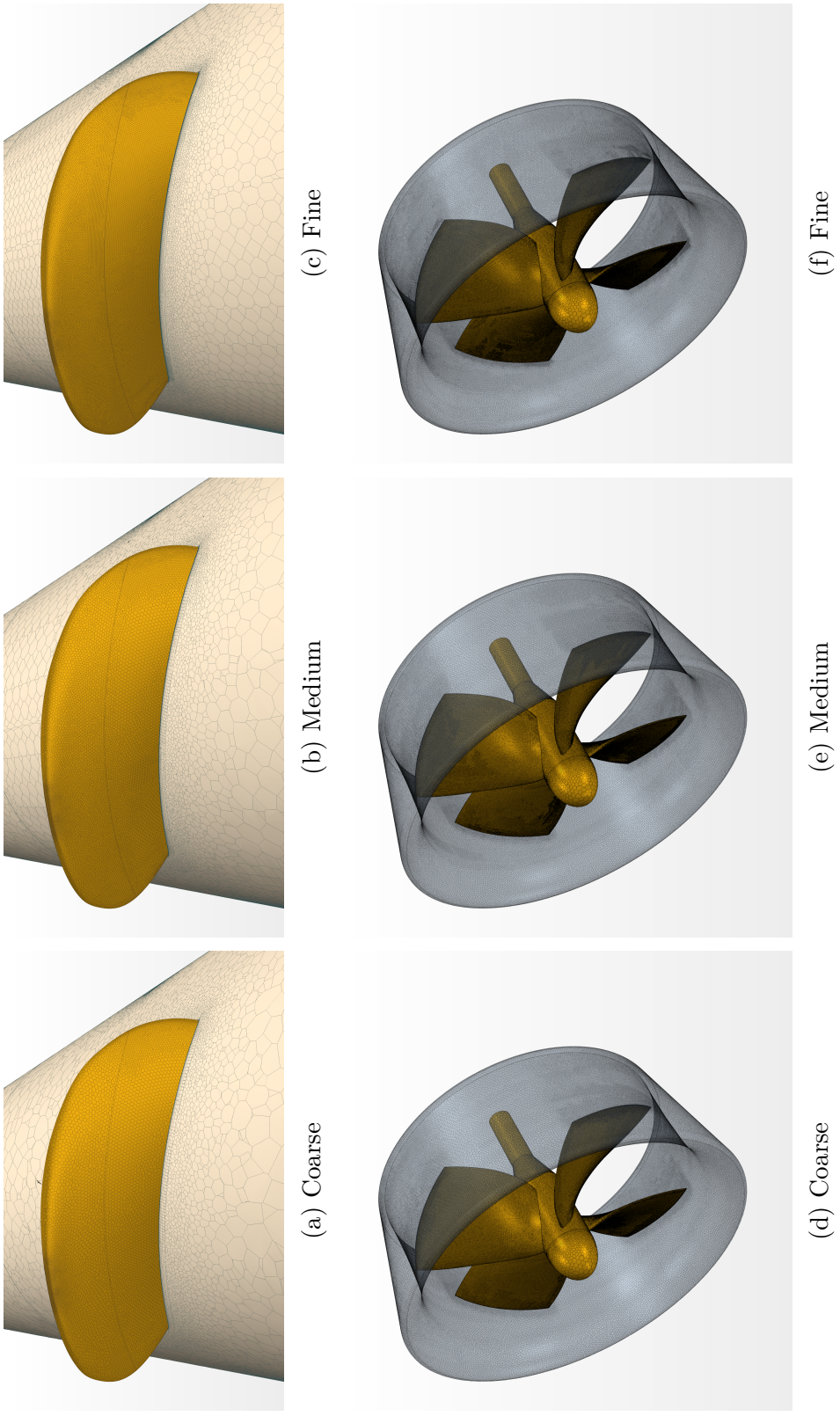

Figure 4.3: Particulars of the mesh scenes for open and ducted propeller

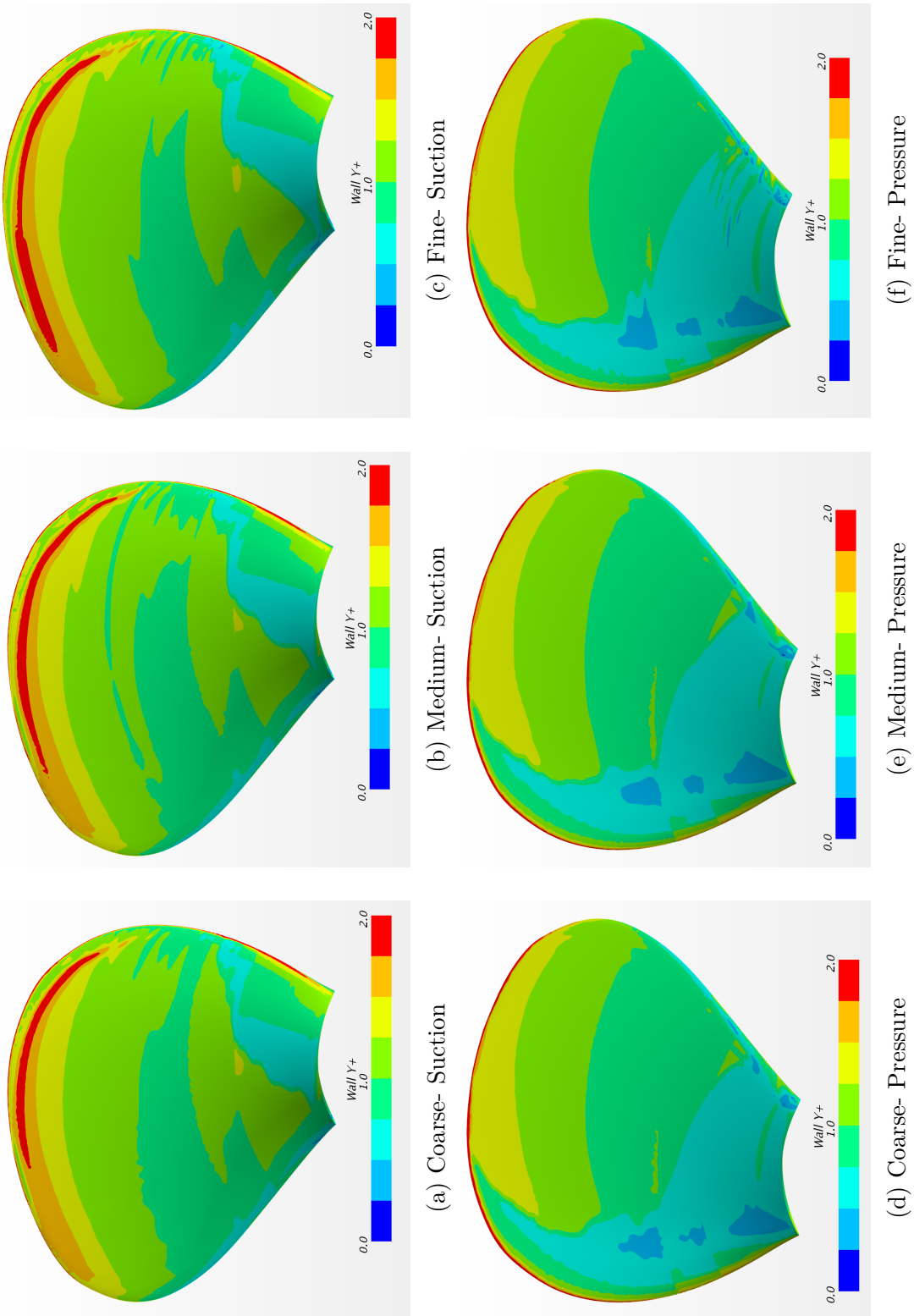

(a) Coarse- Suction (b) Medium- Suction (c) Fine- Suction

(d) Coarse- Pressure (e) Medium- Pressure (f) Fine- Pressure

Figure 4.4: Wall Y+ on the surface of open propeller for different types of mesh

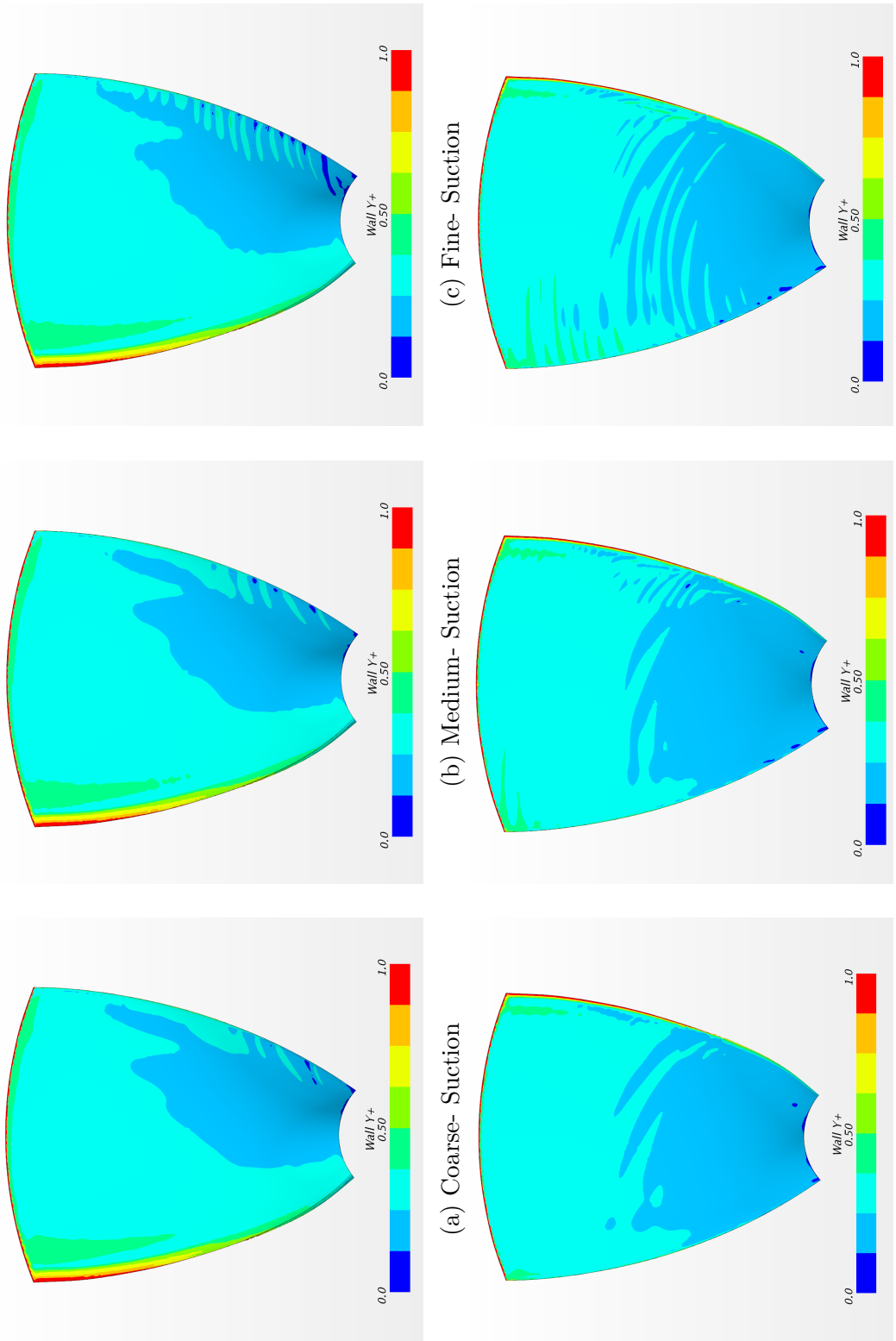

(a) Coarse- Suction (b) Medium- Suction (c) Fine- Suction

(d) Coarse- Pressure (e) Medium- Pressure (f) Fine- Pressure

Figure 4.5: Wall Y+ on the surface of propeller K_a-4-70 inside the duct for different types of mesh

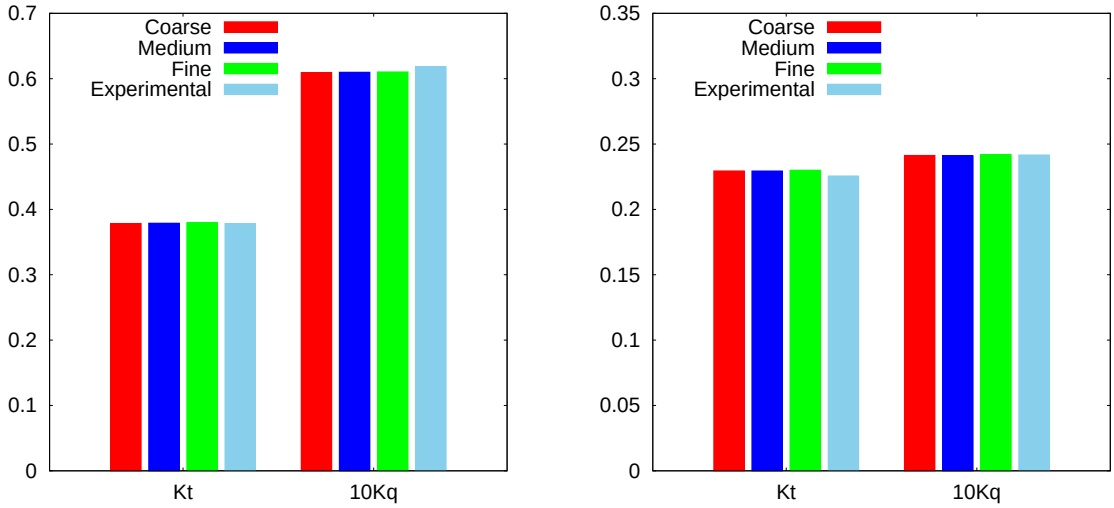

(a) Open Propeller (b) Ducted Propeller

Figure 4.6: Mesh sensitivity analysis results for open propeller at $J = 0.4$ and for ducted propeller at $J = 0.3$

4.1.2.1 Influence of Turbulence inlet parameters

The $\gamma - Re_\theta$ transition model takes into account the effect of freestream turbulence levels on the transition location. Hence, the special attention should be given to the inlet turbulence parameters when using the transition model. Since the inlet boundary is located at $4D$ upstream from the propeller plane, there is a decay of turbulent kinetic energy from inlet boundary to the propeller region. The decay in turbulent intensity and turbulent viscosity ratio from inlet to the propeller plane is given by below equations.

$$I = I_{inlet}[1 + \frac{0.1242 x \rho U_\infty I_{inlet}^2}{\mu TVR_{inlet}}]^{-0.5435} \tag{4.1}$$

$$TVR = TVR_{inlet}[1 + \frac{0.1242 x \rho U_\infty I_{inlet}^2}{\mu TVR_{inlet}}]^{-0.087} \tag{4.2}$$

where x is the distance in streamwise direction from inlet plane, I_{inlet} is turbulent intensity at the inlet, TVR_{inlet} is the turbulent viscosity ratio at the inlet and U_∞ is the freestream

velocity.

The higher value of turbulent viscosity ratio will reduce the decay in turbulent intensity significantly. However, a rough guideline is that the turbulent viscosity ratio should be lower than the turbulent viscosity occurring within the boundary layer. In order to have the same turbulent kinetic energy in the propeller region as the inlet boundary, additional source term is added in the turbulent kinetic energy transport equation. An ambient source option in StarCCM+ keeps the turbulence intensity constant over the domain. For the experimental setup, there was 3% disturbance in the velocity in the upstream region of the propeller [36]. Hence, the turbulent intensity is kept constant at $TI = 3\%$ and three values of turbulent viscosity ratio are considered: $TVR = 10$, 30 and 100. Fig. 4.7 shows the skin friction coefficient contour on the suction and pressure side of the propeller for different values of turbulent viscosity ratio at 60% slip. The slip is defined as the ratio of the difference between theoretical travel (pn) and actual travel (V_a) to theoretical travel. The skin friction coefficient is calculated using an effective velocity $V_E = \sqrt{V_A^2 + (2\pi nr)^2}$ at each radial location. The skin friction coefficient magnitude on the surface of propeller results in a range of values that lies in laminar to turbulent transition region friction coefficient for the flat plate at given Reynolds number. The extent of the turbulent region on the surface of the propeller increases with an increase in turbulent viscosity ratio.

Fig. 4.8 shows the location of transition for different values of TVR for 60% slip and chord-based Reynolds number of $0.665 \cdot 10^6$. The Reynolds number is based on $r/R = 0.7$ location. It can be clearly seen that the location of transition shifts toward leading edge with an increase in TVR. The results are in good agreement with the experimental results for $TVR = 30$. The CFD results for the position of transition are further compared for two Reynolds number and two loading conditions. Fig. 4.9 shows the comparison of chord-wise position of transition at $r/R = 0.7$. The transition model predicts the transition position

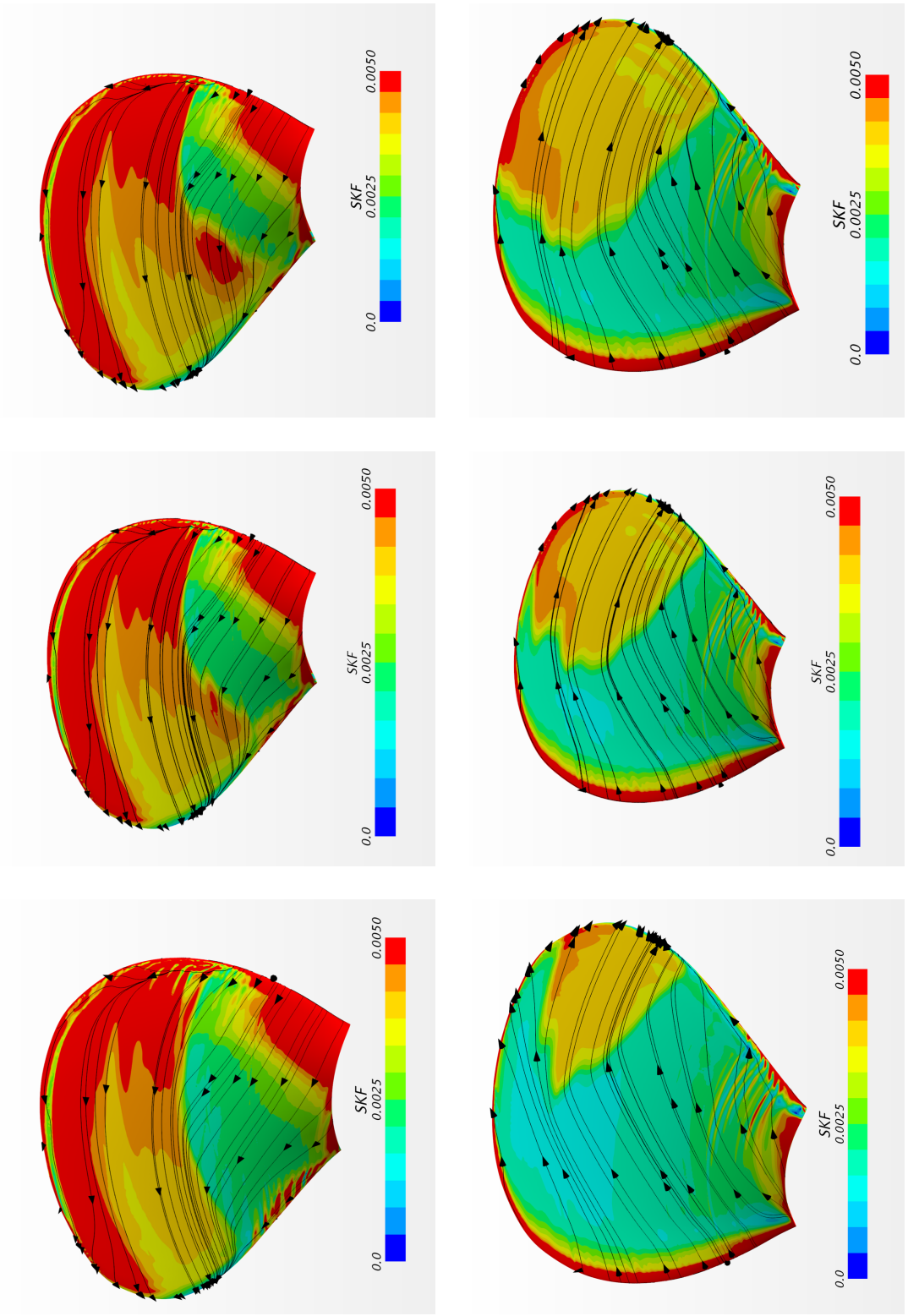

(a) TVR= 10 (b) TVR= 30 (c) TVR= 100

Figure 4.7: Skin Friction Coefficient Contour for TI= 3% and different values of Turbulent Viscosity Ratio at 60% slip. Top: Suction side, Bottom: Pressure side

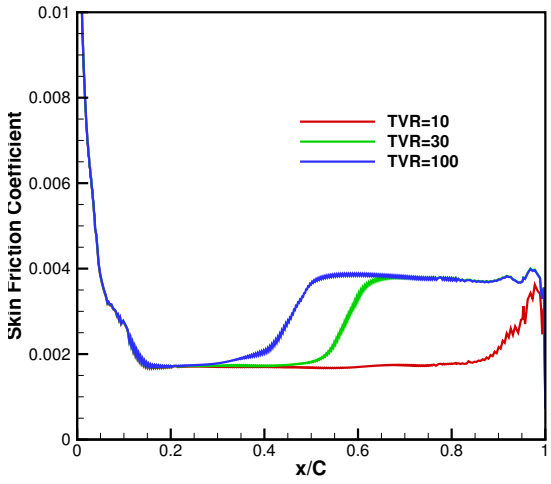

Figure 4.8: Effect of turbulent viscosity ratio on location of laminar- turbulent transition at 60% slip

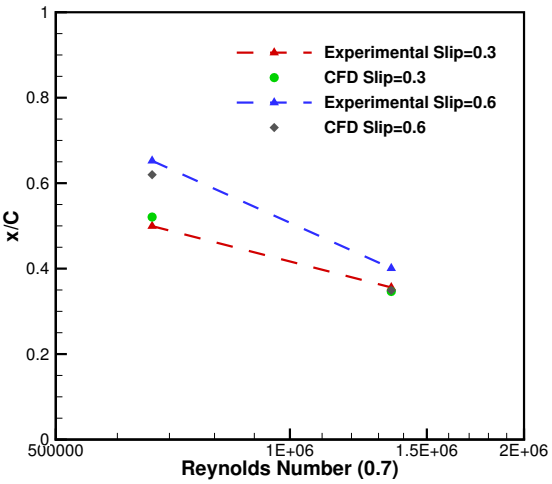

Figure 4.9: Location of laminar to turbulent transition for two different loading conditions and two Reynolds number

correctly for 30% slip which is a light loading condition. At higher loading condition of 60% slip, the transition model predicts earlier transition to turbulent flow than the experimental results.

4.1.2.2 Paint Pattern Visualization

In this section paint pattern is compared for open propeller at 30% slip and $Re_N = 0.66 \cdot 10^6$ where $Re_N = {}^{nD^2}/_{\nu}$. The streamline pattern on the surface of propeller gives an indication of the relative strength of the centrifugal force and tangential force. Tangential forces are due to friction between the fluid and the propeller. Based on the laminar or turbulent region, the frictional forces vary and hence the direction of streamlines changes depending upon the dominant force. Hence, if streamlines are directed in the radial direction then the centrifugal forces are dominant and hence the flow is in the laminar region. If the streamlines are directed in the tangential direction, then tangential forces are dominant and hence the flow is in the turbulent region. In addition, the skin friction coefficient is higher in case of

turbulent flow than for the laminar flow. Therefore skin friction coefficient increases as flow changes from laminar to turbulent flow.

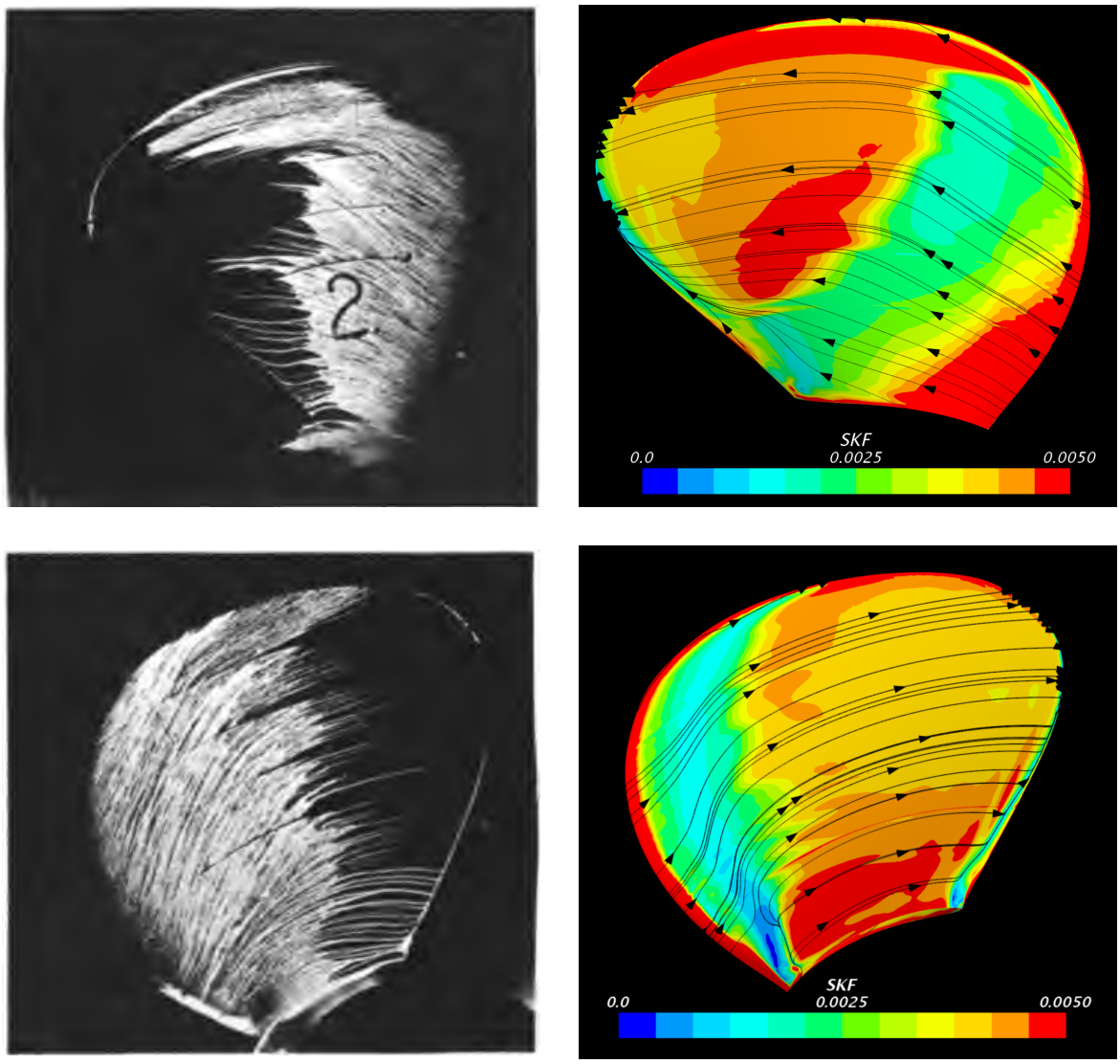

Figure 4.10: Comparison of paint pattern on the surface of propeller blade [35] with constrained streamline pattern and contours for skin friction coefficient for 30% slip and $Re_N = 0.66 \cdot 10^6$. Top: Suction, Bottom: Pressure

The results of the paint test on the propeller surface are compared with the constrained streamlines for wall shear stress. Fig. 5.12 shows that there is a good qualitative agreement

is obtained between the paint test and the transition model results. The transition model is able to predict the change in orientation of streamlines due to transition. The transition model predicts larger turbulent region especially on the pressure side as compared to the experimental results. The streamline direction matches with the paint pattern in the region near the hub up to $r/R = 0.5$. In the outer region there is an earlier transition to turbulent flow as compared to experimental results on both suction and pressure side.

4.1.2.3 Open Water Performance Comparison

In this section open-water performance is presented for the open propeller. The results are compared with experimental data obtained by Kuiper [35] for propeller C. The open-water forces were calculated at $Re_N = 2.9E6$ and same rotational speed of the propeller is used for CFD simulations. The magnitude of inlet velocity is calculated based on advance coefficient. For open-water performance calculation same turbulent inlet parameters (Tu = 3% and TVR= 30) are used at all advance coefficient. For all the force and moment measurement, both pressure and viscous forces are integrated over the surface of the propeller blades.

The comparison of the thrust and torque coefficient calculated using CFD model and experimental results are presented in Fig.4.11. The difference between numerical results and experimental results for thrust and torque coefficient is within 5% up to advance coefficient $J = 0.7$. The thrust predicted by CFD simulation is up to 15% less than the experimental results at advance coefficients higher than $J = 0.7$. At $J = 1.0$ the thrust of the propeller is near zero value and the absolute error between the numerical and experimental results is small. At these advance coefficients, the torque coefficient is up to 8% lower than the experimental results. This shows that the transition model is able to capture the boundary layer transition correctly at all advance coefficients. The efficiency calculated using CFD simulation is within 7% at all advance coefficient.

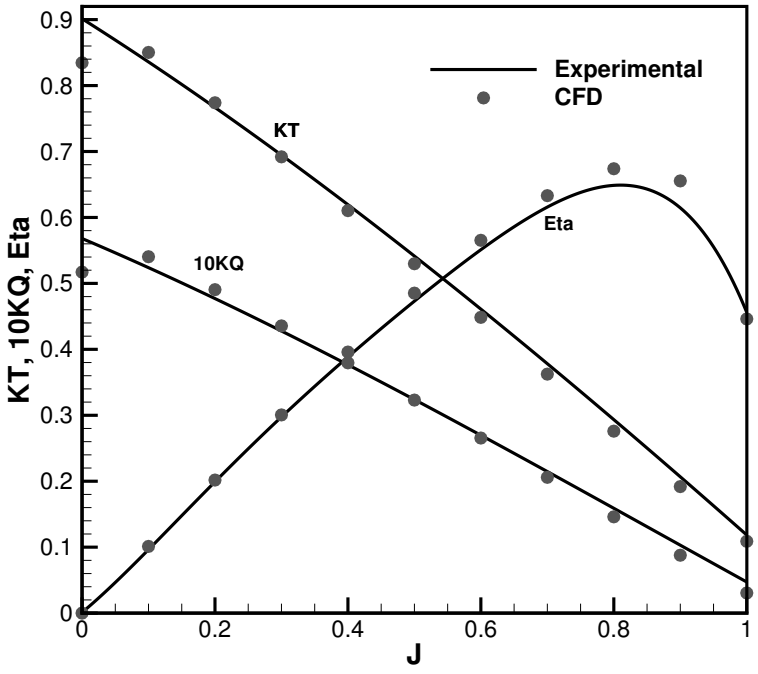

Figure 4.11: Open-water performance comparison for open propeller calculated using RANSE solver with transition model and experimental results [35]

4.2 Ducted Propeller Hydrodynamic Analysis

In this section, local and global hydrodynamic characteristics are presented for propeller K_a-4-70 with P/D=0.8 inside the duct 19A. The geometrical details of this propeller are given in Table 4.1. The speed of rotation of this propeller was kept constant at $n = 6.3$ rps for open-water performance measurement. The Reynolds number of flow on the surface of propeller ranges from $1.4 \cdot 10^5$ to $4.7 \cdot 10^5$. At this Reynolds number, the flow is in the transitional region on the surface of the propeller.

4.2.1 Influence of Turbulence inlet parameters

As discussed in case of the open propeller (Section 4.1.2.1), the $\gamma - Re_\theta$ transition model results strongly depend upon the turbulent inlet parameters. Hence different values of turbulent intensity and turbulent viscosity ratio are used and its influence on hydrodynamic coefficients is considered. For all the turbulent inlet parameters, the ambient source option was used which keeps the turbulent intensity constant over the domain as the inlet boundary. In all these cases, the advance coefficient was kept constant at $J = 0.5$.

For the propeller K_a-4-70 the paint pattern data is not available and hence we cannot compare the constrained streamlines on the surface of the propeller. We can compare hydrodynamic coefficients for different turbulent inlet parameters to find the correct parameters for the transition model. The hydrodynamic coefficients for different turbulence inlet parameter are given in Table 4.4. It can be seen that the thrust of the propeller and the duct is not influenced by turbulent inlet parameters as compared to the torque coefficient.

Turbulent Intensity	**Turbulent Viscosity Ratio**	K_{TN}	K_{TP}	K_T	$10K_Q$
Experimental Results		0.007	0.109	0.117	0.186
1%	10	0.015	0.117	0.131	0.192
3%	10	0.017	0.117	0.134	0.201
5%	10	0.018	0.118	0.136	0.208
5%	100	0.017	0.118	0.135	0.212

Table 4.4: Effect of turbulence inlet parameters on hydrodynamic coefficients of the propeller

As the turbulent intensity increases, we see that the torque coefficient also increases. The shear stress is higher for turbulent flow than the laminar flow. As the torque of the propeller depends upon the shear stress, a higher value of torque suggests that the boundary layer on the surface of the propeller is mainly turbulent. At model scale, the flow on the surface of the propeller is in transition regime and hence the turbulent inlet parameters (Tu= 1% and

TVR= 10) are suitable for the transition model.

4.2.2 Open Water Performance Comparison

In this section open-water performance is presented for the ducted propeller. The results are compared with experimental data obtained by Oosterveld [51] for propeller K_a-4-70 with P/D=0.8. For all advance coefficients, the speed of rotation of the propeller was kept constant at $n = 6.3\ rps$ and inlet velocity is changed to get the required value of J. For open-water performance calculation same turbulent inlet parameters (Tu = 1% and TVR= 10) are used at all advance coefficient. Both pressure and viscous forces are integrated over the surface of the propeller blades for force and moment calculation.

The comparison of the thrust and torque coefficient calculated using CFD simulation and experimental results are presented in Fig. 4.12a for transition model. The hydrodynamic coefficients calculated using transition model and fully turbulent model are compared in 4.12b. The total thrust coefficient is within 5% at all advance coefficients except for at $J = 0.5$ for both fully turbulent and transition model. The torque coefficient is within 4% at all advance coefficient for the transition model. However, the fully turbulent model overpredicts the torque coefficient by more than 5% at all advance coefficients (as seen in Fig. 4.12b). This suggests that the transition model is able to capture the correct boundary layer on the surface of the propeller than the fully turbulent model. The difference between the experimental and numerical results for duct thrust is larger at higher advance coefficient. At higher advance coefficient the duct thrust is very small and the absolute error between CFD results and experiment is very small. Baltazar et al. [6] made similar observations for the duct thrust at higher advance ratios.

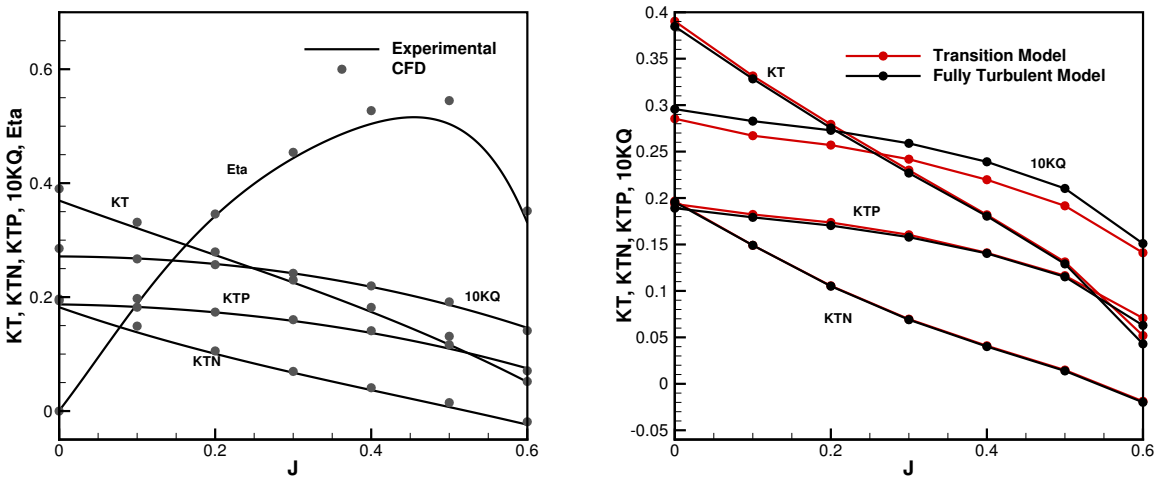

(a) $\gamma - Re_\theta$ Transition model (b) Transition and Turbulent model

Figure 4.12: Open-water performance comparison for Ducted propeller K_a-4-70 with P/D=0.8 inside the Duct 19A for transition model (left) and experimental results [51]. Comparison of hydrodynamic coefficients for fully turbulent and transition model (right)

4.2.3 Flow Pattern Analysis

In order to understand the difference in torque coefficient predicted by turbulent and transition model in section 4.2.2, the constrained streamline pattern with skin friction coefficient is compared for both transition and fully turbulent model at three different loading conditions.

Fig. 4.13 and 4.14 shows the constrained streamline pattern on pressure and suction side of the propeller for three loading conditions respectively. It can be clearly seen that the skin friction coefficient predicted using fully turbulent model is higher than the transition model at all loading conditions. The constrained streamline pattern is in tangential direction over the surface of the propeller for the fully turbulent model. The transition model predicts the constrained streamlines in a radial direction indicating that the flow is in the laminar-turbulent transition region and centrifugal forces are significant in comparison to tangential shear stress. The transition model predicts trailing edge separation which is not predicted

by the fully turbulent model.

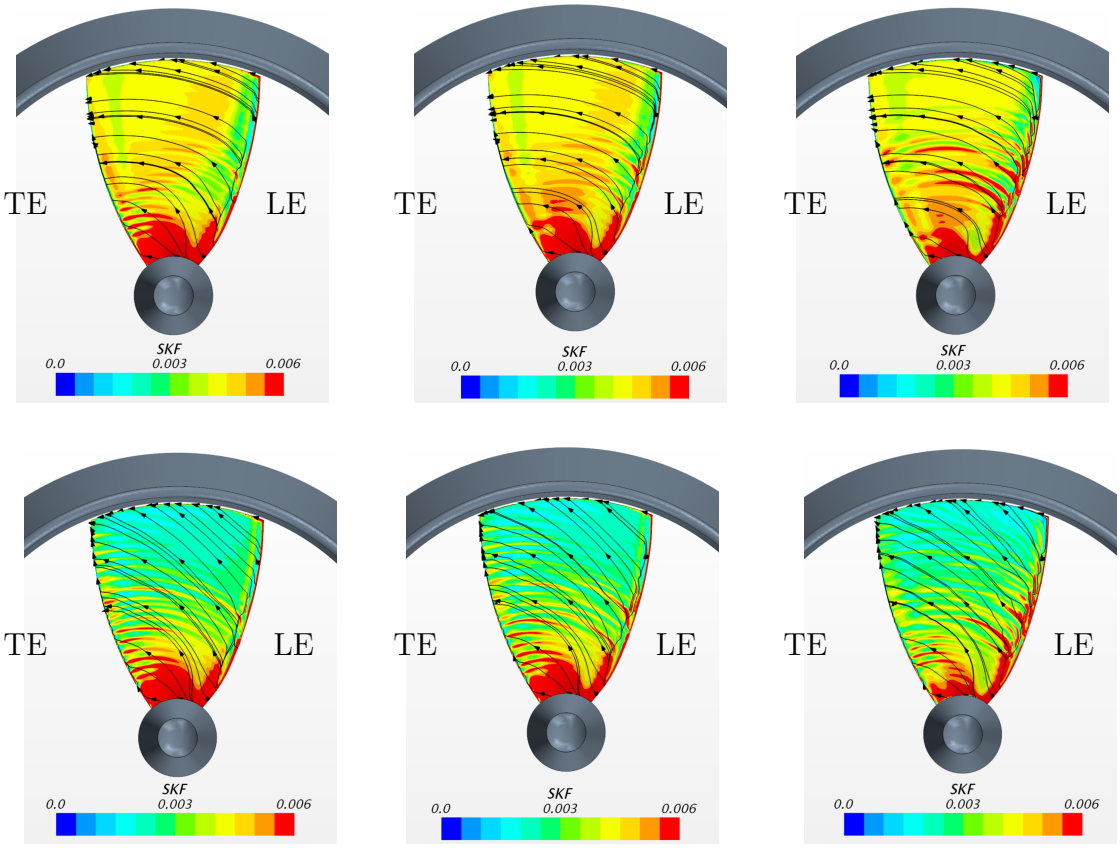

(a) J=0.1 (b) J=0.3 (c) J=0.5

Figure 4.13: Constrained streamline pattern with skin friction coefficient contour on the pressure side of the propeller's surface for different loading conditions, Top: Turbulent Model; Bottom: Transition Model

4.2.4 Flow Field around the Duct

The relative contribution to total thrust from the duct increases with an increase in propeller loading. As the propeller loading changes the flow field around the duct also changes. Fig. 4.15 shows the line integral convolution streamline of the velocity field around the duct at different advance coefficients.

It can be clearly seen that the stagnation point position changes with the change in propeller

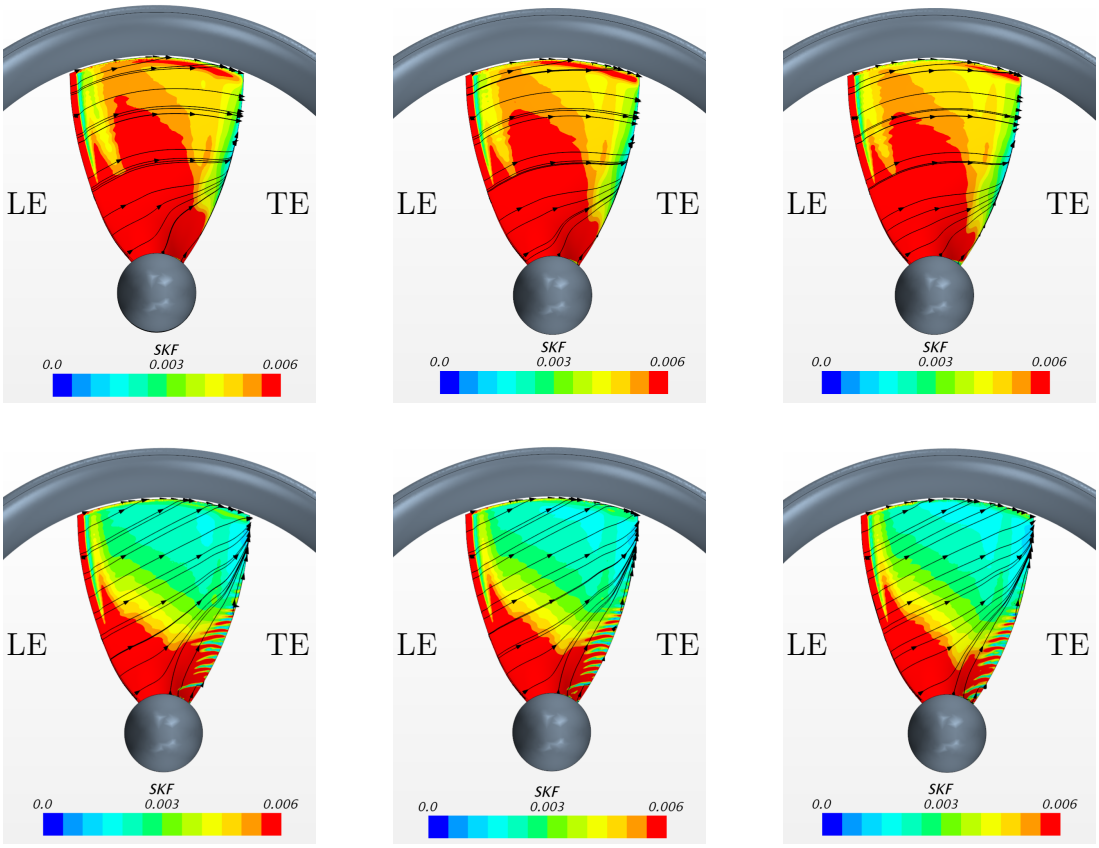

(a) J=0.1 (b) J=0.3 (c) J=0.5

Figure 4.14: Constrained streamline pattern with skin friction coefficient contour on the suction side of the propeller's surface for different loading conditions, Top: Turbulent Model; Bottom: Transition Model

loading. At advance coefficient $J = 0.1$, the stagnation point is on the outer surface of the duct and with an increase in the advance coefficient, the stagnation point shifts towards the leading edge of the duct. At advance coefficient $J = 0.4$, the flow almost approaches along the camber line of the duct. The stagnation point then shifts slightly towards the inner surface of the duct for higher advance coefficients of $J = 0.5$ and 0.6.

The flow starts separating at the leading edge of the duct and the separation bubble is predicted with the consequent transition at the reattachment point for advance coefficient $J = 0.5$. Bhattacharyya et al. [9] also found the separation bubble near the leading edge

on the outer surface of the duct 19A with controllable pitch propeller inside the duct at advance coefficient $J = 0.6$. The reattachment point moves aft as the advance coefficient increases until the flow fully separates at $J = 0.6$. This shows that the propeller loading and type of propeller can have an effect on the flow separation on the outer surface of the duct. This confirms that the duct 19A is not suitable for low loading conditions (high advance ratios) for low Reynolds number propeller also. Since the duct has a blunt trailing edge, an unsteady separation with a pair of counter-rotating vortices is formed due to boundary layer separation from inner and outer surface of the duct.

4.2.5 Tip Gap Flow Analysis

The characteristic strong tip vortex flow which establishes on the open propeller, due to the pressure difference between face and back, is substantially prevented by the presence of the duct. This flow in the tip gap is also influenced by the boundary layer on the inner side of the duct and the propeller tip, and the centrifugal force. Bhattacharyya et al. [9] showed that the separation on the inner side of the duct gets influenced by the tip vortex forming at the propeller tip of the skewed propeller and it can modify the wake flow field and duct thrust. The propeller $K_a - 4 - 70$ has a wide tip and hence accurate resolution of tip vortex is essential for improved prediction of duct and propeller thrust.

Fig. 5.4 shows the flow field on five sections across the tip of the propeller. It can be seen that the tip vortex is formed and the flow gets attached to the suction side of the propeller blade. The size of the tip vortex formed increases from leading edge to the trailing edge at particular advance coefficient. With the change in the size of tip vortex, the attachment point on the suction side also changes.

The size of the tip vortex at a particular section also changes with the change in advance

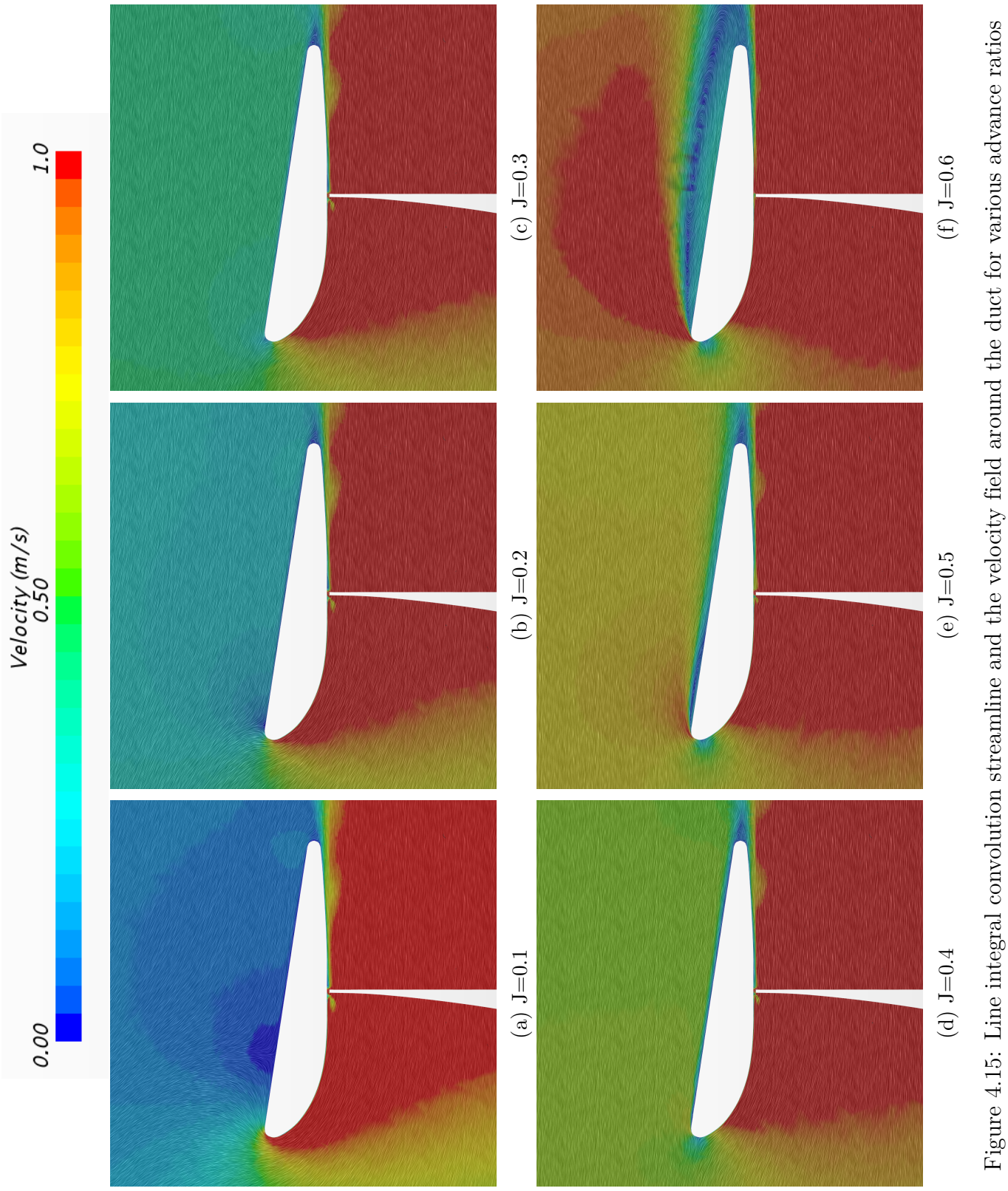

(a) J=0.1 (b) J=0.2 (c) J=0.3

(d) J=0.4 (e) J=0.5 (f) J=0.6

Figure 4.15: Line integral convolution streamline and the velocity field around the duct for various advance ratios

coefficient. At higher loading condition (lower advance coefficient), the pressure difference between the pressure and suction side is higher and hence the size of the tip vortex is larger. With an increase in the advance coefficient, the tip vortex size gets smaller. At higher advance coefficient, the tip vortex is not formed immediately after the leading edge. Fig. 4.16e and 4.16f shows that there is no backflow across the section 1 and 2 for advance coefficient $J = 0.5$ and $J = 0.6$.

4.2.6 MRF and Sliding Mesh for Propeller

In this section, we discuss the unsteady sliding mesh approach for modeling flow around the propeller. The analysis is done at advance coefficient $J = 0.5$ and results are compared with steady-state MRF approach. In the sliding mesh approach, the region containing the propeller rotates by fixed angular rotation per time step. For each time step, the interfaced region slides the mesh to the new position according to the user-defined motion. The time step used in unsteady simulation corresponds to rotation of 0.5 deg for the propeller. This time step ensures that the average convective courant number is as around 0.03 on the surface of the propeller with maximum convective courant number around 10 for few cells in prism layer near leading edge of the tip region. Table 4.5 gives the hydrodynamic coefficient calculated using both MRF and sliding mesh approach. The hydrodynamic coefficient predicted using MRF approach are in better agreement with the experimental results than the sliding mesh approach.

Hydrodynamic Coefficient	**MRF**	**Sliding Mesh**	**Experimental**
K_{TP}	0.1164	0.1176	0.1094
K_{TN}	0.0148	0.0176	0.0072
K_T	0.1312	0.1352	0.1166
$10K_Q$	0.1916	0.1963	0.1864

Table 4.5: Hydrodynamic coefficient for MRF and sliding mesh approach for ducted propeller at $J = 0.5$

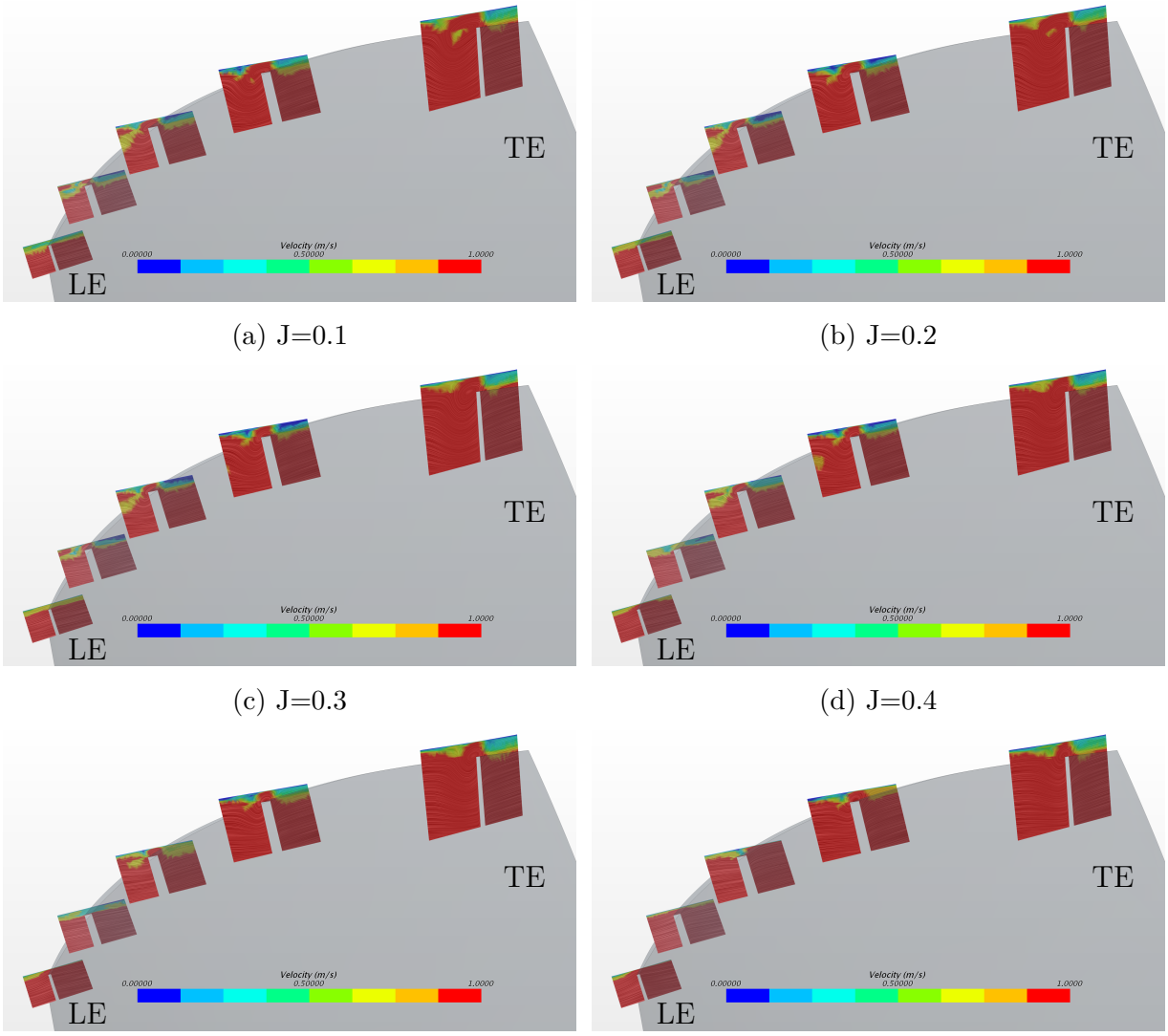

(a) J=0.1 (b) J=0.2

(c) J=0.3 (d) J=0.4

(e) J=0.5 (f) J=0.6

Figure 4.16: Velocity flow field in the tip gap with line integral convolution streamline at different advance ratios

In order to find the cause of the discrepancy between MRF and sliding mesh results, the flow field around the duct and tip leakage flow are compared for both approaches. Fig. 4.17 shows the flow field around the duct for two approaches. It can be seen that the MRF approach predicts a single separation bubble near the leading edge and on the outer surface of the duct. On the other hand, the sliding mesh approach predicts a separation bubbles

smaller in size than predicted by MRF approach, in the same region. Also trailing edge vortex predicted using the sliding mesh approach is smaller than the one predicted by MRF approach.

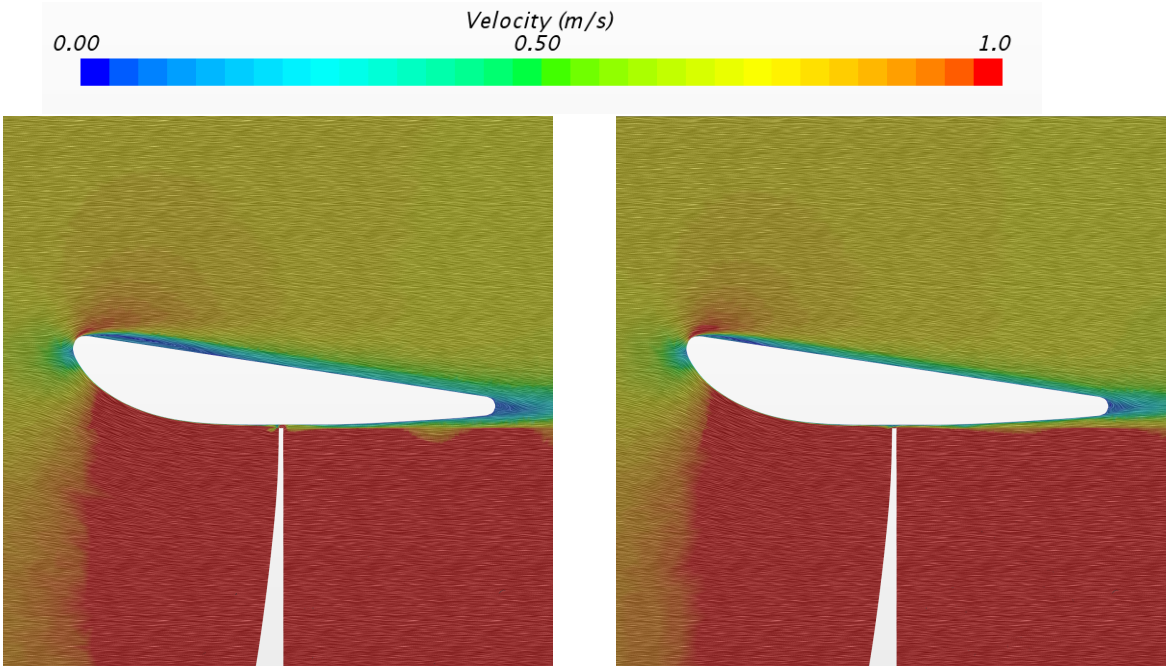

(a) MRF (b) Sliding Mesh

Figure 4.17: Comparison of flow analysis around the duct at J=0.5 for MRF and sliding mesh approach

Fig. 4.18 shows the tip leakage flow predicted using MRF and sliding mesh approach at advance coefficient $J = 0.5$. The magnitude of velocity between the propeller tip and the duct inner surface is considerably different for both approaches. The velocity magnitude in the gap is lower in case of sliding mesh approach than the MRF approach. Hence the leakage flow from the pressure side to suction side is smaller for the sliding mesh approach and the total thrust predicted is higher as compared to the MRF approach. The difference in forces predicted by two approaches might be due to unsteady simulation and difference in the interpolation of flow quantities for sliding interface in case of sliding mesh approach. The velocity is exactly matched at the interface in case of MRF approach via the velocity

transformation from one reference frame to another. Due to the lack of physical data it is difficult to say which approach is better and accurately predicts the flow around the ducted propeller.

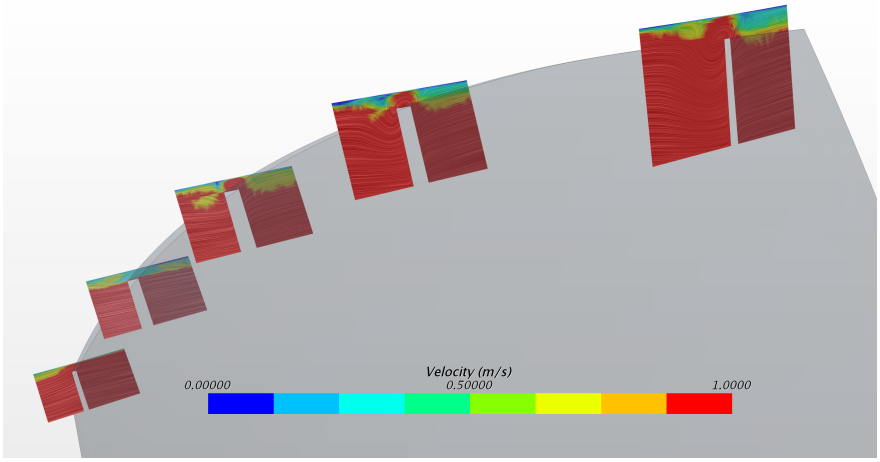

(a) MRF

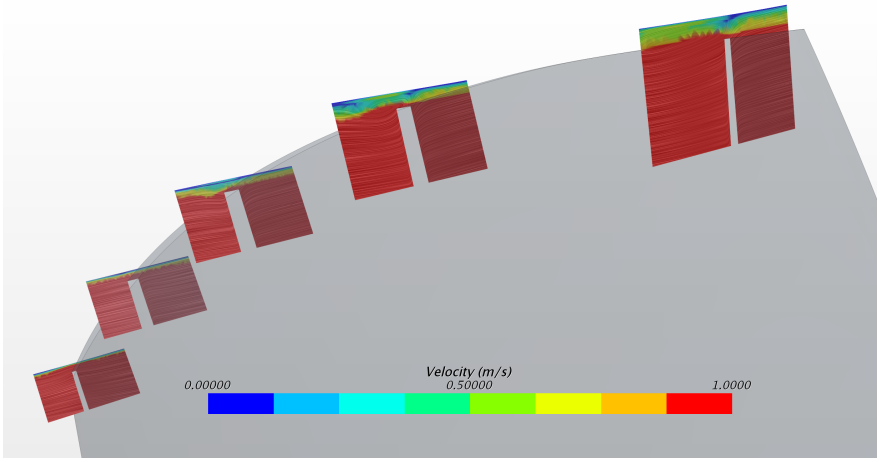

(b) Sliding Mesh

Figure 4.18: Comparison of tip leakage flow at $J = 0.5$ for MRF and sliding mesh approach

4.3 Propeller Redesign

The simulation-based design of the propeller is based on an automatic computational framework whose main components are parametric geometry definition of propeller, high-fidelty RANSE solver for the prediction of propeller's hydrodynamic performance and multi-objective optimization algorithm. The design optimization is applied to a propeller K_a-4-70 inside an accelerating nozzle 22 [50]. The accelerating nozzle has $L/D = 0.8$. The longer duct is used so that the stator can be accommodated behind the propeller. The CFD model discussed in section 4.1 is used for open-water performance comparison with experimental results. Fig. 4.19 shows that the hydrodynamic coefficients predicted using CFD model are in good agreement with the experimental results.

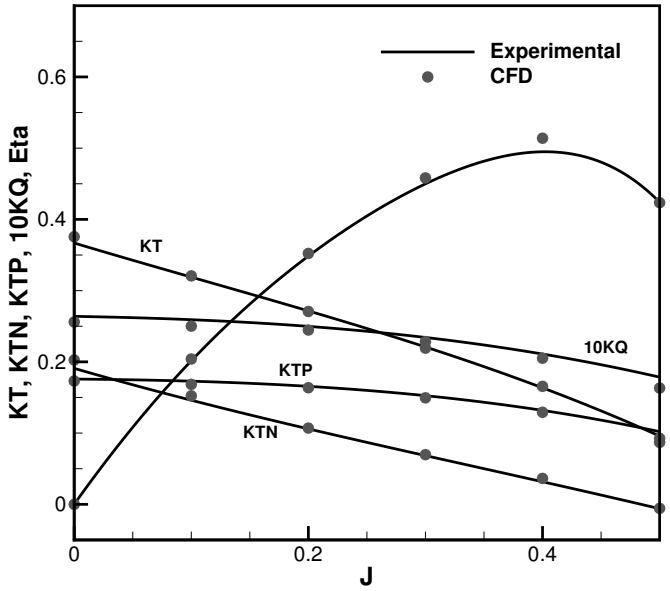

Figure 4.19: Open-water performance comparison of propeller K_a-4-70 with $P/D = 0.8$ inside the nozzle no. 22 with experimental results

4.3.1 Parametric Geometry for the Propeller

The geometry of the propeller is inherently parametric in which radial distribution of different parameters are given in the form of table. The radial distribution of design parameters- pitch, maximum camber, maximum thickness and chord length can be fitted using b-spline curve. The third order b-spline curve for all parameters are constructed using four control points. The radial distribution of parameters created by this method is verified to confirm the reproducibility of original parameters and it shows good agreement with original parameters of the propeller K_a-4-70. This method is similar to the method used by other researchers for parametric optimization of open and ducted propeller [14]. The control points for these b-spline curves are used as the design variables for an optimization algorithm. The control points can be changed in a systematic manner within the user-defined range as discussed later on in section 6.1.1 and different propeller geometries can be generated. In this design space, the optimization algorithm will look for the best design that satisfies a series of objective function. Fig. 4.20 shows the radial distribution of various propeller design parameters like maximum camber, maximum camber position, pitch, maximum thickness and chord length non-dimensionalized with the diameter of the propeller. The maximum thickness of the base propeller K_a-4-70 is increased by 50% more due to manufacturing constraint.

4.3.2 Hydrofoil Section

To complement the parametric geometry created in section 4.3.1, the hydrofoil shape must be specified. There are different hydrofoil shapes available for the propeller. Each of these hydrofoil shapes are suitable for specific applications. Brockett [15] studied three types of hydrofoil section and found that hydrofoil having NACA 66 (modified) thickness distribution with NACA a=0.8 camber line has favorable cavitation characteristics for wider range of

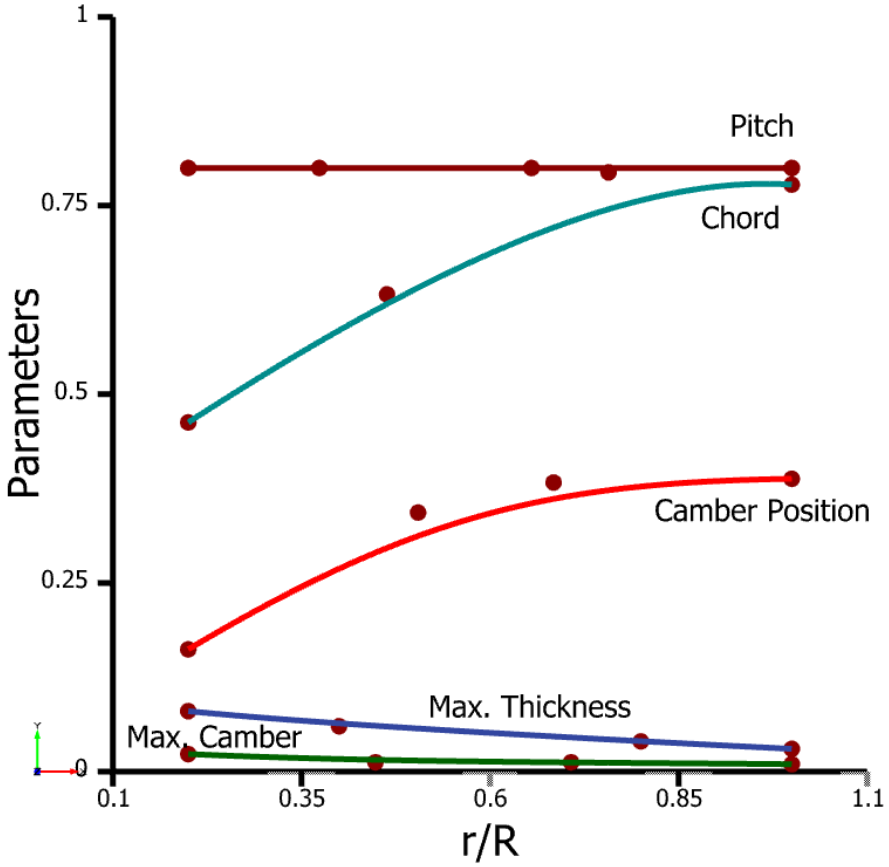

Figure 4.20: Parametric geometry definition for the base propeller K_a-4-70

angle of attacks. The NACA 66 (modified) section was obtained by thickening the trailing edge of original NACA 66 section for ease of manufacturing. Also a sharp suction peak was present near the leading edge of original NACA 66 section. This hump of suction was faired by trial and error to give smooth pressure curve in NACA 66 (modified) section.

In this study hydrofoil shape with NACA a=0.8 camber line and NACA 66 (modified) thickness is used. The hydrofoil sections are generated by superimposing thickness distribution perpendicularly on the camber line. The thickness and camber ordinates were interpolated at locations where the data is not available. Fig. 4.21 shows hydrofoil shapes at four radial location with design parameters (chord length, maximum camber, maximum thickness) same

as in Fig. 4.20. The details of NACA a=0.8 camber line and NACA 66(mod) thickness are given in Appendix C.

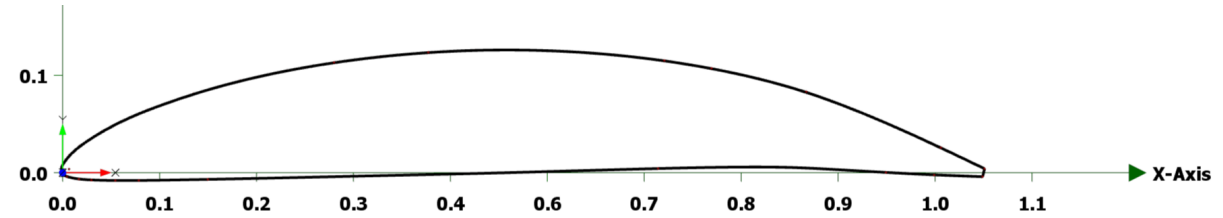

(a) $r/R = 0.3$

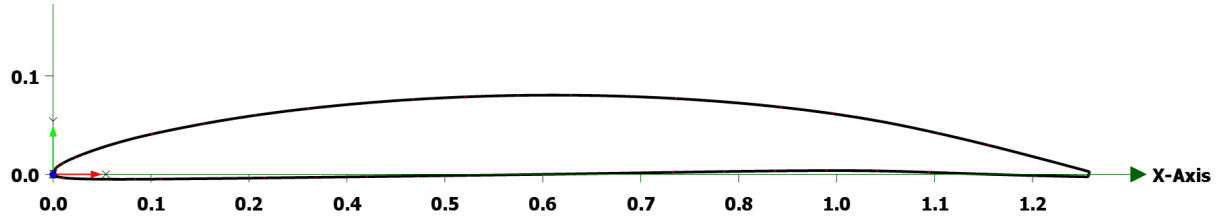

(b) $r/R = 0.5$

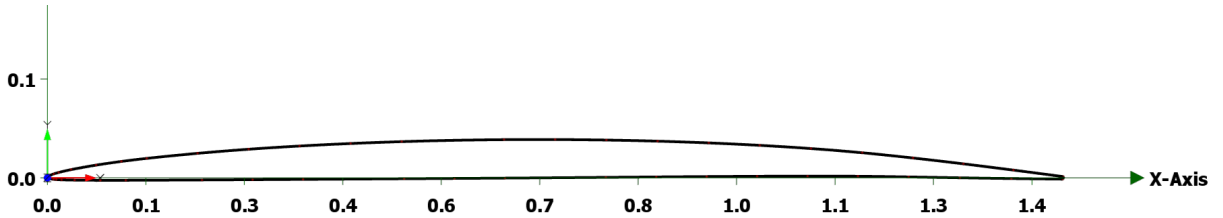

(c) $r/R = 0.7$

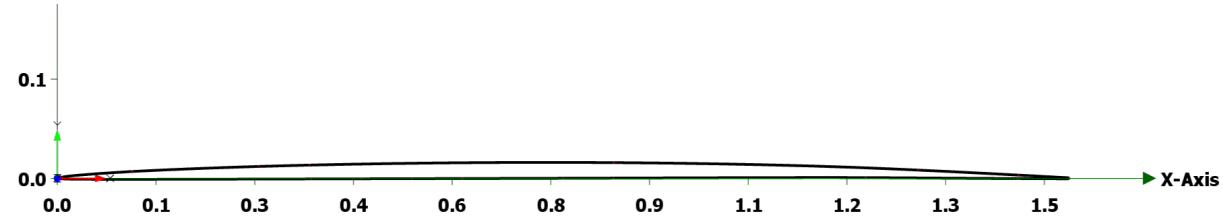

(d) $r/R = 0.9$

Figure 4.21: Hydrofoil sections generated using NACA a=0.8 camber line and NACA 66 (modified) thickness distribution at four radial locations for the base propeller K_a-4-70

Chapter 5

Postswirl Stator Design

The power required by an AUV towing a large payload is considerably higher than non-towing AUV. Even if the propeller is rotating at a very high speed which is limited due to the risk of cavitation, the torque of the propeller is still very high. The propeller induces this torque to the AUV and will cause an excessive rolling. In order to bring directional stability to the AUV, post-swirl stator is used as discussed in section 2.4.

The flow around these propulsors is usually analyzed using potential based panel method [29]. A coupled lifting surface/ RANS method has been used for designing this propulsor by other researchers [10, 17, 63]. Pumpjet propulsors with good cavitation resistance has been designed using streamline curvature method [27, 43]. The lifting surface method, the panel method and streamline curvature method are computationally fast and are mature methods. However, these methods can not predict the complex flow field such as leading edge flow separation, and tip leakage flow between the propeller tip and the duct. Also, there is a strong interaction between the propeller and the stator. Hence the Navier-Stokes equation solver is used in this study for designing the propulsor.

The main objective of the postswirl stator is to eliminate the propeller torque. This can be achieved by removing the swirl component of flow present at the propeller's wake. When the swirl in the wake of the propeller is removed the rotational energy losses is also reduced and overall efficiency might improve.

5.1 Axial Compressor Design Method

The postswirl stator is designed using an axial compressor design method. The shape of the stator is like a hydrofoil and is closely related to the wake characteristics of the propeller. The flow exiting from the propeller has three components of velocity in axial, tangential and radial direction. For the present study, it is assumed that the radial component of velocity is very small and is neglected. From CFD RANSE simulations, we can get the axial and tangential component of velocity at various radial locations from hub to tip behind the propeller. The stator should be designed in such a way that the flow leaving the stator has a negligible tangential component of velocity.

Based on the axial and tangential component of velocity leaving the propeller an inlet angle of the stator blades can be calculated. The exit angle of the stator should be zero so that the tangential component of velocity is minimized. Using an inlet and an exit angle the camber line of the stator blade is constructed. The hydrofoil section is generated by superimposing the NACA 00XX thickness distribution on the calculated camber line. Fig. 5.1 shows the velocity triangle at the propeller exit and the stator exit. The propeller is rotating and the tangential velocity U at a particular radial location will be $r\Omega$ where Ω is the rotational speed of the propeller. The fluid leaves the propeller with relative velocity W_1. Since the stator is not rotating, it sees the flow coming at an absolute velocity V_1. The stator is designed such that the flow leaves the propulsor in the axial direction with velocity V_2.

5.2 Self-propulsion Point of the Propulsor

The hydrodynamic forces and moment of the propeller get modified when it operates behind the hull. In order to find the self-propulsion point, Myring hull [49] is used in this study for

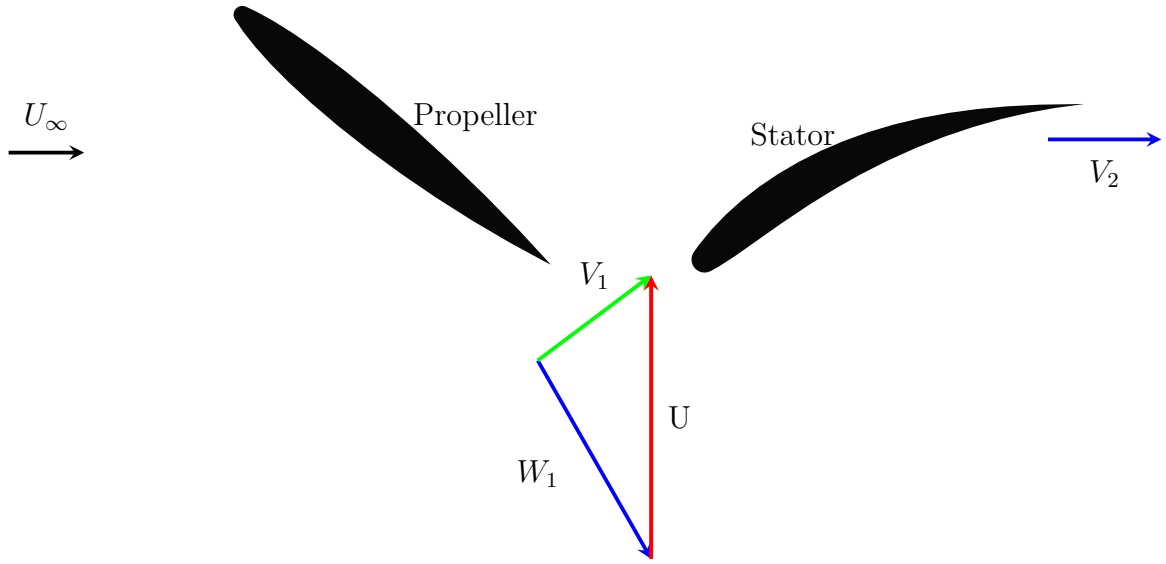

Figure 5.1: Sketch of the velocity triangles at propeller and stator exit

all CFD simulations. The design payload drag in this study is 70 N. The speed of the AUV at design condition is 2 m/s. At self-propulsion point, the total thrust of the propeller and the duct is equal to the sum of drag of the hull and the payload. The self-propulsion point is obtained by calculating total thrust at two speeds for the propeller and then interpolating the hull drag and total thrust to get self-propulsion point. The speed of the propeller is 57 *rps* at self-propulsion point. The performance of propeller behind AUV at two speeds and self-propulsion point is given in table 5.1. The payload drag is assumed to remain constant for all rotational speeds of the propeller.

Speed (rps)	**Total Thrust (N)**	**Propeller Torque (N-m)**	**Hull Drag (N)**	**Total Drag (N)**
50	58.14	0.60	11.89	81.89
65	118.78	1.09	21.69	91.69
57	86.45	0.83	16.47	86.47

Table 5.1: Self-propulsion point calculation

The effective wake fraction and the relative rotational efficiency are calculated using thrust identity principle. First, the total thrust coefficient and torque coefficient for the propeller is calculated at self-propulsion point. The advance coefficient corresponding to the total thrust coefficient is determined from open-water performance calculated in Section 4.3. From this, we can calculate the open-water advance speed. The effective wake fraction is calculated to be $w = 0.367$ using open-water advance speed and the speed of the AUV. The torque coefficient is extracted from the open-water performance at the same advance coefficient. The relative rotational efficiency is calculated to be 1.03 from open-water torque coefficient and self-propulsion point torque coefficient. The thrust deduction factor is calculated using bare hull drag and drag of the hull in the presence of propeller operating at self-propulsion point. The thrust deduction factor is calculated to be $t = 0.162$.

5.3 Stator Design

In this section, the design procedure and hydrodynamic analysis for the stator is presented. Also, the results are presented for the first design of the stator which is used as a baseline for future design and performance comparison.

5.3.1 Turning Angle for the Stator

As discussed in Section 5.1, the turning angle of the stator can be calculated using axial and tangential component of velocity in the wake of the propeller. Fig. 5.2 shows the axial and tangential velocity contour downstream to the propeller at a distance $x/D = 0.1$ from the propeller plane. The axial and tangential velocities are normalized with the the free-stream velocity $V = 2\ m/s$ and the propeller is rotating at $n = 57\ rps$.

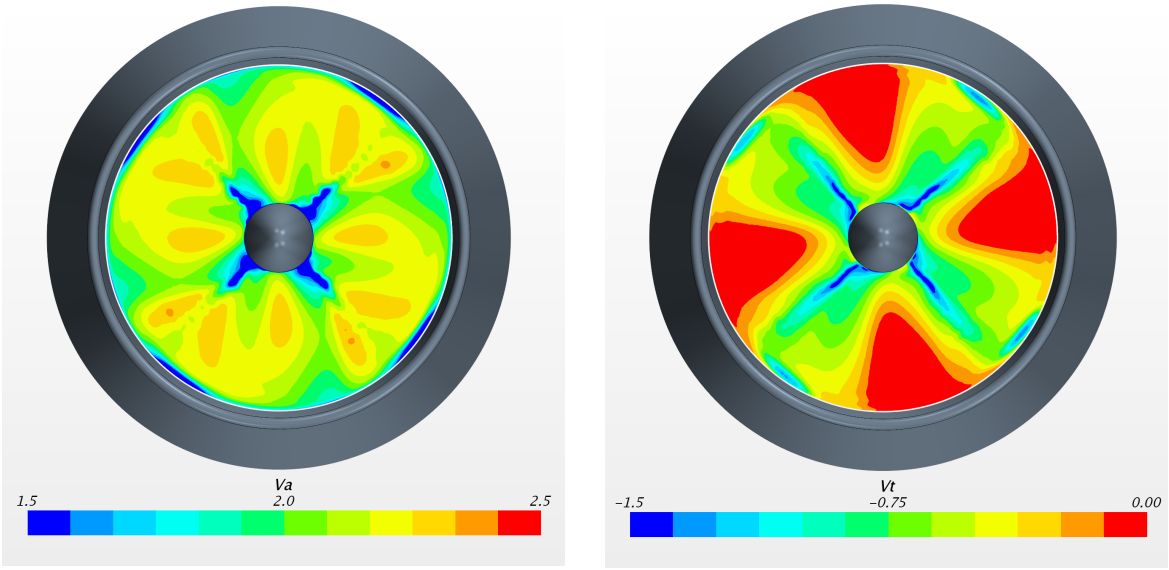

(a) Axial Velocity (b) Tangential Velocity

Figure 5.2: Normalized axial and tangential velocity distribution in the wake of the propeller at $x/D = 0.1$ from the propeller plane for $V = 2.0\ m/s$ and $n = 57\ rps$

Fig. 5.3 shows the circumferential variation of normalized axial and tangential velocity at different radial locations. The magnitude of axial velocity is smallest at the tip due to the tip leakage vortex. The tip leakage vortex is shown in Fig. 5.4 at three angular position for one blade. The tip leakage vortex is formed due to the pressure difference between back and face side of the propeller. The axial velocity is nearly constant at $r/R = 0.6$ and 0.8. The tangential velocity magnitude is smaller near the root region of the propeller as compared to higher radial location. The turning angle is calculated based on the axial and tangential component of velocity in the wake of the propeller. The turning angle is given as

$$\theta = tan^{-1}\left(\frac{V_T}{V_A}\right) \tag{5.1}$$

Fig. 5.3c shows the turning angle at different radial locations. The turning angle is maximum for the region near the root of the propeller. This is due to a smaller axial velocity of flow

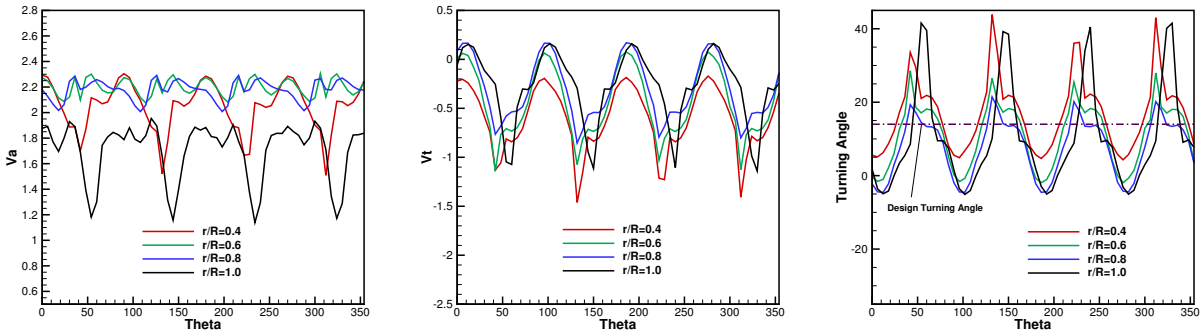

(a) Axial Velocity (b) Tangential Velocity (c) Turning Angle

Figure 5.3: Circumferential variation of normalized axial velocity, tangential velocity and turning angle of the flow in the wake of the propeller at $x/D = 0.1$ from the propeller plane at different radial location for $V = 2.0\ m/s$ and $n = 57\ rps$

near the hub of the propeller. At the tip of the propeller, there is a maximum circumferential variation in turning angle.

For the first design of the stator, a simplified steady-state approach, as described in section 3.4.1 is used for modeling the propeller's unsteady hydrodynamics. Hence, CFD simulations give velocity only at a particular instant for a particular position of the propeller. In actual operation, the propeller is rotating and the velocity seen by the stator is continuously changing. Hence, from the design perspective, one has to find the average effective turning angle of the stator that will remove the swirl present in the flow to the maximum extent. Also, the turning angle should vary radially from the hub to the tip to straighten the flow in the wake of the propeller. For this preliminary study, though, we assumed no twist for the stator. i.e a constant pitch angle from root to the tip is used for the stator. For the first design of postswirl stator, the constant turning angle of 14° is used. The constant turning angle is obtained by taking a circumferential average of turning angle at $r/R = 0.7$. The comparison of steady state approach with an unsteady approach is further investigated in section 5.3.4.

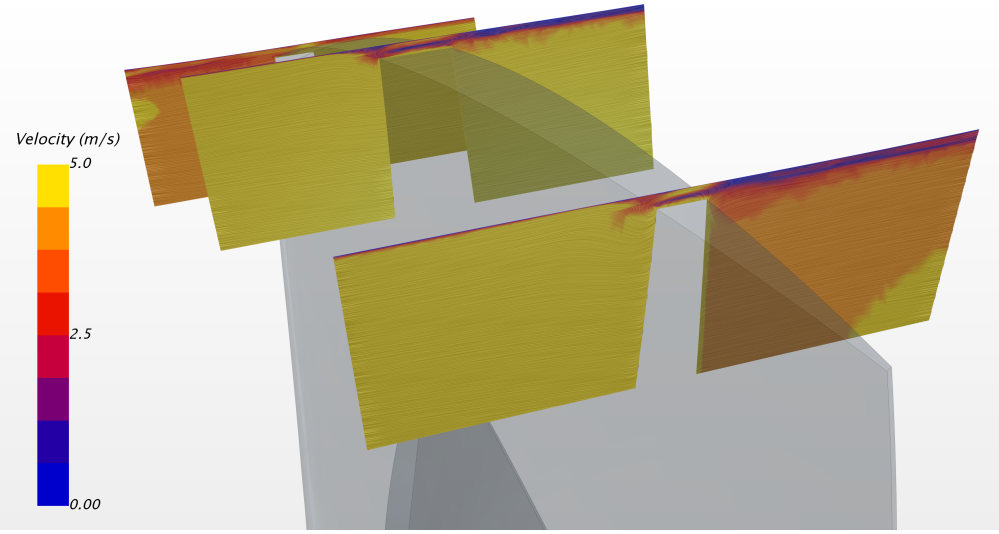

Figure 5.4: Tip leakage vortex between the propeller and inner side of the duct for $V = 2$ m/s and $n = 57$ rps

5.3.2 Effect of Thickness

The camber for the stator is calculated using the required turning angle of the flow from the wake of the propeller calculated in section 5.3.1. The exit angle of the flow from the stator should be zero. Using these two angles, the camber line is generated for the stator using a third order b-spline curve and three control points. The first and second point is selected to give the required turning angle. The third point is selected based on the projected chord length of the stator and the coordinates of the second point. This is summarized in equation 5.2. The stator blade shape is generated by superimposing NACA 00XX thickness distribution on the calculated camber line.

$$\begin{aligned} P_{2X} &= P_{1X} + \alpha \cdot L \cdot tan\theta; \quad P_{2Y} = P_{1Y} + \alpha \cdot L \\ P_{3X} &= P_{2X}; \quad P_{3Y} = P_{1Y} + L \end{aligned} \tag{5.2}$$

where L is the projected chord length, θ is the turning angle, P_1, P_2 and P_3 are control points for camber line. Fig. 5.5a shows the camber line generated using equation 5.2 for the stator.

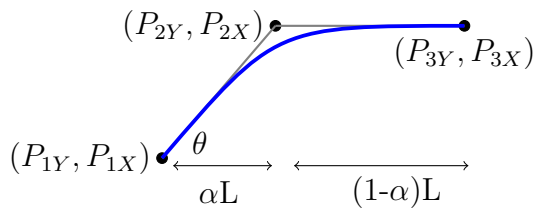

(a) Camber line for the stator

(b) NACA 0010 Section

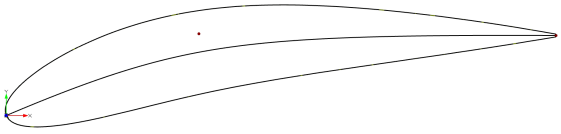

(c) NACA 0015 Section

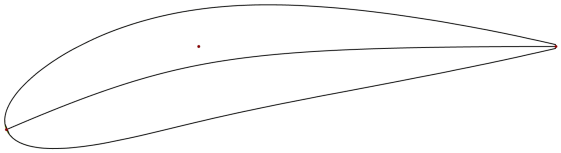

(d) NACA 0020 Section

Figure 5.5: Parametric geometry definition for the stator camber and different hydrofoil section for the stator

In the present study, NACA 0010, NACA 0015 and NACA 0020 thickness distribution is used to study the influence of stator blade thickness on propulsor's performance. Fig. 5.5b-5.5d shows hydrofoil section for the same camber and different thickness distribution.

The performance of the propulsor is calculated at self-propulsion point ($n = 57\ rps$ and $V = 2\ m/s$). For all simulations, nine stator blades are used to generate sufficient torque to counteract the rolling torque of the propeller. The camber of the stator is kept constant from hub to the tip for the first geometry of the postswirl stator. If the stator is correctly designed then it can also generate the thrust in a positive direction. Otherwise, the postswirl stator will increase the total drag. Once the stator is added, the performance of the propeller also gets changed due to its interaction with the stator. Table 5.2 gives the results for different parameters for different thickness distribution for the stator. The residual torque is minimum for NACA 0015 thickness distribution. The force acting on the stator with NACA 0020 thickness is in opposite direction of the thrust of the propeller. Hence the drag of the whole system increases if NACA 0020 thickness distribution is used for the stator blade. The efficiency is calculated based on the total thrust from propeller, duct and stator and torque

of the propeller.

Fig. 5.6 shows the pressure coefficient on the surface of the stator for constant turning angle from root to the tip and NACA 0015 as the stator's thickness distribution. The pressure coefficient is calculated using an effective velocity at each radial location. The flow separation is observed on the face side of the stator. The flow separation is due to the high angle of attack of flow on the stator.

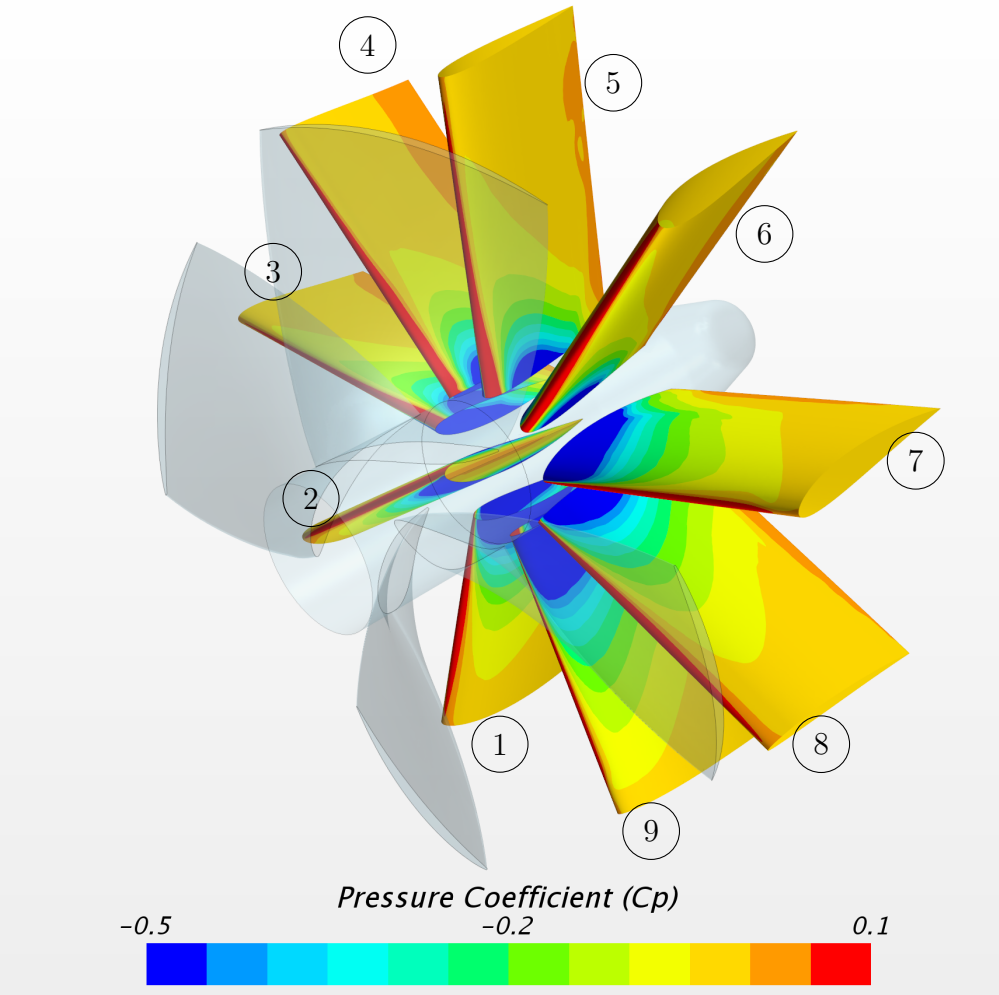

Figure 5.6: Pressure Coefficient on the surface of stator blades for $V = 2m/s$ and $n = 57rps$

NACA Thickness	T_{Total} (N)	$T_{Prop.}$ (N)	T_{Duct} (N)	T_{Stator} (N)	$Q_{Prop.}$ (N-m)	Q_{Stator} (N-m)	$Q_{Res.}$ (N-m)	D_{Hull} (N)	η_P (%)
0010	89.85	57.32	30.96	1.56	0.869	-0.667	0.202	17.34	57.7
0015	91.02	60.82	29.66	0.55	0.906	-0.755	0.151	16.98	56.1
0020	91.27	66.20	27.57	-2.51	0.961	-0.791	0.170	16.36	53.0

Table 5.2: Effect of stator's thickness on propulsor's performance at $V = 2.0\ m/s$ and $n = 57$ *rps*

5.3.3 Wake Flow Characteristics

In this section, we discuss the wake characteristics of the flow downstream to the propeller and the stator. The main purpose of the stator is to remove the swirl in wake of the propeller and recover rotational kinetic energy loss. In order to see the effectiveness of stator design, the axial and tangential components of velocity are plotted in transverse section $0.1D$ downstream from the propeller and the stator. Fig. 5.7 shows axial and tangential velocity in these two sections. From fig. 5.7a and 5.7b, we can see that the axial velocity is increased from the exit plane of the propeller to the exit plane of the stator. The transverse section aft of the stator is outside the nozzle and there is a backflow from the inner surface of the duct to the outer surface of the duct. This is indicated by backflow (negative velocity contour) in fig. 5.7b.

The tangential velocity contour for same transverse sections is shown in fig. 5.7c and 5.7d. The surface average of tangential velocity reduces from 0.85 m/s to 0.15 m/s. The reduction in tangential velocity shows that the stator is able to remove the swirl component of velocity leaving from the propeller. This can be seen in fig. 5.8, which shows the velocity vectors with axial velocity contour on three different cylindrical section at different radii. By removing the swirl in the wake of the propeller, the stator is able to generate the counteracting moment

to reduce the rolling of an AUV.

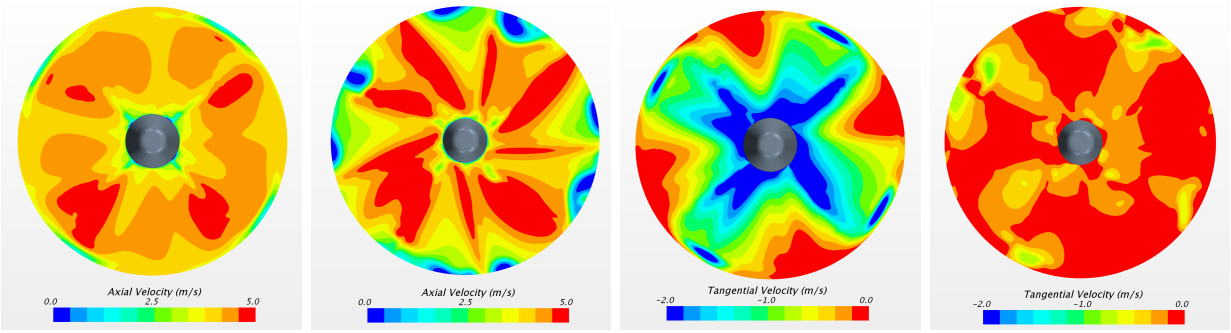

(a) Post Propeller (b) Post Stator (c) Post Propeler (d) Post Stator

Figure 5.7: Axial and tangential component of velocity in the wake of the propeller and the stator at $V = 2.0\ m/s$ and $n = 57\ rps$

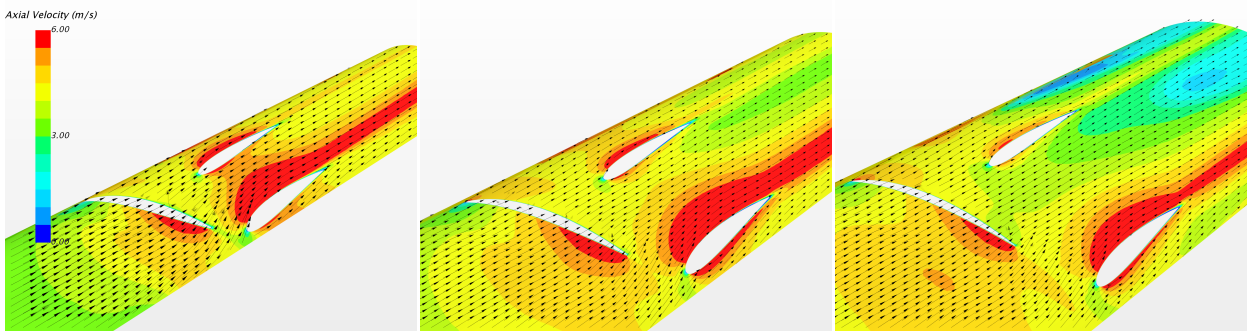

(a) $r/R = 0.5$ (b) $r/R = 0.7$ (c) $r/R = 0.9$

Figure 5.8: Velocity vector with axial velocity contour on three cylindrical section at different radii for $V = 2.0\ m/s$ and $n = 57\ rps$

5.3.4 Sliding Mesh vs Moving Reference Frame Approach

In previous sections, a simplified steady state approach as described in section 3.4.1 is used for modeling the propeller's unsteady hydrodynamic forces. Hence, CFD simulations give velocity only at a particular instant for a particular position of the propeller. In actual operation, the propeller is rotating and the velocity seen by the stator is continuously changing.

Hence, from the design perspective, one has to find the average turning angle that will remove the swirl in the flow to a maximum extent throughout the rotation of the propeller. However, running the unsteady simulation is computationally intensive and time-consuming.

In this section, we calculate the unsteady forces acting on the stator for one revolution of the propeller using an unsteady sliding mesh approach as described in section 3.4.2. The time step used for this calculation corresponds to 1° angular movement per time step. This time step ensures that the maximum Courant number is less than 10 except for few bad cells in the leading edge and trailing edge region due to the chopping of prism layers around sharp curves. This time step is found to be a good compromise between computational efficiency and numerical stability. Fig. 5.9 shows the velocity vectors and pressure coefficient contour for the stator blades at three radial locations and for four angular positions of the propeller as it is turning. The pressure field around the stator changes as the propeller is rotating which in turn changes the lift force acting on each of the stator blades.

Fig. 5.10a and 5.10b shows the unsteady forces acting on each stator blade for one revolution of the propeller (stator blade numbering is given in Fig. 5.6). It can be seen that the forces acting on each blade changes, as the propeller rotates. However, the total force and the moment of the stator remains constant for one revolution of the propeller. Table 5.3 gives the forces and moments acting on the propulsor for both steady and unsteady approaches. For unsteady sliding mesh approach, the forces are calculated by taking an average over one revolution of the propeller. It can be seen that the force and moments, especially for the propeller, are close to each other for both steady state MRF and unsteady sliding mesh approach. The stator torque predicted by sliding mesh approach is around 12 % less than the MRF approach, which might be due to the flow separation not captured by the steady-state approach. This shows that we can use steady state moving reference approach which is computationally less expensive than the unsteady approach for designing the propulsor.

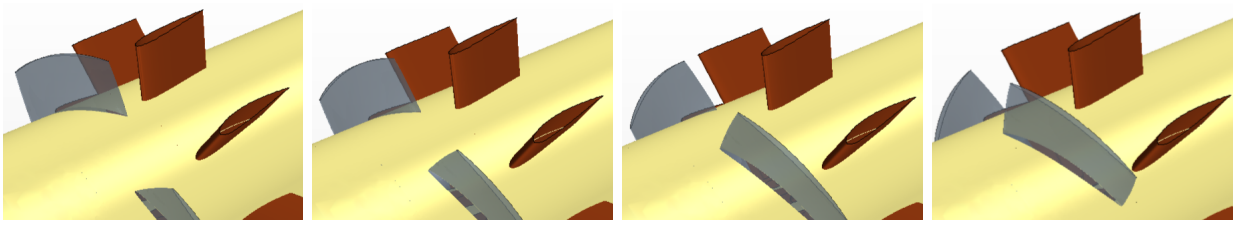

(a) Angular position of the propeller

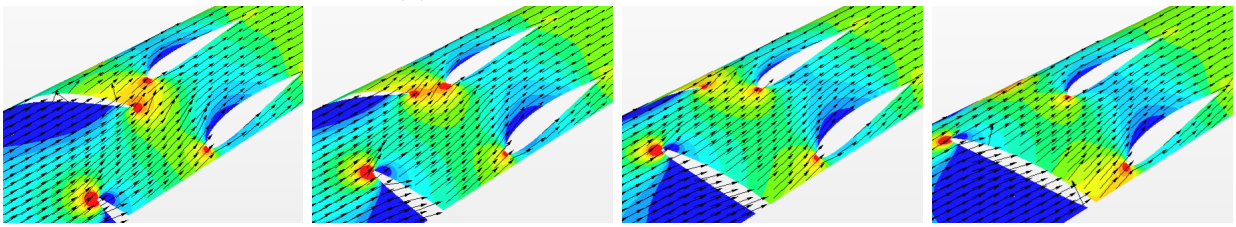

(b) $r/R = 0.5$

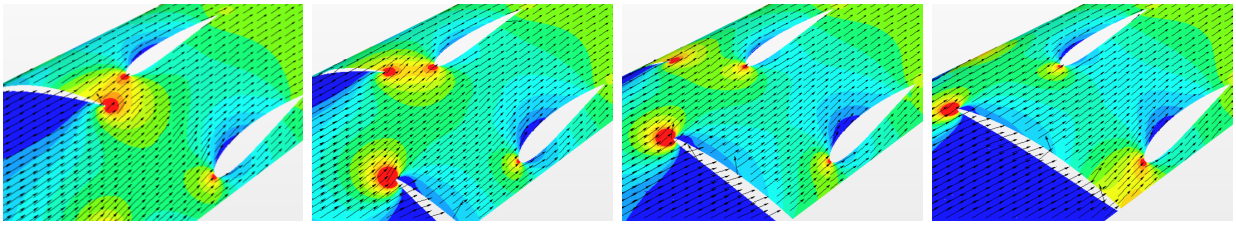

(c) $r/R = 0.7$

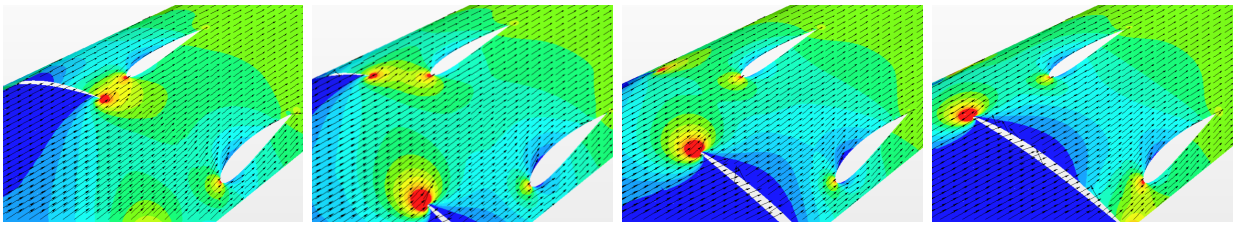

(d) $r/R = 0.9$

Figure 5.9: Velocity vector with pressure coefficient contour for different angular position at different radial location of the propeller during one revolution, $V = 2\ m/s$ and $n = 57\ rps$

Parameters	**MRF**	**Sliding Mesh**	**Percentage Difference**
Propeller Thrust (N)	60.82	57.59	5
Duct Thrust (N)	29.65	30.67	-3
Stator Thrust (N)	0.55	0.85	-55
Propeller Torque (N-m)	0.91	0.88	3
Stator Torque (N-m)	-0.75	-0.66	12

Table 5.3: Comparison of forces and moments calculated using MRF and sliding mesh approach for the propulsor at $V = 2m/s$ and $n = 57\ rps$

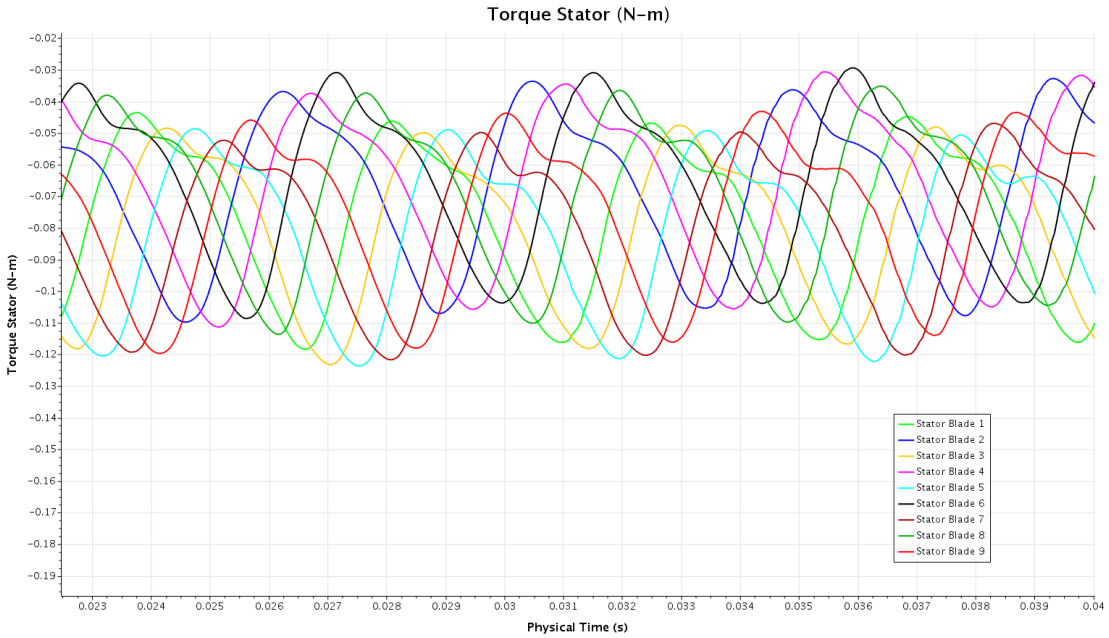

(a) Stator Torque (N-m)

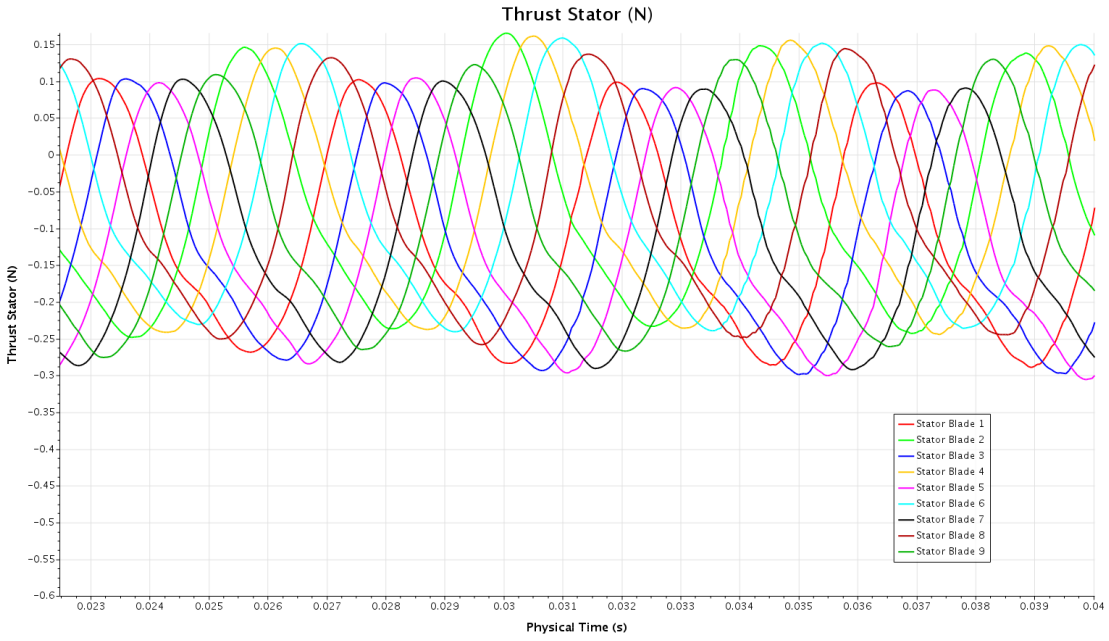

(b) Stator Thrust (N)

Figure 5.10: Unsteady forces and moments acting on the stator during one revolution of the propeller

5.4 Field Trials

The field trials were performed for Virginia Tech Dragon AUV with the base propulsor at the Claytor Lake in Pulaski County, Virginia. The payload was 50 m long and 1 $inch$ diameter thick rope. The propeller was manufactured from Nylon 12CF using Selective Laser Sintering (SLS) process. The duct was manufactured from ABS using Fused Deposition Modeling (FDM). Fig. 5.11 shows Virginia Tech Dragon AUV and the base propulsor used in field trial. The straight-line constant depth mission was given for 60 seconds with the propeller running at 3400 rpm. The commanded depth was 2 m. The velocity of the vehicle was measured using the pressure sensors and Pitot tube connected in the nose of the AUV. The vehicle reached a steady-state velocity of 1.9 m/s as shown in 5.12b. This is 5 % less than the design speed 2 m/s and is a good indication that the propeller can provide the required thrust to tow the payload. The steady-state roll angle was 60° which can be attributed to the fact that the stator is not completely neutralizing the propeller torque. Hence, the propeller torque needs to be completely neutralized to minimize the rolling. The surrogate-based optimization method to design the propulsor with minimum residual torque is described in Chapter 6.

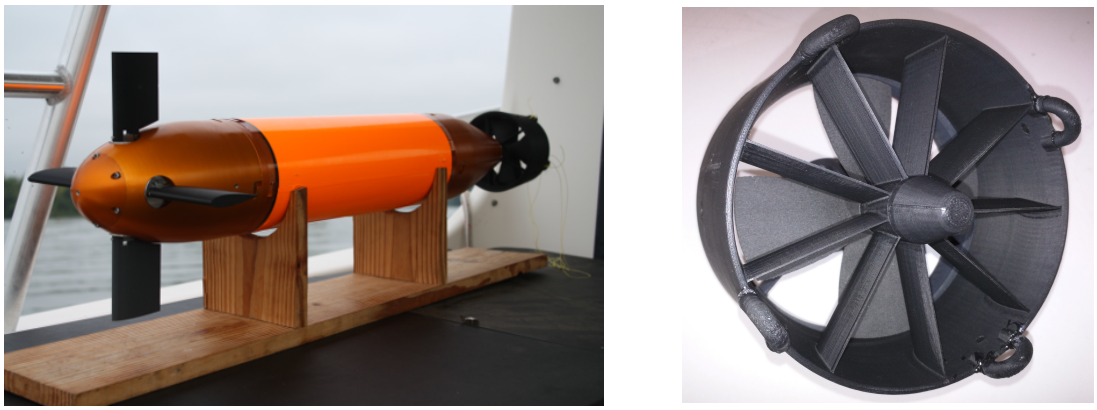

Figure 5.11: Virginia Tech Dragon AUV and base propulsor used in field trials at Claytor Lake in Pulaski County, Virginia

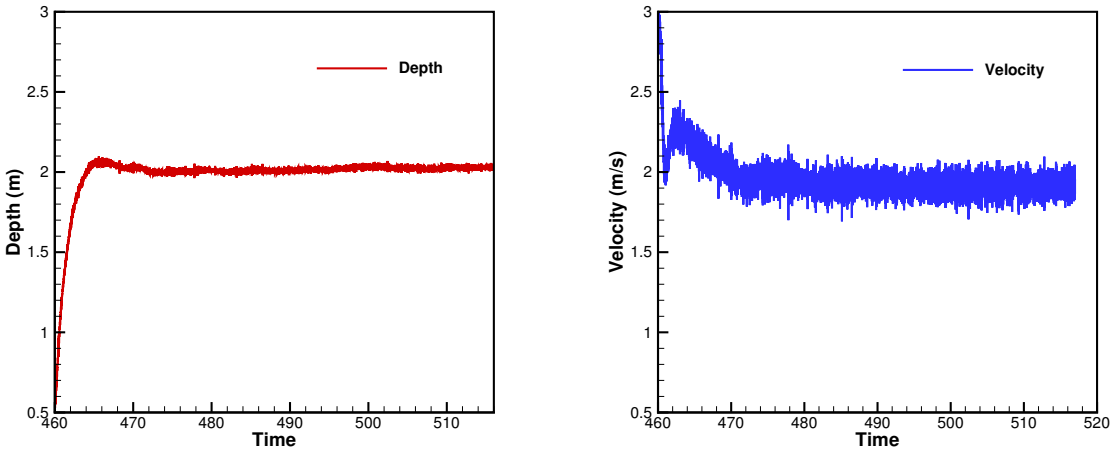

(a) Depth measurement

(b) Velocity measurement

Figure 5.12: Field trial data collected for depth and vehicle speed for Virginia Tech Dragon AUV at Claytor Lake in Pulaski County, Virginia

Chapter 6

Multiobjective Optimization

Design by shape optimization can be a daunting task, especially if the shape is complex and the design approach consists of using high-fidelity numerical simulations. The main elements for a successful shape design by optimization are:

- Efficient and accurate numerical model for simulation of the physics involved
- Fully parametric geometry module for automatic 3D geometry generation
- Global convergence multi-objective optimization algorithm
- Input-output data exchange software interface so that different applications in the optimization loop can communicate

Several researchers have worked on shape optimization for different geometries such as traditional propellers [14, 60], unconventional propellers [24], supercavitating hydrofoils [59] and hull forms [13]. In many of these optimization studies, Genetic Algorithms (GA) were used because of their ease of use, it supports multiobjective and global perspective. For multi-objective optimization problems, there can be a number of possible solutions. For example, in the present study, the objective is to maximize the propulsor efficiency and to minimize the residual torque. These two objectives are related to each other and improvement in one objective can deteriorate the other. Multi-objective Genetic algorithms (MOGA) give us a set of solutions often called as the Pareto-optimal solution.

One of the disadvantages of GA is that they are computationally expensive i.e time-consuming. For instance, Gaggero [22] designed PBCF energy saving devise using a genetic algorithm and fully viscous RANSE solver. In this study, optimized PBCF design was obtained after evaluation of 900 candidate design and each simulation took around 25 min (including meshing and post-processing) on a medium-end workstation and it took about 15 days of calculations for design optimization. Gaggero [22] used quarter-domain and modeled only one propeller blade. If all four blades of the propeller are considered then, the design optimization procedure would be very time-consuming. In addition, genetic algorithms require thousands of iteration before converging to optimum design as demonstrated in design optimization of hydrofoils by Vernengo et al. [59].

Therefore, when high-fidelity simulations are used for objective function evaluation, then the required CPU time prohibits the use of genetic algorithms for design optimization even with present computational infrastructure. In such cases, surrogate models are built for computationally expensive simulations and optimization is done using these models. These surrogate models [20] are an order of magnitude faster than expensive simulations and at the same time, they provide sufficiently accurate approximations to the real objective function. Lian and Liou [40] used multiobjective genetic algorithms and response surface models to redesign single-stage turbopump, a multi-stage turbopump, and NASA rotor67 compressor blade. Guerrero et al. [25] presented a surrogate-based optimization framework using open source software for the bulbous bow with an objective to minimize hydrodynamic resistance.

6.1 Surrogate-based Optimization

In this section, we discuss each of the components of the design approach which is based on surrogate-based optimization. This includes parametric geometry definition for the propul-

sor, design space exploration, surrogate model construction and running multi-objective optimization to get the Pareto front solution. In this section brief theory for each component is presented.

6.1.1 Parametric Geometry Module

The parametric geometry definition for the propeller and the stator is already discussed in 4.3 and 5.3.2 respectively. In this section, the design variables for the propeller and the stator is presented.

The pitch and the maximum camber of the propeller are the critical parameters that affect the performance of the propulsor and hence only pitch and maximum camber distribution are changed for the design phase. Other parameters like maximum thickness and chord length are not changed. The pitch and the camber distribution is controlled using four control points (as shown in Fig. 4.20) and both horizontal and vertical position of these control points can be used as design variables. The horizontal position of these points is fixed at 0.2 and 1.0 for the hub and tip respectively. Hence, the pitch and camber have six design variables each. The vertical position of the second and third control point is kept the same and the vertical position for the first and last point is calculated based on that position. This helps in avoiding the S-shape distribution for pitch and camber. Finally, the number of design variables reduced to five for both pitch and camber.

For the stator, the position of P_2 (X_2, Y_2) (as shown in Fig. 5.5a) are used as design variables. The position of P_2 will change the turning angle of the stator. The turning angle can be changed from the hub to the tip by changing the coordinates of control points of b-spline curves for X_2 and Y_2. For surrogate-based optimization, the turning angle is kept constant from the hub to the tip. Very few geometry constraint were included such as the projected

length of the stator and avoiding a double curvature shape distribution for pitch and camber.

Design Variable	**Lower bound**	**Upper bound**
P_{1Y}	0.65	1.0
P_{23Y}	0.75	1.05
P_{4Y}	0.7	1.05
P_{2X}	0.3	0.5
P_{3X}	0.6	0.8
C_{1Y}	0.02	0.07
C_{23Y}	0.01	0.05
C_{4Y}	0.005	0.05
C_{2X}	0.3	0.5
C_{3X}	0.6	0.85
X_2	0.1	0.3
Y_2	0.1	0.7

Table 6.1: Design variables for optimization of propulsor

6.1.2 Sobol Sequence

The Sobol sequence is an example of quasi-random low-discrepancy sequence which can be used for exploring the design space [55]. Sobol is similar to a random number sequence in which the aim is the uniform sampling of the design space. But in this case, the clustering effect of random sequences are reduced and can provide an accurate view of the design space. The highest benefit of the exploration phase can be achieved by full factorial design description of the design space. However, for 12 design variables, it would mean excessive computational time for design space exploration. The value of all design variables generated using a Sobol sequence is given in Appendix D.

6.1.3 Response Surface Methodology

RSM is a popular surrogate model used to create approximations of complex and long-running simulations [48]. RSM is used when several input variables influence the performance measure of the product or process. The performance of several design combinations generated using a Sobol sequence as discussed in section 6.1.2 is evaluated using CFD RANSE solver. Once all designs are analyzed, the response surface is constructed for the functional relationship between the design variables and the objective function. In general if a response y depends on the design variables $x_1, x_2, ..., x_k$ then the relationship can be expressed as

$$y = f(x_1, x_2, ..., x_k) + \epsilon \tag{6.1}$$

where ϵ is the term that represents the error not accounted for in f.

Usually, a low-order polynomial in some relatively small region is appropriate for the response surface [48]. In this study, a second-order model is used for RSM. Often the curvature in true response surface is strong enough which cannot be captured by the first-order model. In general, a second-order model is given as

$$y = \beta_0 + \sum_{j=1}^{k} \beta_j x_j + \sum_{j=1}^{k} \beta_{jj} x_j^2 + \sum \sum_{i<j=2}^{k} \beta_{ij} x_i x_j + \epsilon \tag{6.2}$$

where x_i are the design variables and β are the regression coefficients determined using least square method.

The fitted regression model is

$$\hat{y} = Xb \tag{6.3}$$

where $\hat{y}$ is the estimated response vector, X is the matrix of model terms evaluated at design

points and b is the least-square estimator of regression vector β. The difference between the observation y_i and the fitted value $\hat{y}_i$ is called as the residual. The vector b is such that it minimizes the square of each term in the residual vector e defined as

$$e = y - \hat{y} \tag{6.4}$$

There are various statistical measures like coefficient of multiple determination R^2, adjusted R^2 statistic R^2_{adj} that reports the ratio of variability in a data set that the response surface model accounts for. Their calculation involves partitioning the total sum of squares $SS_T = \sum_{i=1}^{n}(y_i - \bar{y})^2$ into a sum of squares due to regression and a sum of squares due to residual. This can be expressed as

$$SS_T = SS_R + SS_E \tag{6.5}$$

The $\bar{y}$ in total sum of squares SS_T is the mean of response given as

$$\bar{y} = \sum_{i=1}^{n} \frac{y_i}{n} \tag{6.6}$$

The R^2 is defined as

$$R^2 = 1 - \frac{SS_E}{SS_T} \tag{6.7}$$

R^2 is a measure of the amount of reduction in the variability of y obtained by using the regressor variables $x_1, x_2, ..., x_k$ in the model. The value of R^2 lies in between 0 and 1. A large value of R^2 does not necessarily mean that the response surface model is good. Addition of variables to the model will always increase R^2, regardless of whether the additional variable is significant or not. Thus it is possible that the response surface with a large value of R^2 gives poor estimates of the mean response.

Because R^2 always increases as we add terms to model, a lot of response surface model uses adjusted R^2 statistic defined as

$$R^2_{adj} = 1 - \frac{SS_E/(n-p)}{SS_T/(n-1)} \tag{6.8}$$

where n is number of observations and p is number of regression coefficients.

6.1.4 Non-dominated Sorting Genetic Algorithm- II

The Non-dominated Sorting Genetic Algorithm- II (NSGA-II) is a multiple objective optimization algorithm and belongs to the category of Evolutionary Algorithms [18]. Evolutionary algorithms are based on the concept of biological evolution and use concepts of reproduction, mutation, recombination, and selection. NSGA-II is one of the most popular multi-objective optimization algorithms with three special characteristics- a fast nondominated sorting procedure, a fast crowded distance estimation procedure, and a simple crowded comparison operator [18]. Various steps in NSGA-II are described below

- Population initialization: Generate a random initial population. Sort the initial population using the concept of non-domination and assign the rank to the level of non-dominance.
- Reproduction: Create offspring of the same size as the initial population using binary tournament selection. recombination and mutation operators.
- Non-dominated Sorting: Combine generation population and offspring population $R_t = P_t \cup Q_t$ to get a new population of size $2N$. Sort the population R_t using the criteria of non-domination.
- Crowding distance sorting: Compute the crowding distance for each member of the

population. The crowding distance is a measure of the density of individuals surrounding a particular solution in the population. Select a new population based on crowded-comparison operator which takes into account the rank and crowded distance of each individual in the population.

6.2 Complete Framework

Fig. 6.1 gives the complete surrogate-based optimization framework. There are many applications like solid modeler, mesher, physics solver, optimizer, results extraction tool and coupling tools that work together for any optimization framework. The optimization framework should be flexible and should be able to start from previously saved state in case of an unexpected failure. Ideally, there should be minimum user intervention in the optimization framework.

In this work, we successfully coupled many applications for solid modeling, meshing, solving the physics and generating Pareto front to efficiently carry out surrogate-based optimization design. We are using CAESES [1], a CAD software which allows the parametric definition of the propulsor. The CAESES software has the capability to automatically generate different designs and export them in a suitable file format that can be processed by the mesher. The Sobol optimizer in CAESES is used for generating initial designs to construct a surrogate model. The range of all design variables created using Sobol sequence is given in Appendix D. All CFD simulations are performed in StarCCM+ (version 12.04.011) [3]. The Java macro feature in StarCCM+ is used to automate the geometry import, computational domain setup, meshing, solving the physics and exporting results.

The RSM toolkit and optimization algorithm in ModelCenter [2] (version 12.0.0.15) is used for constructing a response surface and for optimization using NSGA-II algorithm. In this

work, all software are not coupled directly and user intervention is required for running CFD simulations on supercomputers (ARC clusters), running Java macros and data analysis. The software CAESES, ModelCenter and modeFrontier allows the user to couple all software in one framework and they can communicate with each other automatically. The challenge is to create an interface that will permit the user to use optimization software on their local workstation and run CFD simulations remotely on supercomputers. This task of creating an interface between a local workstation and remote supercomputers is a part of future work. This will allow the user to use robust response surface model like Kriging model [11] and to couple optimization algorithm directly to CAD software and physics solver.

Having developed the complete optimization framework, the next step is to formulate the optimization problem. The multiobjective optimization problem is formulated as below in this work

$$\begin{aligned} &\text{maximize} && \eta_p \\ &\text{minimize} && Q_{Res} \\ &\text{subject to} && \left|\frac{T-D}{T}\right| \leq 5\% \end{aligned} \tag{6.9}$$

where η_P is the propulsor efficiency, Q_{Res} is the residual torque, T is the total thrust, D is the total drag.

The constraint in this study (self-propulsion point constraint) ensures that the thrust/resistance equilibrium point will be achieved when the propeller rotates as speed close to $n = 57$ rps and the hull advances at 2 m/s. The efficiency of the motor is high (as shown in Appendix A) at speed closer to this rotational speed and hence the efficiency of the whole propulsion unit will be high. Another approach would be to allow the propulsor to operate at a different speed of revolution at self-propulsion point. This approach will need calculation of propulsor's performance at two different speeds and interpolate in between those two speeds to calculate self-propulsion point speed. The motor will have different efficiency at

this speed and hence, the efficiency of the whole propulsion unit might get adversely affected.

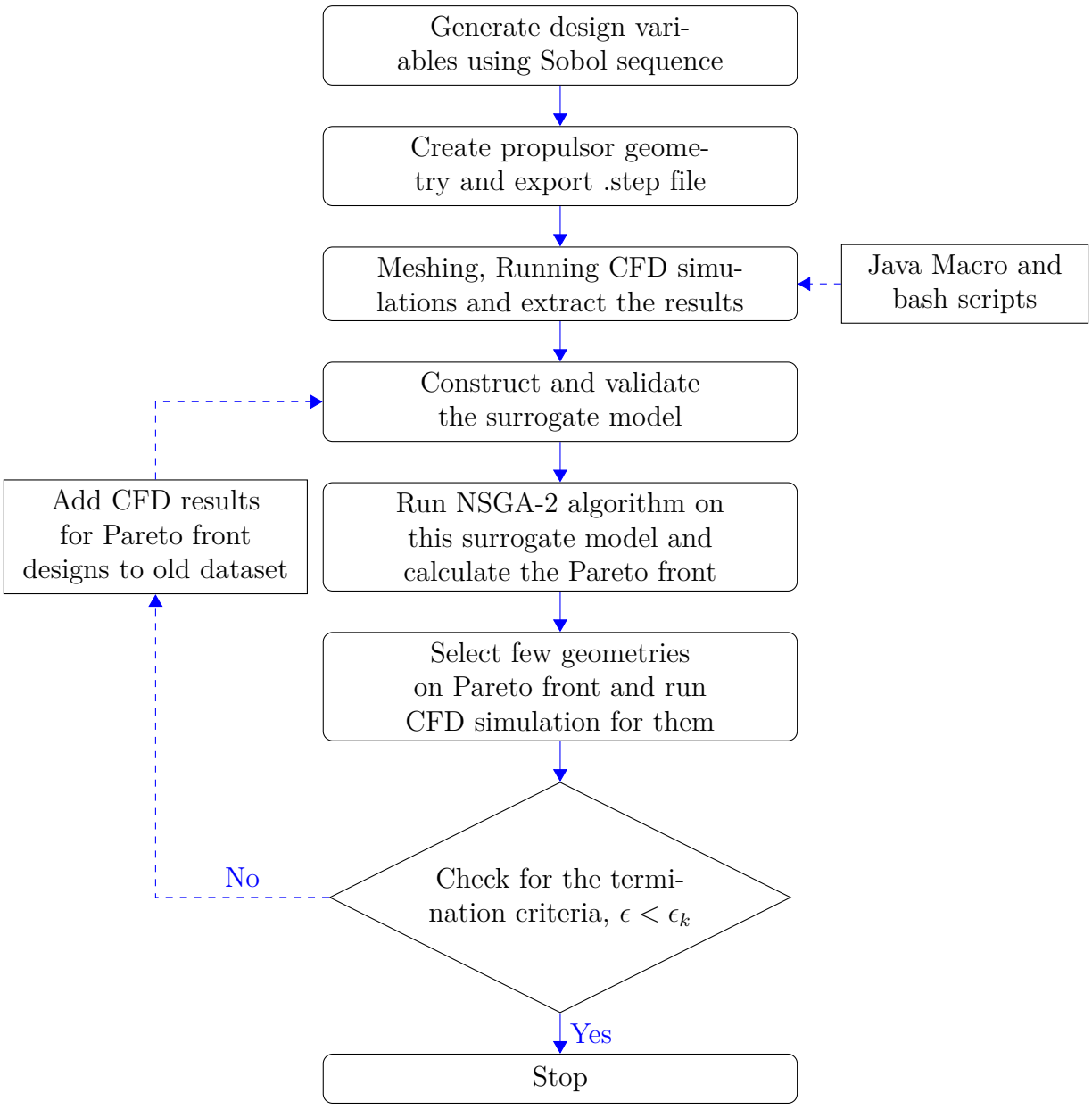

Figure 6.1: Compete optimization framework for the propulsor design

6.3 Optimization Results

In this section, we discuss the results for each of the component of an optimization framework. Fig. 6.2 shows the response surface created for two objective functions- propulsor efficiency, residual torque, and self-propulsion point constraint. The initial data set consists of 120 designs, for which the performance is calculated using CFD RANSE solver as discussed in chapters 3, 4 and 5. The design variables for these designs were generated using a Sobol sequence algorithm. The initial response surface was validated using six designs which were not included in the dataset to construct the response surface. Once we perform optimization on the initial response surface, we get a Pareto front as shown in 6.3a. From this Pareto front, six designs were chosen that are uniformly spaced along a Pareto front. The performance of these designs calculated using CFD simulations are then included in the initial dataset to construct an improved response surface. This is called as infilling. The R^2_{adj} for initial and improved response surfaces is given in table 6.2.

Parameters	**Initial RSM**	**Improved RSM**
Propulsor Efficiency	99.18%	98.96%
Residual Torque (N-m)	99.01%	98.99%
Self-propulsion point constraint	99.74%	99.76%

Table 6.2: The R^2_{adj} for objective functions and constrain for initial and improved response surface model

Fig. 6.3b shows the optimization results for an improved response surface model for the propulsor. The Pareto front is shifted from the original Pareto front shown in Fig. 6.3a obtained for initial response surface. This is because the dataset used for constructing the improved response surface has more data points in the region of interest. The Pareto front in Fig. 6.3b is almost flat and the propulsor efficiency is in the range 56.8% to 57.2% for all Pareto designs. The residual torque for Pareto designs is in the range 0 N-m to 0.14 N-m. This shows that two objective functions (maximize propulsor efficiency and minimize

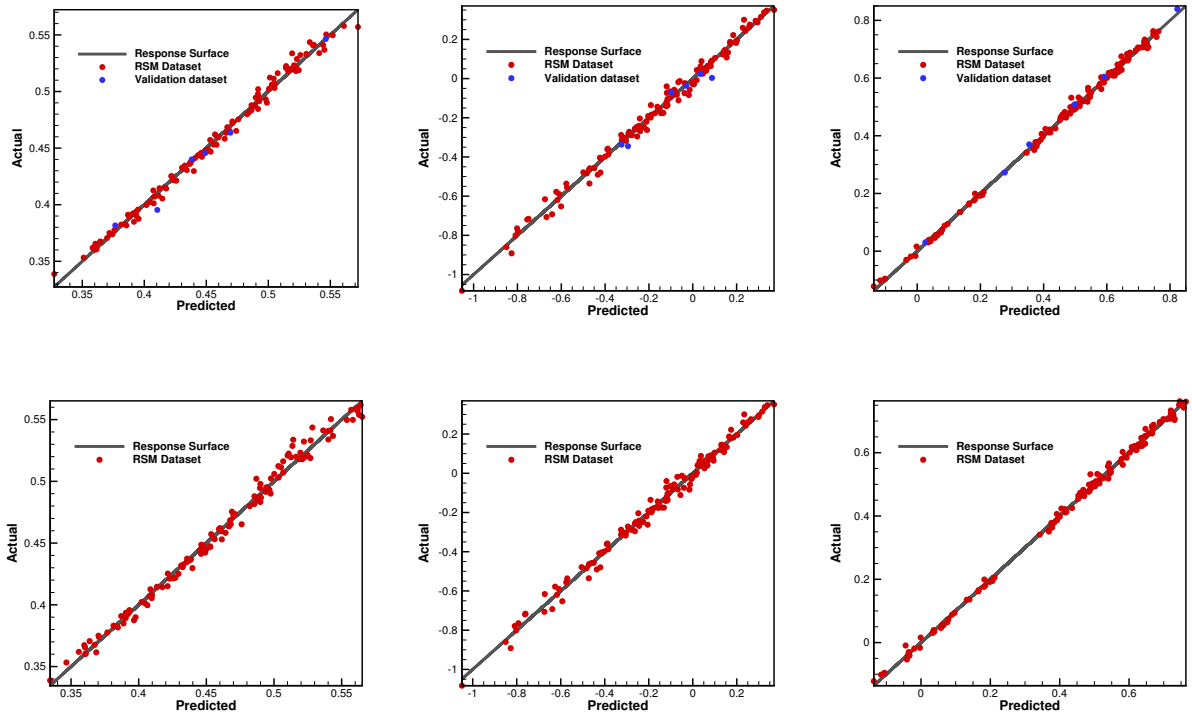

(a) Efficiency (b) Residual torque (N-m) (c) Constraint

Figure 6.2: Top: Correlation plots showing the fidelity of the response surface created using 120 data points for three quantities of interest efficiency (left), residual torque (middle) and thrust constraint (right) Bottom: Correlation plots for response surface created using 126 data points out of which 6 new points are on the Pareto front of initial response surface

residual torque) are not competing. Hence, the optimization algorithm is able to converge to maximum propulsor efficiency regardless of the residual torque.

By analyzing the performance of all geometries that are tested by an optimization algorithm, the correlations and relative importance of design variables on objective functions can be calculated. The variable influence profile plot in ModelCenter [2] is used to gain an insight into key design variables. It allows designers to determine what design parameters are important and to measure its influence on the performance of the geometry. The tornado plot in ModelCenter [2] allows the designer to visualize influence of design variable on a particular response. The value of influence ranges from -1 to 1, with values farther away

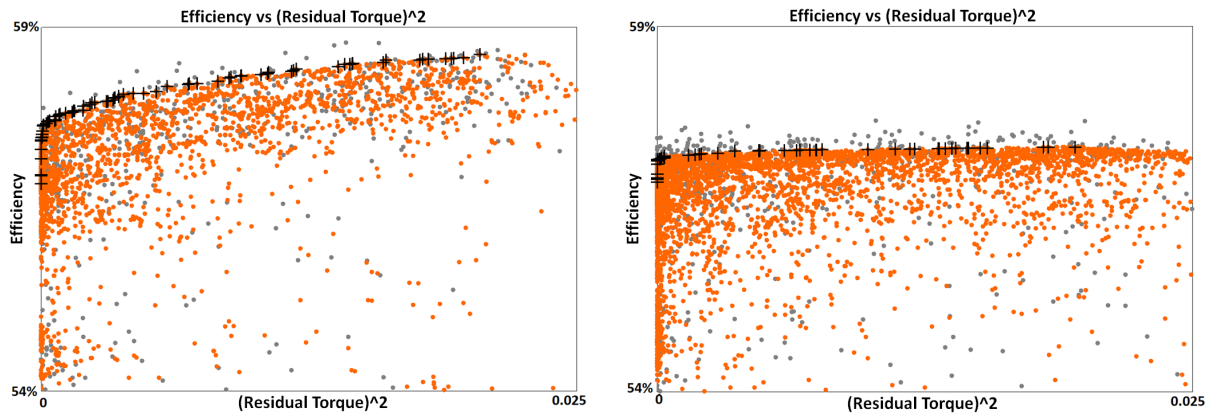

(a) Initial surrogate model

(b) Improved surrogate model using infilling

Figure 6.3: Optimization history with the Pareto front for initial and improved response surface model. Orange color presents the feasible designs, gray color presents infeasible designs and black markers is for Pareto front designs

from 0 indicating a stronger reaction. This type of analysis can help designer for initial screening of design space to understand which design parameters are critical for the product's performance.

Figs. 6.4 and 6.5 summarizes the relationship in the pie chart (importance) and the kind of relation (direct or inverse) between input design variables and objective functions. From Fig. 6.4, we can see that the camber of the propeller is the most important design variable affecting the propulsor efficiency. Fig. 6.5 shows that the design variables X_2 and Y_2 which decides the turning angle for the stator are the critical design parameters for residual torque. This is to be expected because the change in turning angle changes the angle of attack. As the angle of attack changes the lift force acting on the stator also changes. With the change in this lift force, the torque of the stator also changes and the residual torque is mainly dependent on the torque of the stator. Also, the residual torque is not significantly affected by any of the propeller design parameters. This explains the reason for getting flat Pareto front in Fig. 6.3b. The camber of the propeller has an inverse effect on the propulsor

efficiency, while it has a direct effect on the residual torque. The change in camber of the hydrofoil section changes its lift to drag ratio and directly affects the thrust and torque of the propeller. The pitch of the propeller is also a critical design parameter that changes in the efficiency of the propeller. However, in this study the operating point of the propeller is fixed at a speed near to 57 *rps* and all optimum designs have a pitch ratio close to 0.8 (base design). Hence, we do not see pitch design variables as most influencing parameters in Fig. 6.4. There are some design variables like Y_2, P_{1Y} and P_{3X} that has opposite effect on propulsor efficiency and the residual torque.

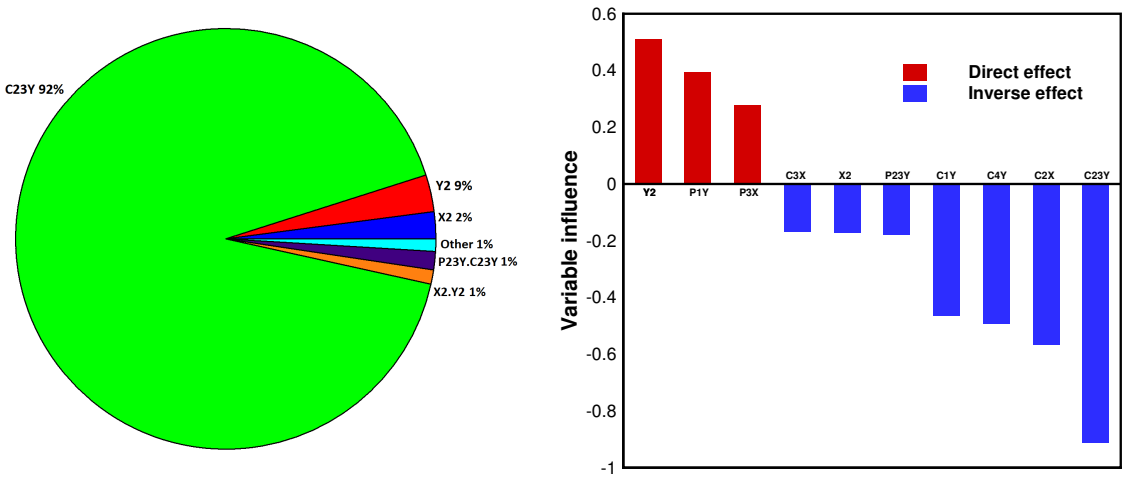

Figure 6.4: Variable influence profiler (left) and tornado plot (right) with respect to propulsor efficiency

6.4 Analysis of Pareto Designs

In order to demonstrate the validity of the surrogate-based optimization framework for designing the propulsor, we select few designs which lies on the Pareto front of the improved

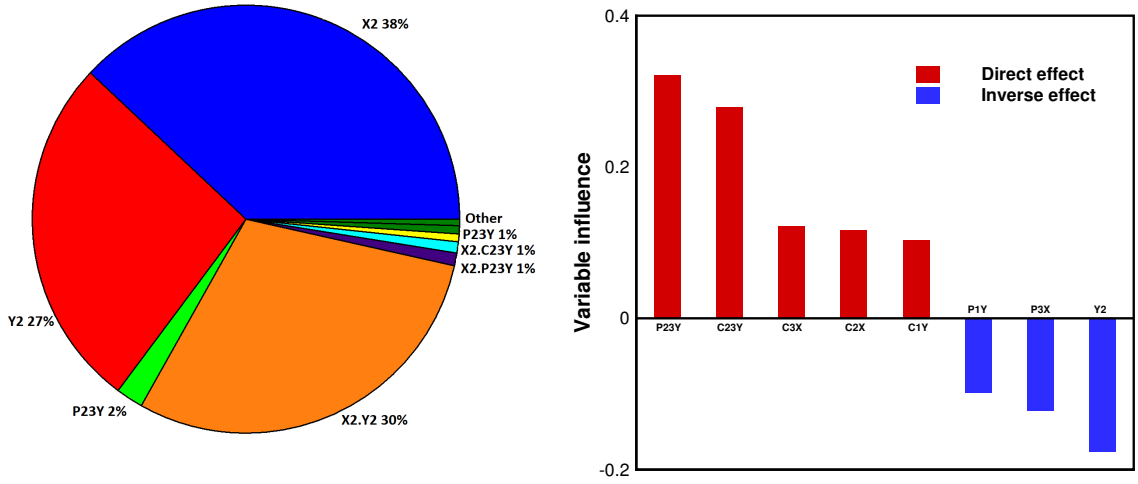

Figure 6.5: Variable influence profiler (left) and tornado plot (right) with respect to residual torque of the propulsor (N-m)

surrogate model. The performance of these designs is calculated using RANSE solver with the transition model. The results for objective functions predicted by CFD RANSE solver and percentage error between the response surface model and CFD RANSE solver are given in Table 6.3

ID	**RANSE Solver**			**Percentage Error**		
	Efficiency (%)	Residual Torque (N-m)	Constraint (%)	Efficiency (%)	Residual Torque (N-m)	Constraint (%)
5469	55.67	0.001	-4.3	2.6	-331	5
5606	56.23	0.082	-4.9	1.9	18	-7
5796	55.68	-0.001	-4.5	2.6	181	-1
5821	56.35	0.112	-5.0	1.7	17	-14
5965	56.05	0.048	-4.6	2.1	10	-6

Table 6.3: Results for objective functions predicted by RANSE solver and percentage error (between response surface and RANSE solver) of five designs selected from Pareto front of improved surrogate model

From the results shown in Table 6.3, we can see that there is a very slight improvement in efficiency in comparison to base propulsor geometry (Section 5.3.2). The residual torque,

on the other hand, is considerably reduced and is almost near zero value. The propeller is operating at very high loading condition and has a large suction upstream to the propeller. The velocity inflow to the propeller is almost uniform from hub to the tip. This explains why we do not see significant improvement in propulsor efficiency by considering non uniform pitch distribution along the radius. The base propeller geometry which has uniform pitch distribution is already a good design for operating at high loading condition and hence Pareto designs do not demonstrate improvement in propulsor efficiency. Even though the optimum pitch distribution found in this case is pretty trivial, it is still important to find the absolute value of the uniform pitch to ensure the prescribed thrust. Also, it appears that the overall design problem can be decomposed in two almost independent problems. The efficiency and the thrust objective functions depend predominantly on design variables related to the propeller geometry; the minimum residual torque problem depends on the stator geometry design variables. This explains the almost horizontal shape of the Pareto front in Fig. 6.3b The percentage error for propulsor efficiency is less than 3% for all Pareto designs.

The base stator design was not a good design and was not counteracting the propeller torque completely. The Pareto designs have residual torque almost close to zero value. The percentage error between the response surface model and RANSE solver for residual torque is very high in some cases. However, the residual torque is almost zero for these designs and absolute difference between response surface model and RANSE solver prediction is very small. The self-propulsion point constraint predicted using response surface model is consistent with RANSE solver results with a maximum error of 14% for design 5821. From the results presented in this section, we can conclude that the surrogate-based optimization can be an effective design tool especially if the high-fidelity solver is to be used for performance calculation.

Chapter 7

Conclusion and Future Work

In this thesis, we present a design framework based on the use of high-fidelity RANSE solver and surrogate-based optimization for the propulsor design which operates at very high loading condition. We analyze the total thrust requirement and propeller-hull interaction using empirical relations and experimental data at the conceptual design stage. The conceptual design of the propulsor leads to the selection of propeller $K_a - 4 - 70$ with $P/D = 0.8$ inside an accelerating duct 19A with an objective to maximize propulsor efficiency at a speed close to motor's operating point and to minimize the propeller torque.

We demonstrate the capability of RANSE solver with the $\gamma - Re_\theta$ transition model to capture low Reynolds number physics by comparison with the experimental work published in the literature for model scale propeller. The application of the transition model for ducted propeller shows a significant difference in terms of local flow pattern and global hydrodynamic forces as compared to using a fully turbulent model. The results obtained show that the transition model is able to predict complex flow physics such as leading-edge separation, tip leakage vortex, and the separation bubble on the outer surface of the duct that leads to correct calculation of global hydrodynamic forces and moments acting on the propeller at low Reynolds number. We present a simple design method for postswirl stator based on axial compressor design principle. The analysis of different stator shapes shows that the NACA 0015 thickness gives better performance in terms of residual torque of the propulsor. We show that the steady-state MRF approach is sufficient to model the propulsor

than computationally expensive unsteady sliding mesh approach.

We developed a surrogate-based optimization framework which is built on parametric geometry definition for the propulsor, RANSE solver, construction of response surface and multi-objective optimization algorithm. From the results presented in Chapter 6, we can conclude that the surrogate-based optimization can be used as a designing tool for marine propulsor when the use of high-fidelity solver is warranted. However, the user should pay extra attention to the construction of the surrogate model, since the final results depend on the quality of the surrogate model. The propulsor designed using this method has efficiency of around 56 % with almost zero residual torque.

The propulsor designed in Chapter 6 should be tested in the field for efficiency and the residual torque. Fig. 7.1 shows the designed propulsor mounted on Virginia Tech Dragon AUV. Future work includes monitoring the power delivered to the propulsor when the mission is given. The current drawn by the motor can be used for calculating the propulsor torque. The roll angle and vehicles CG-CB separation can be used for calculating the residual torque.

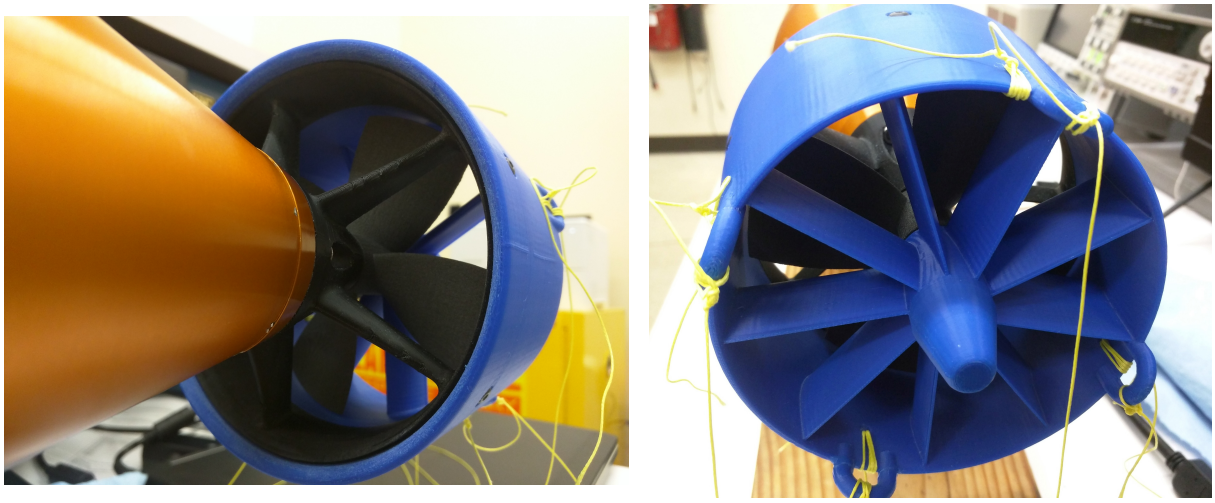

Figure 7.1: Designed propulsor mounted on Virginia Tech Dragon AUV

Bibliography

[1] CAESES friendship systems. https://www.caeses.com/. Accessed: 2017-2018.

[2] ModelCenter®12.0.0.15 Documentation. Accessed: 2018.

[3] StarCCM+ 12.04.011 Documentation. https://thesteveportal.plm.automation.siemens.com/. Accessed: 2017-2018.

[4] Barrett Baldwin and Harvard Lomax. Thin-layer approximation and algebraic model for separated turbulentflows. In *16th aerospace sciences meeting*, page 257, 1978.

[5] J Baltazar, JAC Falcão de Campos, and J Bosschers. Open-water thrust and torque predictions of a ducted propeller system with a panel method. *International Journal of Rotating Machinery*, 2012, 2012.

[6] J Baltazar, D Rijpkema, J Falcão de Campos, and J Bosschers. A comparison of panel method and rans calculations for a ducted propeller system in open-water. In *Third International Symposium on Marine Propulsors (SMP2013), Launceston, Tasmania, Australia*, 2013.

[7] JM Baltazar, D Rijpkema, and J Falcão de Campos. On the use of the γ-reθ transition model for the prediction of the propeller performance at model-scale. In *Proceedings of the Fifth International Symposium on Marine Propulsors SMP*, volume 17, 2017.

[8] D Bertetta, S Brizzolara, S Gaggero, M Viviani, and L Savio. Cpp propeller cavitation and noise optimization at different pitches with panel code and validation by cavitation tunnel measurements. *Ocean engineering*, 53:177–195, 2012.

[9] Anirban Bhattacharyya, Vladimir Krasilnikov, and Sverre Steen. Scale effects on open water characteristics of a controllable pitch propeller working within different duct designs. *Ocean Engineering*, 112:226–242, 2016.

[10] Scott Donald Black. *Integrated lifting-surface/Navier-Stokes design and analysis methods for marine propulsors*. PhD thesis, Massachusetts Institute of Technology, 1997.

[11] Andrew J Booker. Examples of surrogate modeling of computer simulations. In *ISSMO/NASA/AIAA First Internet Conference on Approximations and Fast Reanalysis in Engineering Optimization*, 1998.

[12] S Brizzolara, D Villa, and S Gaggero. A systematic comparison between rans and panel methods for propeller analysis. In *Proc. Of 8th International Conference on Hydrodynamics, Nantes, France*, 2008.

[13] Stefano Brizzolara. Parametric optimization of swat-hull forms by a viscous-inviscid free surface method driven by a differential evolution algorithm. In *Proceedings 25th Symposium on Naval Hydrodynamics, St. John's, Newfoundland and Labrador*, volume 5, pages 47–64, 2004.

[14] Stefano Brizzolara, Stefano Gaggero, and Alessandro Grasso. Parametric optimization of open and ducted propellers. In *In Proceedings of the SNAME Propellers and Shafting Symposium*, 2009.

[15] Terry Brockett. Minimum pressure envelopes for modified naca-66 sections with naca a= 0.8 camber and buships type 1 and type 2 sections. Technical report, DAVID TAYLOR MODEL BASIN WASHINGTON DC HYDROMECHANICS LAB, 1966.

[16] John Carlton. *Marine propellers and propulsion*. Butterworth-Heinemann, 2012.

[17] Benjamin YH Chen and Carol L Tseng. A postswirl propulsor for a small vehicle. Technical report, NAVAL SURFACE WARFARE CENTER CARDEROCK DIV BETHESDA MD, 1995.

[18] Kalyanmoy Deb, Amrit Pratap, Sameer Agarwal, and TAMT Meyarivan. A fast and elitist multiobjective genetic algorithm: Nsga-ii. *IEEE transactions on evolutionary computation*, 6(2):182–197, 2002.

[19] Mark Drela and Michael B Giles. Viscous-inviscid analysis of transonic and low reynolds number airfoils. *AIAA journal*, 25(10):1347–1355, 1987.

[20] Michael S Eldred, Anthony A Giunta, Bart G van Bloemen Waanders, Steven F Wojtkiewicz, William E Hart, and Mario P Alleva. Dakota, a multilevel parallel object-oriented framework for design optimization, parameter estimation, uncertainty quantification, and sensitivity analysis. Technical report, Citeseer, 2006.

[21] Brenden Epps, Julie Chalfant, Richard Kimball, Alexandra Techet, Kevin Flood, and Chrysssostomos Chryssostomidis. Openprop: An open-source parametric design and analysis tool for propellers. In *Proceedings of the 2009 grand challenges in modeling & simulation conference*, pages 104–111. Society for Modeling & Simulation International, 2009.

[22] Stefano Gaggero. Design of pbcf energy saving devices using optimization strategies: A step towards a complete viscous design approach. *OCEAN ENGINEERING*, 159: 517–538, 2018.

[23] Stefano Gaggero and Stefano Brizzolara. Exact modeling of trailing vorticity in panel method for marine propeller. *Proceedings of ICMRT*, 2007.

[24] Stefano Gaggero, Juan Gonzalez-Adalid, and Mariano Perez Sobrino. Design of contracted and tip loaded propellers by using boundary element methods and optimization algorithms. *Applied Ocean Research*, 55:102–129, 2016.

[25] Joel Guerrero, Alberto Cominetti, Jan Pralits, and Diego Villa. Surrogate-based optimization using an open-source framework: The bulbous bow shape optimization case. *Mathematical and Computational Applications*, 23(4):60, 2018.

[26] M Guner and EJ Glover. Propeller/stator propulsors for autonomous underwater vehicles. In *Autonomous Underwater Vehicle Technology, 1994. AUV'94., Proceedings of the 1994 Symposium on*, pages 331–336. IEEE, 1994.

[27] RE Henderson, JF McMahon, and GF Wislicenus. A method for the design of pumpjets. Technical report, PENNSYLVANIA STATE UNIV STATE COLLEGE ORDNANCE RESEARCH LAB, 1964.

[28] SF Hoerner. Fluid dynamics drag, published by the author. *Midland Park, NJ*, 1965.

[29] Michael Joseph Hughes. *Analysis of multi-component ducted propulsors in unsteady flow*. PhD thesis, Massachusetts Institute of Technology, 1993.

[30] Stephen A Huyer. Postswirl maneuvering propulsor. *Journal of Fluids Engineering*, 137 (4):041104, 2015.

[31] Stephen A Huyer, Amanda Dropkin, David N Beal, John AN Farnsworth, and Michael Amitay. Preswirl maneuvering propulsor. *IEEE Journal of Oceanic Engineering*, 37(1): 122–138, 2012.

[32] Harry A Jackson. Fundamentals of submarine concept design. 1992.

[33] WP Jones and Brian Edward Launder. The prediction of laminarization with a two-equation model of turbulence. *International journal of heat and mass transfer*, 15(2): 301–314, 1972.

[34] S Kinnas and N Fine. A nonlinear boundary element method for the analysis of unsteady propeller sheet cavitation. 1994.

[35] G Kuiper. Scale effects on propeller cavitation inception. *12th Sym. posium on Naval Hydrodynamics*, pages 401–429, 1978.

[36] Gerrit Kuiper. *Cavitation inception on ship propeller models*. PhD thesis, TU Delft, Delft University of Technology, 1981.

[37] Robin Blair Langtry. A correlation-based transition model using local variables for unstructured parallelized cfd codes. 2006.

[38] Robin Blair Langtry, FR Menter, SR Likki, YB Suzen, PG Huang, and S Völker. A correlation-based transition model using local variables—part ii: test cases and industrial applications. *Journal of Turbomachinery*, 128(3):423–434, 2006.

[39] Edward V Lewis. Principles of naval architecture second revision. *Jersey: SNAME*, 1988.

[40] Yongsheng Lian and Meng-Sing Liou. Multiobjective optimization using coupled response surface model and evolutionary algorithm. *AIAA journal*, 43(6):1316–1325, 2005.

[41] FS Lien, WL Chen, and MA Leschziner. Low-reynolds-number eddy-viscosity modelling based on non-linear stress-strain/vorticity relations. In *Engineering Turbulence Modelling and Experiments, Volume 3*, pages 91–100. Elsevier, 1996.

[42] Fue-Sang Lien and MA Leschziner. Assessment of turbulence-transport models including non-linear rng eddy-viscosity formulation and second-moment closure for flow over a backward-facing step. *Computers & Fluids*, 23(8):983–1004, 1994.

[43] Mark W McBride. The design and analysis of turbomachinery in an incompressible, steady flow using the streamline curvature method. Technical report, PENNSYLVANIA STATE UNIV UNIVERSITY PARK APPLIED RESEARCH LAB, 1979.

[44] Florian R Menter. Two-equation eddy-viscosity turbulence models for engineering applications. *AIAA journal*, 32(8):1598–1605, 1994.

[45] Florian R Menter, Robin Blair Langtry, SR Likki, YB Suzen, PG Huang, and S Völker. A correlation-based transition model using local variables—part i: model formulation. *Journal of turbomachinery*, 128(3):413–422, 2006.

[46] Keh-Sik Min, Bong-Jun Chang, and Heung-Won Seo. Study on the contra-rotating propeller system design and full-scale performance prediction methodin rapid hull form generation. *International Journal of Naval Architecture and Ocean Engineering*, 1(1): 29–38, 2009.

[47] Anthony F Molland, Stephen R Turnock, and Dominic A Hudson. *Ship resistance and propulsion*. Cambridge university press, 2017.

[48] Raymond H Myers, Douglas C Montgomery, et al. *Response surface methodology: process and product optimization using designed experiments*, volume 4. Wiley New York, 1995.

[49] DF Myring. A theoretical study of body drag in subcritical axisymmetric flow. *The Aeronautical Quarterly*, 27(3):186–194, 1976.

[50] MWC Oosterveld. Ducted propeller systems suitable for tugs and pushboats. *International Shipbuilding Progress*, 19(219):351–371, 1972.

[51] MWC Oosterveld. Ducted propeller characteristics. In *RINA symposium on ducted propellers*, 1973.

[52] S. V. Patankar and D. B. Spalding. A calculation procedure for heat, mass and momentum transfer in three-dimensional parabolic flows. *International Journal of Heat and Mass Transfer*, 15(10):1787–1806, 1972.

[53] Robert O Reid and Basil W Wilson. Boundary flow along a circular cylinder. Technical report, TEXAS A AND M UNIV COLLEGE STATION, 1962.

[54] Wolfgang Rodi. Experience with two-layer models combining the k-epsilon model with a one-equation model near the wall. In *29th Aerospace sciences meeting*, page 216, 1991.

[55] Il'ya Meerovich Sobol'. On the distribution of points in a cube and the approximate evaluation of integrals. *Zhurnal Vychislitel'noi Matematiki i Matematicheskoi Fiziki*, 7 (4):784–802, 1967.

[56] M Jordan Stanway and Thaddeus Stefanov-Wagner. Small-diameter ducted contrarotating propulsors for marine robots. In *OCEANS 2006*, pages 1–6. IEEE, 2006.

[57] Keerati Suluksna, Pramote Dechaumphai, and Ekachai Juntasaro. Correlations for modeling transitional boundary layers under influences of freestream turbulence and pressure gradient. *International Journal of Heat and Fluid Flow*, 30(1):66–75, 2009.

[58] Ch. Suryanarayana, B. Satyanarayana, K. Ramji, and A. Saiju. Experimental evaluation of pumpjet propulsor for an axisymmetric body in wind tunnel. *International Journal of Naval Architecture and Ocean Engineering*, 2(1):24 – 33, 2010. ISSN 2092-6782. doi:

https://doi.org/10.2478/IJNAOE-2013-0016. URL http://www.sciencedirect.com/science/article/pii/S209267821630228X.

[59] Giuliano Vernengo, Luca Bonfiglio, Stefano Gaggero, and Stefano Brizzolara. Physics-based design by optimization of unconventional supercavitating hydrofoils. *Journal of Ship Research*, 60(4):187–202, 2016.

[60] Florian Vesting and Rickard E Bensow. On surrogate methods in propeller optimisation. *Ocean Engineering*, 88:214–227, 2014.

[61] Florian Vesting, Rickard Gustafsson, and Rickard E Bensow. Development and application of optimisation algorithms for propeller design. *Ship Technology Research*, 63(1): 50–69, 2016.

[62] Xiao Wang and Keith Walters. Computational analysis of marine-propeller performance using transition-sensitive turbulence modeling. *Journal of Fluids Engineering*, 134(7): 071107, 2012.

[63] Christopher L Warren. Prediction of propulsor-induced maneuvering forces using a coupled viscous/potential-flow method for integrated propulsors. Technical report, MASSACHUSETTS INST OF TECH CAMBRIDGE DEPT OF OCEAN ENGINEERING, 1999.

[64] David C Wilcox. Reassessment of the scale-determining equation for advanced turbulence models. *AIAA journal*, 26(11):1299–1310, 1988.

[65] David C Wilcox. Formulation of the kw turbulence model revisited. *AIAA journal*, 46 (11):2823–2838, 2008.

[66] Liangyu Xu, Emilio Baglietto, and Stefano Brizzolara. Extending the applicability of rans turbulence closures to the simulation of transitional flow around hydrofoils at

low reynolds number. *Ocean Engineering*, 164:1 – 12, 2018. ISSN 0029-8018. doi: https://doi.org/10.1016/j.oceaneng.2018.06.031. URL http://www.sciencedirect.com/science/article/pii/S0029801818310552.

[67] Gert-Jan Zondervan, Jan Holtrop, Jaap Windt, and T Terwisga. On the design and analysis of pre-swirl stators for single and twin screw ships. In *Second International Symposium on Marine Propellers*, 2011.

Appendices

Appendix A

Motor Calculation

There are three fundamental relations in the motor model

- Resistance model: The resistance of the motor R is assumed to be constant
- Voltage model: The internal back-EMF voltage v_m is directly proportional to motor's rotation rate ω_m via the motor constant K_V. Here the units for K_V are in $rpm/volt$.

$$v_m = \frac{\omega_m}{K_V} \tag{A.1}$$

- Torque model: The shaft torque Q_m is proportional to the difference between the motor current i and no-load current i_0 via the torque constant K_Q. Here the torque constant is in $N - m/A$

$$Q_m = K_Q(i - i_0) \tag{A.2}$$

The motor terminal voltage is the sum of back-EMF voltage v_m and the resistance voltage drop as given below

$$V = v_m + iR \tag{A.3}$$

The model equations above are manipulated to get the variation of current, speed and efficiency as a function of shaft torque.

$$i = \frac{Q_m}{K_Q} + i_0 \tag{A.4}$$

$$\omega_m = (V - iR)K_V \tag{A.5}$$

$$\eta_m = \frac{2\pi\omega_m Q_m}{iV} \tag{A.6}$$

Fig. A.1 shows the motor characteristics curves for Turningy Rotomax 1.2 Brushless Outruner motor. The highlighted area gives the speed, shaft torque, and the current drawn by the motor at which the motor has high efficiency. This motor was selected from a database of 57 commercial off the shelf motors. This motor has $K_V = 280\ rpm/volt$, $K_Q = 0.0341\ N-m/A$, $i_0 = 1.55\ A$, $R = 0.027\ \Omega$

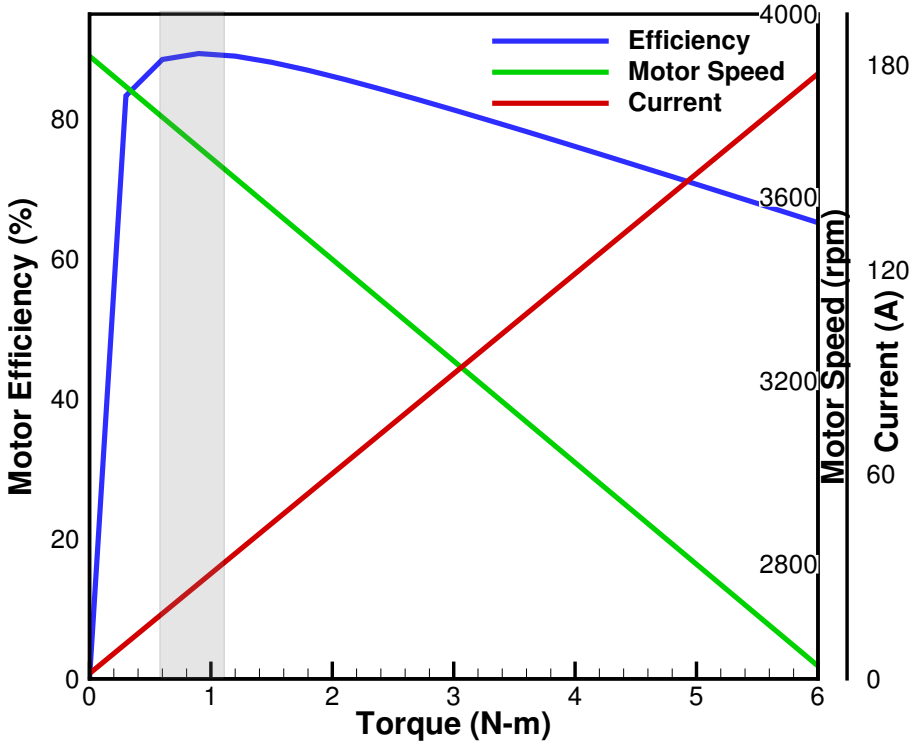

Figure A.1: Motor characteristics curves for Turnigy RotoMax 1.20 brushless outrunner motor

Appendix B

Propeller Geometry

The base geometry of the propeller K_a series screw propeller is given in Table B.1. The ordinates of back and face of the hydrofoil at different radial location is given in Table B.2. This gives the 2D section hydrofoil. The 2D hydrofoil section is then converted to 3D hydrofoil shape. The 3D hydrofoil section are lofted from hub to the tip in a CAD modeling software to get the propeller geometry. The 3D hydrofoil section coordinates are calculated as below from 2D hydrofoil coordinates

$$x_p = -[i_G + r\theta_s tan(\theta_{nt})] + (0.5c - x_c)sin(\theta_{nt}) + y_{u,L}cos(\theta_{nt}) \tag{B.1}$$

$$y_p = rsin\Big[\theta_s - \frac{180[(0.5c - x_c)cos(\theta_{nt}) - y_{u,L}sin(\theta_{nt})]}{\pi r}\Big] \tag{B.2}$$

$$z_p = rcos\Big[\theta_s - \frac{180[(0.5c - x_c)cos(\theta_{nt}) - y_{u,L}sin(\theta_{nt})]}{\pi r}\Big] \tag{B.3}$$

where i_G is the propeller rake, θ_S is the skew angle, θ_{nt} is the pitch angle, c is the chord lenght, r is the radius of section radius, x_c is the abscissa of the hydrofoil section, and $y_{u,L}$ is the ordinates of back and face of the 2D hydrofoil section.

Dimensions of the K_a screw series propeller											
r/R		0.2	0.3	0.4	0.5	0.6	0.7	0.8	0.9	1.0	
Length of the blade sections in percentages of the maximum length of the blade section at $0.6R$	from center line to trailing edge	30.21	36.17	41.45	45.99	49.87	52.93	55.04	56.33	56.44	Length of the blade section at $0.6R = 1.969\frac{D}{Z}\frac{A_E}{A_0}$
	from center line to leading edge	36.94	40.42	43.74	47.02	50.13	52.94	55.04	56.33	56.44	
	from center line to leading edge	67.15	76.59	85.19	93.01	100.00	105.86	110.08	112.66	112.88	
Maximum blade thickness in percentage of the diameter		4.00	3.52	3.00	2.45	1.90	1.38	0.92	0.61	0.50	Maximum thickness at center of shaft $= 0.049D$
Distance of maximum thickness from leading edge in percentages of the length of the sections		34.98	39.76	46.02	49.13	49.98	-	-	-	-	

Table B.1: Details of the K_a- series screw propeller (taken from Oosterveld [51])

Distance of the ordinates from maximum the maximum thickness												
From maximum thickness to trailing edge						From maximum thickness to leading edge						
r/R	100%	80%	60%	40%	20%	20%	40%	60%	80%	90%	95%	100%
ordinates for the face												
0.2	-	38.23	63.65	82.40	95.00	97.92	90.83	77.19	55.00	38.75	27.40	
0.3	-	39.05	66.63	84.14	95.86	97.63	90.06	75.62	53.02	37.87	27.57	-
0.4	-	40.56	66.94	85.69	96.25	97.22	88.89	73.61	50.00	34.72	25.83	-
0.5	-	41.77	68.59	86.42	96.60	96.77	87.10	70.46	45.84	30.22	22.24	-
0.6	-	43.58	68.26	85.89	96.47	96.47	85.89	68.26	43.58	28.59	20.44	-
0.7	-	45.31	69.24	86.33	96.58	96.58	86.33	69.24	45.31	30.79	22.88	-
0.8	-	48.16	70.84	87.04	96.76	96.76	87.04	70.84	48.16	34.39	26.90	-
0.9	-	51.75	72.94	88.09	97.17	97.17	88.09	72.94	51.75	38.87	31.87	-
1.0	-	52.00	73.00	88.00	97.00	97.00	88.00	73.00	52.00	39.25	32.31	-
Ordinates for the face												
0.2	20.21	7.29	1.77	0.1	-	0.21	1.46	4.37	10.52	16.04	20.62	33.33
0.3	13.85	4.62	1.07	-	-	0.12	0.83	2.72	6.15	8.28	10.30	21.18
0.4	9.17	2.36	0.56	-	-	-	0.42	1.39	2.92	3.89	4.44	13.47
0.5	6.62	0.68	0.17	-	-	-	0.17	0.51	1.02	1.36	1.53	7.81

Table B.2: Ordinates of the K_a - series screw propeller (taken from Oosterveld [51])

109

Appendix C

NACA Hydrofoil

Table C.1: NACA a=0.8 mean line

x_x (% c)	y_x (% c)	dy_c/dx_c
0	0	
0.5	0.287	0.48535
0.75	0.404	0.44925
1.25	0.616	0.40359
2.5	1.077	0.34101
5	1.841	0.27718
7.5	2.483	0.23868
10	3.043	0.21050
15	3.985	0.16892
20	4.748	0.13734
25	5.367	0.11101
30	5.863	0.08775
35	6.248	0.06634
40	6.528	0.04601
45	6.709	0.02613
50	6.790	0.00620
55	6.770	-0.01433
60	6.644	-0.03611
65	6.405	-0.06010
70	6.037	-0.08790
75	5.514	-0.12311
80	4.771	-0.18412
85	3.683	-0.23921
90	2.435	-0.25583
95	1163	-0.24904
100	0	-0.20385

Table C.2: NACA 66 (mod) thickness

x/c	y/t_{max}
0	0
0.005	0.0665
0.0075	0.0812
0.0125	0.1044
0.0250	0.1466
0.0500	0.2066
0.0750	0.2525
0.1000	0.2907
0.1500	0.3521
0.2000	0.4000
0.2500	0.4363
0.3000	0.4637
0.3500	0.4832
0.4000	0.4952
0.4500	0.5000
0.5000	0.4962
0.5500	0.4846
0.6000	0.4653
0.6500	0.4383
0.7000	0.4035
0.7500	0.3612
0.8000	0.3110
0.8500	0.2532
0.9000	0.1877
0.9500	0.1143
1.0000	0.0333

Appendix D

Design Space Exploration

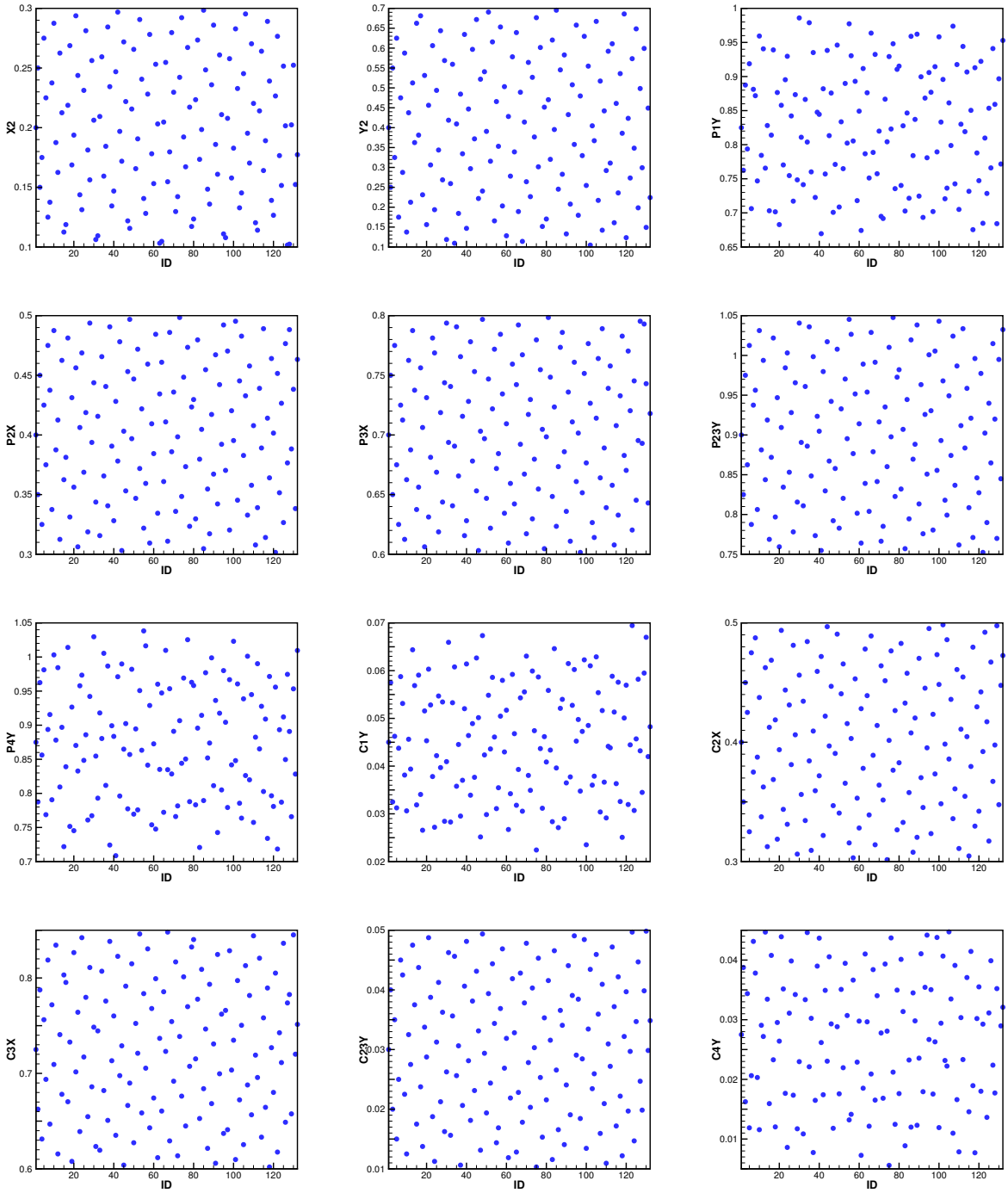

Figure D.1: Design variables generated using Sobol sequence for creating data (120 data points) for initial response surface